

---

**MODELING AND DEVELOPMENT OF  
CONTROLLED TOPOGRAPHY  
REACTORS AND THEIR APPLICATION IN  
THE FIELD OF INDUSTRIAL  
BIOTECHNOLOGY**

---

**Valentina Preziosi**

Dottorato in Scienze Biotecnologiche – XXIV ciclo  
Indirizzo Biotecnologie Industriali  
Università di Napoli Federico II







---

**MODELING AND DEVELOPMENT OF  
CONTROLLED TOPOGRAPHY  
REACTORS AND THEIR APPLICATION IN  
THE FIELD OF INDUSTRIAL  
BIOTECHNOLOGY**

---

**Valentina Preziosi**

Dottoranda: Valentina Preziosi  
Relatore: Prof. Stefano Guido  
Co-relatore: Ing. Alberto Simoncelli  
Coordinatore: Prof. Giovanni Sannia







# Summary

<b>SUMMARY</b>	<b>7</b>
<b>ABSTRACT</b>	<b>8</b>
<b>RIASSUNTO</b>	<b>9</b>
<b>CHAPTER 1 EMULSIFICATION</b>	<b>15</b>
1.1 INTRODUCTION	15
1.2 STABILITY	17
1.3 EMULSIFICATION DEVICES	18
1.4 PRINCIPLE OF RHEOLOGY	19
1.4 FLUID DYNAMICS OF DEFORMABLE DROPS	21
1.9 AIM OF THE THESIS	24
<b>CHAPTER 2 FLOW OF EMULSIONS IN MICROCAPILLARIES</b>	<b>25</b>
2.1 MATERIALS AND METHODS	25
2.1.1 <i>Materials</i>	25
2.1.2 <i>Flow cell</i>	25
2.1.3 <i>Experimental apparatus</i>	26
2.2 RESULTS	27
2.2.1 <i>Characterization</i>	27
2.2.2 <i>Image analysis</i>	28
2.2.3 <i>Deformability of dispersed phase</i>	30
2.3 APPLICATION IN BIOTECHNOLOGY	31
<b>CHAPTER 3 PHASE INVERSION EMULSIFICATION</b>	<b>32</b>
3.1 MATERIALS AND METHODS	34
3.2 RESULTS	34
3.2.1 <i>Particle size distribution and stability</i>	35
3.2.2 <i>Electrical conductivity measurements</i>	37
3.2.3 <i>Rheological measurements</i>	38
3.2.4 <i>Morphology by CSLM</i>	39
3.2.5 <i>Interfacial tension measurements</i>	40
<b>CHAPTER 4 MIXING OF LIQUID-LIQUID NON NEWTONIAN FLUIDS</b>	<b>41</b>
4.1 MATERIALS AND METHODS	41
4.1.1 <i>Materials</i>	41
4.1.2 <i>Static mixers and experimental apparatus</i>	43
4.2 RESULTS	44
4.2.1 <i>Rheological measurements</i>	44
4.2.2 <i>Characterization</i>	45
4.2.3 <i>Interfacial tension measurements</i>	46
4.2.4 <i>Image analysis</i>	47
<b>CONCLUSIONS</b>	<b>50</b>
<b>BIBLIOGRAPHY</b>	<b>51</b>
<b>APPENDIX</b>	<b>54</b>

## Abstract

The mixing of liquids is a common operation in process industries such as chemical and pharmaceutical industries. However the problem of mixing different liquids has not been rigorously characterized yet. Therefore one of the aims of this PhD thesis was focused on mixing in microsystems, like microcapillaries and micromixers.

Microfluidic systems, fabricated by utilizing silicone, biomaterials, or stainless steel, have gathered enormous attention in the recent years. Compared to industrial laboratory equipment, these microsystems offer reduced reagent consumption, more safety and lower time for analysis. Their reduced size makes them suitable for mobile field laboratories, while their reduced cost allows them to be disposable after sensitive applications. Microsystems fit perfectly with the Process Intensification (PI) strategy, an engineering expression that refers to making changes that render a manufacturing or processing design substantially improved in terms of energy efficiency, cost-effectiveness or enhancement of other qualities. The design of microfluidic systems often requires unusual geometries and the interplay of multiple physical effects such as pressure gradients and capillarity, which lead to interesting variants of well-studied fluid dynamical problems and some new fluid responses. The rapidly increasing interest in the application and control of emulsions in microfluidics devices for industrial biotechnological purposes motivates this research. In particular emulsification process to form stable samples over time by using different techniques was investigated. Fluid dynamic behavior of a stable oil-in-water emulsion was characterized in microcapillaries and contrast-enhanced optical microscopy was used for direct observation and automated image analysis algorithms have been developed to characterize the velocity and the deformability of drops flowing in capillaries of micrometric dimensions. Fundamental understanding of emulsification process is very important from a biotechnological point of view because it is present in many biological processes. For example the motion of droplets under confined flow has attracted some interest due to the similarities with the shape taken by red blood cells in microcapillaries.

Furthermore emulsification process in micro static mixers of different diameter and length was analyzed and theoretical models to predict emulsion particle size distribution were performed. Finally scale-up of these microreactors was performed.

## **Riassunto**

La microfluidica è una recente area di ricerca che si occupa di processare piccoli volumi di fluidi in canali di dimensioni micrometriche. La processazione di fluidi in tali canali ha fatto sì da sviluppare metodi per la fabbricazione di sistemi miniaturizzati più o meno complessi, come i lab-on-chip, ed ha aperto nuove ed innumerevoli possibilità per la progettazione di saggi su larga scala di potenziale interesse a livello industriale. Tali microcomponenti permettono di realizzare una serie di funzioni specifiche, dalle più semplici quali il trasporto o il dosaggio di un fluido a quelle più complicate quali il mescolamento, l'analisi e la sintesi di fluidi e miscele di fluidi anche complesse. Il recente interesse verso la microfluidica, o più in generale verso le microtecnologie, è dovuto ai grossi vantaggi che essa garantisce: si pensi ad esempio alla progettazione di sistemi compatti con una notevole diminuzione del loro peso e ingombro, e quindi un'elevata portabilità, alla più facile gestibilità delle operazioni da controllare, che porta quindi ad una maggiore sicurezza, al ridotto utilizzo di reagenti, per lo più molto costosi, e al ridotto tempo di analisi.

L'obiettivo di questo lavoro di tesi è lo studio del processo di emulsificazione, e più in generale di miscelamento, in microsistemi, quali microcapillari o micromiscelatori statici e la formulazione, tramite differenti tecniche, di emulsioni stabili nel tempo.

## **Flusso di emulsioni in microcapillari**

Nella prima parte di questo lavoro di tesi l'attività di ricerca si è concentrata sullo studio della fluidodinamica di emulsioni in microcapillari e sull'analisi della velocità e della deformabilità delle gocce della fase dispersa in flusso.

### Materiali

I materiali utilizzati per le prove sperimentali sono quattro: acqua distillata, olio minerale e due surfattanti non ionici, uno di natura idrofila e l'altro di natura idrofoba. La scelta di due surfattanti, ossia un "blend", e non di un tensioattivo singolo, è legata a delle evidenze sperimentali che confermano un miglioramento nelle caratteristiche del film interfacciale e della stabilità dell'emulsione rispetto al caso in cui si utilizzi un solo surfattante.

### Apparato sperimentale

Per lo studio fluidodinamico delle emulsioni tramite microscopia ottica è stata progettata una cella di flusso costituita da due lastre di plexiglass trasparente separate da uno spaziatore di gomma. Sulla lastra inferiore della cella di flusso sono stati alloggiati, in parallelo, dei microcapillari di vetro (Figura 1-b) con diametro compreso tra 5 e 50  $\mu\text{m}$ . I due fori presenti sulla lastra superiore della cella di flusso sono collegati a due tubi di gomma, connessi agli estremi liberi a due beaker contenenti l'emulsione, preparata precedentemente in un agitatore magnetico.

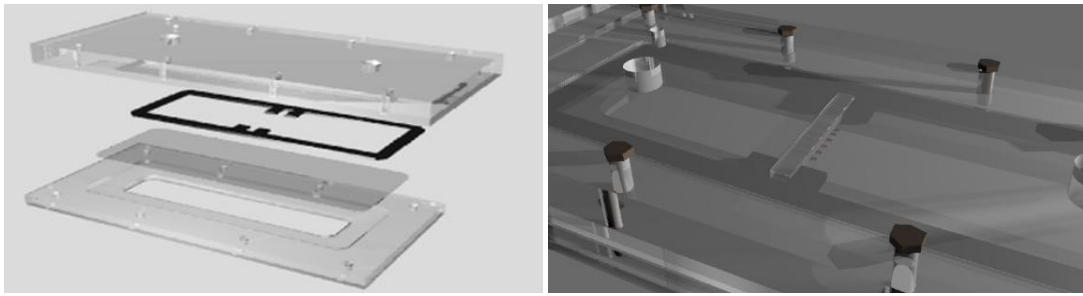


Figura 1: (a) Componenti della cella di flusso; (b) microcapillari di vetro

Lo studio dei parametri relativi alla deformazione e alla velocità delle gocce della fase dispersa durante il flusso nel microcapillare è stato effettuato al computer sulle immagini a disposizione acquisite in tempo reale tramite l'ausilio di una videocamera ad alta velocità connessa ad un microscopio ottico.

### Risultati

Ogni esperimento, è stato preceduto dall'osservazione dell'emulsione in condizione statiche tramite microscopio elettronico a scansione ambientale (figura 2, sinistra) e microscopio ottico (figura 2, destra). Si è potuto così notare che l'emulsione presa in esame è un'emulsione multipla, cioè un sistema polidisperso nel quale, microgocce della fase disperdente sono intrappolate in gocce della fase dispersa, le quali sono a loro volta disperse nella fase continua.

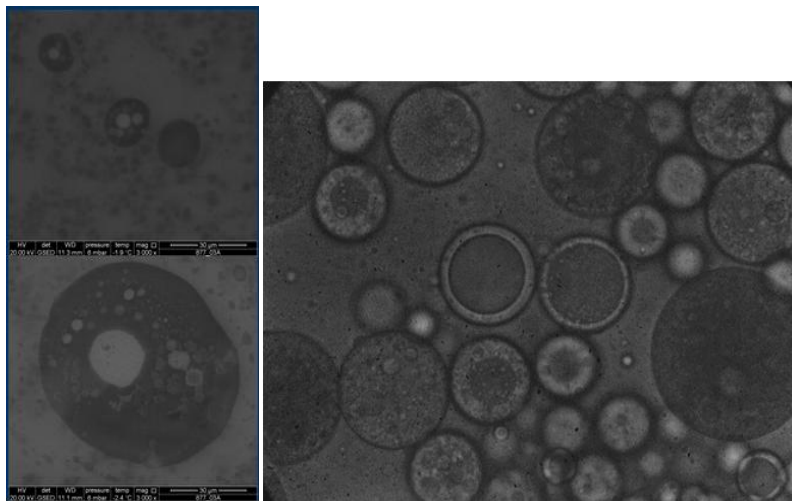


Figura 2: Immagini statiche dell'emulsione; ESEM (sinistra), microscopio ottico (destra)

Dopo l'osservazione in statico si è proceduti al calcolo della velocità dell'emulsione in flusso in un capillare da 50  $\mu\text{m}$  a diversi battenti.

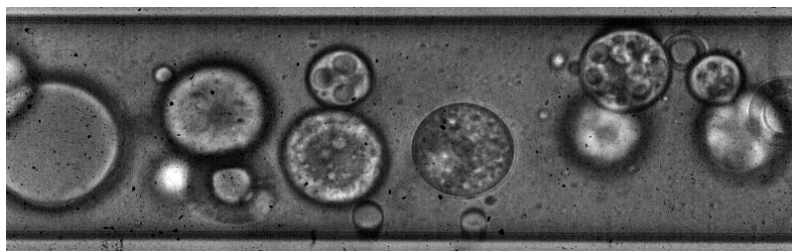


Figura 3: Emulsione in flusso in un capillare da 50  $\mu\text{m}$

Per ogni battente si è realizzato un grafico della velocità sperimentale di tutte le gocce esaminate in funzione della loro posizione radiale, ottenuta come la differenza del centro y di ogni goccia rispetto al centro y del capillare. Da tale grafico si è avuta conferma che l'emulsione nel capillare in regime laminare, ha un profilo di velocità di tipo parabolico, in accordo con la legge di Poiseuille (eq.1). Successivamente, sfruttando tale legge:

$$Q = \frac{\pi r^4 \Delta p}{8 \eta L} \quad \text{Eq. 1}$$

e noti i  $\Delta p$ , la lunghezza  $L_{\text{cap}}=0.407\text{cm}$ , il raggio  $r=25\mu\text{m}$  del capillare e la viscosità dell'emulsione  $\eta=2.5 \cdot 10^{-3} \text{Pa}\cdot\text{s}$ , precedentemente misurata con un viscosimetro a capillare di tipo Ubbelohde, è stato possibile calcolare la portata, e quindi la velocità media e massima teorica delle gocce analizzate, e confrontare tali valori con quelli sperimentali. Da dati di letteratura, è noto che in un'emulsione la velocità delle gocce piccole è approssimabile a quella della fase continua. In figura 4 è mostrato il profilo di velocità in funzione della posizione radiale (l'origine corrisponde al centro del capillare) a diversi battenti. Fittando i dati sperimentali con la legge di Poiseuille si trova un valore di viscosità pari circa a 2 mPa·s, paragonabile alle misure ottenute con il viscosimetro a capillare. Tale accordo mostra che tale cella di flusso può essere usata come un vero e proprio viscosimetro.

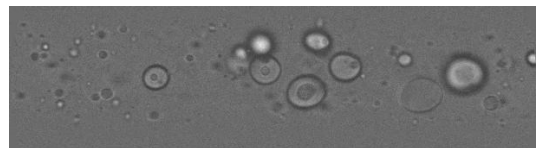
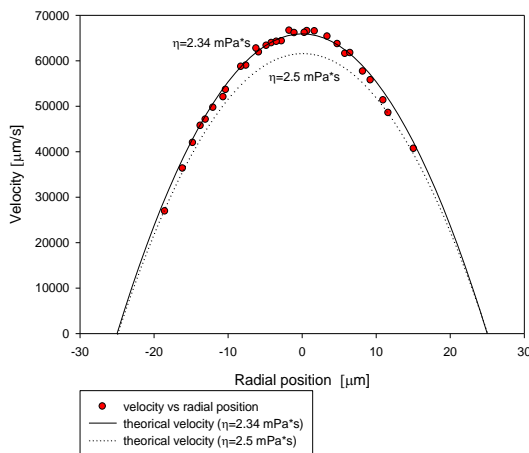
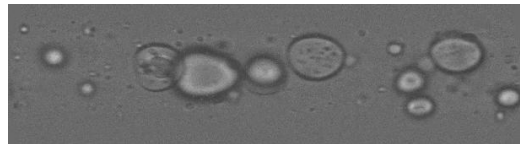
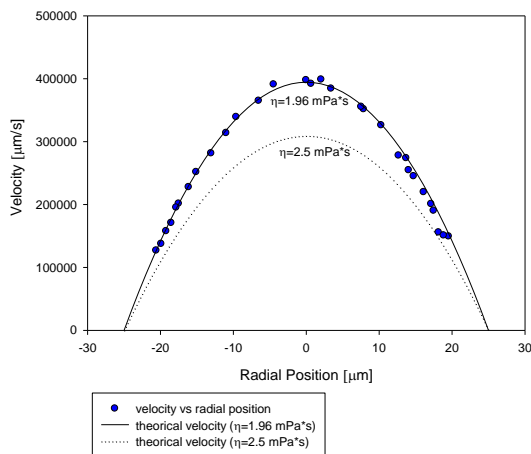


Figura 4: Profilo di velocità in funzione della posizione radiale e immagine dell'emulsione in flusso in capillare da  $50 \mu\text{m}$  a diversi battenti; (in alto)  $\Delta p=205.5 \text{ cmH}_2\text{O}$ , (in basso)  $\Delta p=41 \text{ cmH}_2\text{O}$

Le conoscenze acquisite sul comportamento fluidodinamico delle emulsioni possono essere utilizzate come modello per comprendere il flusso del sangue in microcapillari. Il sistema semplificato di una goccia in flusso confinato è confrontabile con quello dei globuli rossi nello stesso regime di flusso, di cui sono state effettuate analisi quantitative di velocità e deformabilità (figura 4).

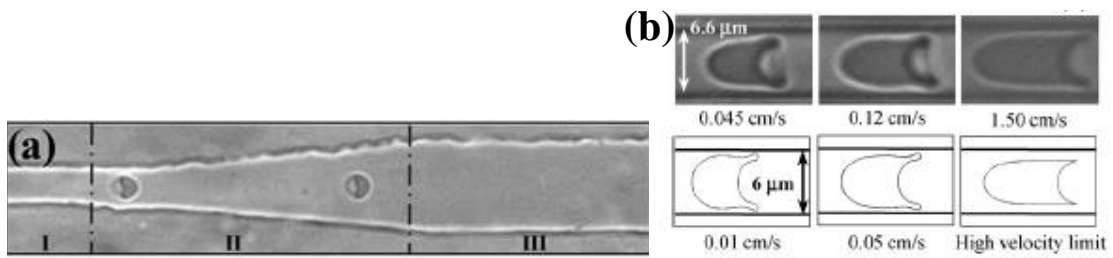


Figura 4: a) profilo di velocità in un canale divergente; b) forma di globuli rossi in capillare da 6.6 μm e confronto con dati di letteratura

### Processo di emulsificazione per inversione di fase

Il metodo dell'inversione di fase, durante il quale un'emulsione di olio in acqua diventa di acqua in olio e viceversa, permette di preparare emulsioni finemente disperse e stabili per lungo tempo. Il processo di emulsificazione mediante tale metodo è stato studiato ed emulsioni stabili nel tempo, con finissima distribuzione di particelle sono state formate. In figura 5 è mostrata l'immagine di un'emulsione preparata tramite inversione di fase e la sua distribuzione media di diametri conferma la dimensione piccolissima delle particelle ( $d_{\text{medio}} \sim 0.17 \mu\text{m}$ ).

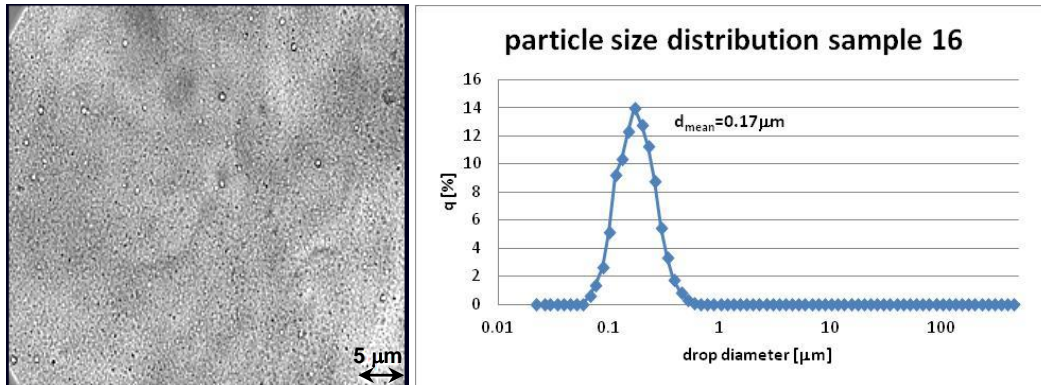


Figura 5: immagine di un'emulsione stabile e distribuzione media dei diametri

L'inversione di fase di un'emulsione può essere dimostrata da misure di conducibilità elettrica, la quale risulta essere molto bassa per emulsioni di acqua in olio, poichè l'olio, al contrario dell'acqua, conduce la corrente elettrica in misura estremamente ridotta, e viceversa per avviene per emulsioni di olio in acqua. Di conseguenza un salto nel valore della conducibilità durante l'inversione è prevedibile e mostrato in figura 6.

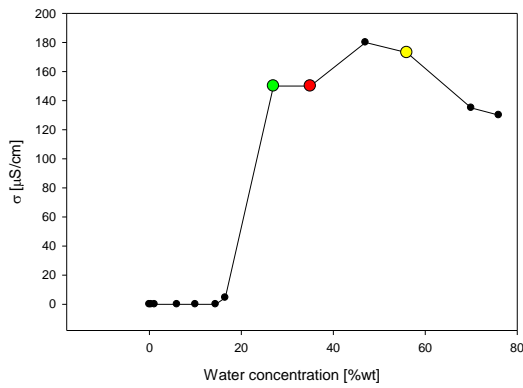


Figura 6: conducibilità elettrica in funzione della concentrazione di acqua

Per comprendere la morfologia delle emulsioni durante l'inversione di fase si è utilizzato un microscopio confocale e un colorante fluorescente solubile in acqua, la Rodamina B, che permette di distinguere la fase acquosa da quella oleosa. In figura 7 l'evoluzione della microstruttura dell'emulsione a diverse concentrazioni di acqua; la prima immagine risulta nera in quanto non c'è acqua, e quindi Rodamina che fluoresce, e poi, all'aumentare della concentrazione di acqua si formano prima delle gocce di acqua in fase oleosa fino all'inversione di fase, a circa il 50% di H<sub>2</sub>O, in cui si sono formate gocce di olio in acqua.

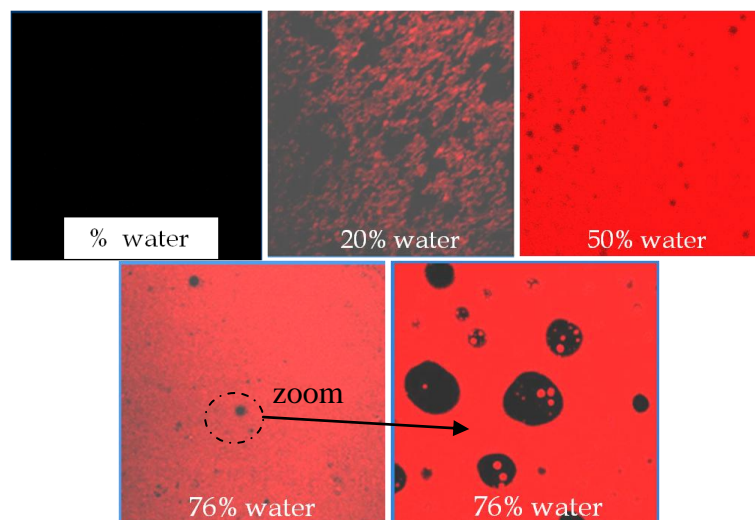


Figura 7: morfologia dell'emulsione al variare della concentrazione di acqua

### Flusso di emulsioni in micromiscelatori statici

I risultati sperimentali del flusso di emulsioni in microreattori, in particolare in micromiscelatori statici, sono presentati nell'allegato confidenziale di tale lavoro di tesi.

## Conclusioni

In conclusione, i risultati raggiunti in questo lavoro di tesi di dottorato possono essere così riassunti:

- Studio del flusso di emulsioni in microcapillari
- Messa a punto di una tecnologia tipo microfluidics per simulare la fluidodinamica del sangue nella microcircolazione
- Messa a punto di un sistema costituito da micromiscelatori statici per studiare il processo di miscelamento ed in particolare di emulsificazione ed influenza della viscoelasticità sull'efficienza del miscelamento
- Studio del processo di emulsificazione mediante inversione di fase
- Messa a punto di un sistema costituito da micro miscelatori statici per il miscelamento di due liquidi immiscibili e scale-up dei microreattori.

# Chapter 1 EMULSIFICATION

## 1.1 INTRODUCTION

Emulsions are unstable systems of two immiscible liquids in which a first phase is dispersed into a second one in form of small droplets. They are of great significance in our daily life covering various products from food, pharmaceutical, cosmetics, and other chemical industries. Some examples of important and familiar emulsions are those occurring in foods (milk, mayonnaise, etc.), cosmetics (creams and lotions), pharmaceuticals (soluble vitamin and hormone products), and agricultural products (insecticides and herbicide emulsion formations). Emulsions are very unstable, so they don't form spontaneously and tend to revert to the stable state of the fully separated phases over time. In order to stabilize the dispersion, an emulsifying agent is added, with the effect of decreasing the interfacial tension between the two phases and of a good stability in time.

Interfacial tension is the force per unit length (N/m) existing at the interface between two immiscible liquid phases; if liquids are completely miscible, no interfacial tension exists between them. When two different phases (gas/liquid, liquid/liquid, gas/solid or liquid/solid) are in contact with each other the molecules at the interface experience an imbalance of forces. This will lead to an accumulation of free energy at the interface. The excess energy is called surface free energy and can be quantified as a measurement of energy/area i.e. the energy required to increase the surface area of the interface by a unit amount. It is also possible to describe this situation as having a line tension or interfacial tension (IFT), which is quantified as a force/length measurement

A very common class of emulsifiers, known as surface active agents or surfactants, is able to modify the interfacial properties of the liquids in which they are present. The peculiar properties of these molecules is their amphiphilic character, thus they contain both hydrophobic and hydrophilic groups (Fig.1-1) and concentrate at the interface separating immiscible phases, thereby decreasing the interfacial tension.

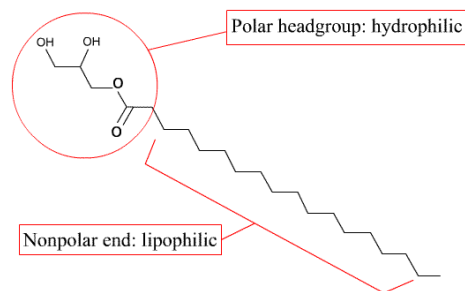


Fig.1-1: Surfactant molecule

In general a droplet tends to be spherical because this shape minimizes the energetically contact area between the oil and the aqueous phases; changing the shape of a droplet, or breaking into a number of smaller droplets, increases this contact area and therefore requires an input of energy. The interfacial force responsible for keeping a droplet in a spherical shape is characterized by the Laplace Pressure:  $\Delta P_L = 4\sigma/d$

where  $\sigma$  is the interfacial tension and  $d$  is drop diameter. So to deform and break a droplet, it's necessary to apply an external force that is much higher than the interfacial tension  $\sigma$ .

The ratio between the external force and the Laplace Pressure could be defined as a dimensionless number, the Capillary number:  $Ca = \tau d / \sigma$ .

The nature of these disruptive forces that act on a droplet depends on the flow condition it experiences (laminar, turbulent, transitional), besides to break up a droplet, these forces must exceed the interfacial tension and their duration must be longer than the critical time required to deforming and disrupting the droplet.

Depending on the nature of the hydrophilic moiety ensuring the water affinity of the molecule, major surfactants can be divided into ionic, anionic, cationic, non-ionic classes and zwitterionic. A non-ionic surfactant has no charge groups in its head. The head of an ionic surfactant carries a net charge. If the charge is negative, the surfactant is more specifically called anionic; if the charge is positive, it is called cationic. If a surfactant contains a head with two oppositely charged groups, it is termed zwitterionic

Regarding the hydrophobic moiety of the molecule, it is a hydrocarbon chain in most common surfactants; however, in some more specialized surfactants, this hydrophobic part can be a nonhydrocarbon chain such as a polydimethylsiloxane or a perfluorocarbon.

In principle two types of emulsions are readily distinguished, depending upon the liquid that forms the continuous phase as shown in figure 1-2: oil-in-water (o/w) emulsion, where oil droplets are dispersed in continuous water and water-in-oil (w/o) emulsion where water droplets are dispersed in continuous oil.

In addition there are multiple emulsions (O/W/O or O/W/O), which are complex systems where both water - in - oil (W/O) and oil - in - water (O/W) emulsion types exist simultaneously. In the case of water - in - oil - in - water multiple emulsions, the oil droplets have smaller water droplets within them and the oil droplets themselves are dispersed in a continuous water phase. Oil - in - water - in - oil multiple emulsions, on the other hand, consist of tiny oil droplets entrapped within larger water droplets, which in turn are dispersed in a continuous oil phase. Multiple emulsions typically require two or more emulsifiers, one that is predominately hydrophobic stabilizing the primary W/O emulsion and one that is predominately hydrophilic stabilizing the secondary O/W emulsion. The hydrophobic and hydrophilic emulsifiers are added to the oil and continuous aqueous phases, respectively.

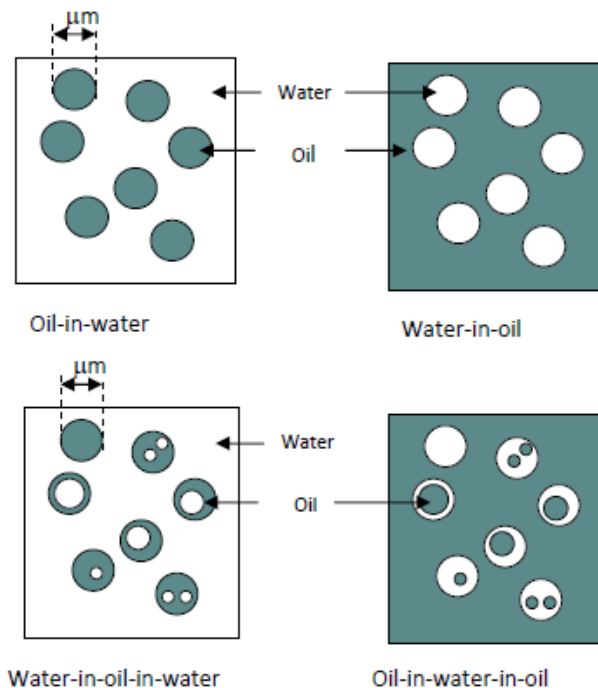


Fig.1-2 Schematic representation of different emulsions

Whether an emulsion turns into a water-in-oil emulsion or an oil-in-water emulsion depends on the volume fraction of both phases and on the type of emulsifier.

Generally, the Bancroft rule applies: surfactants tend to promote dispersion of the phase in which they do not dissolve very well; for example, proteins dissolve better in water than in oil and so tend to form oil-in-water emulsions (Bancroft, 1913).

A more sophisticated criterion was proposed by Griffin (1954), who introduced the concept of hydrophilic-lipophilic balance (HLB). As far as emulsification is concerned, surfactants with an HLB number in the range from 3 to 6 must form water-in-oil (w/o) emulsions, whereas those with HLB numbers from 8 to 18 are expected to form oil-in-water (o/w) emulsions. The HLB system is particularly useful to identify surfactants for oil and water emulsification, if more than one surfactant is present in the system, the HLB will be the weighted average of the HLB values for each component.

## 1.2 STABILITY

There are two principal types of stability for colloidal emulsions. The first type is droplet stability and is common to all emulsions, whether colloidal or not. Without droplet stability, the oil droplet would demix, destroying the emulsion. Droplet stability is dependent on the bulk properties of the fluids and the nature of the surfactant. For colloidal emulsions, the second type of stability is dispersion stability. As in other colloidal suspensions, dispersion stability is stability against aggregation or flocculation. The two principle mechanisms which destroy the droplet stability are coarsening and coalescence. Coarsening is dependent primarily on the solubility of the dispersed phase in the continuous phase, whereas coalescence is dependent on the degree of repulsion provided by the surfactant at the droplet interfaces. Coarsening involves an increase in the average size of the emulsion droplets due to the solubility of two phases. Transfer of the dispersed phase from smaller to larger droplets is driven by their differences in the Laplace pressure, provided the solubility is significant. The small droplets continue to decrease in size until they disappear, because their interfacial pressure increases as they get smaller. The big droplets around them become even larger as they receive molecules from the smaller droplets. The growth of these larger droplets through coarsening is also known as Ostwald ripening. The rate of molecular diffusion through the interface is also dependent on the interfacial barrier created by the surfactant (Leal-Calderon et al., 2007).

Coalescence is the abrupt rupturing of the film of continuous phase between droplet interfaces. When two droplets of the dispersed phase approach each other, they will coalesce, thereby reducing their total interfacial area, unless repulsion between the droplet interfaces inhibits this process. To prevent coalescence, a surfactant must provide effective repulsion between droplet interfaces. The repulsion is dependent on the surfactant concentration on the interface, and a minimum surfactant concentration, which depends on the chemistry of the surfactant, is usually necessary to prevent coalescence. If the surfactant provides only weak repulsion, the droplets will coalesce and the dispersed phase will demix, destroying the emulsion (Leal-Calderon et al., 2007).

By choosing fluids that are extremely insoluble and using an appropriate surfactant, one can render emulsion droplets stable over many years. For such emulsions, measurements of their properties can be made over time scales which are negligible compared to the time scale of the droplet stability.

Dispersion stability is defined for any particulate suspension of colloidal particles. It refers to the stability of the dispersion against macroscopic phase separation (Russel et al., 1989). Dispersion stability in emulsions means that the droplets do not aggregate or flocculate. Each droplet has an entropic thermal energy of roughly  $kBT$ , where  $kB$  is Boltzmann's constant and  $T$  is the absolute temperature. This energy drives Brownian

motion of the droplets and keeps them dispersed, provided it is larger than microscopic interdroplet attractive energies.

If the mass density of the dispersed phase is smaller than that of the continuous phase, the droplets may cream due to buoyant forces if the Brownian forces are smaller. The creaming rate is affected by the droplet size and the viscosity of the continuous phase.

For micron-sized droplets and most common fluids, creaming is noticeable after many weeks. Figure 1-3 shows schematically different instability in emulsion systems (Tadros, 2005).

The study of emulsions' stability is fundamental for the definition of emulsion itself.

One of the methods for evaluation of emulsion stability is to monitor the changes in the mean drop size for a certain period of storage time. It is often considered that an increase of drop size with time is a clear indication for emulsion destabilization. Such a relation is quite understandable (at a first glance) for at least two reasons:

- (1) the increase of drop size reflects an ongoing coalescence process inside the emulsion
- (2) as shown in previous studies, the stability of emulsions containing larger drops is lower at equivalent other conditions.

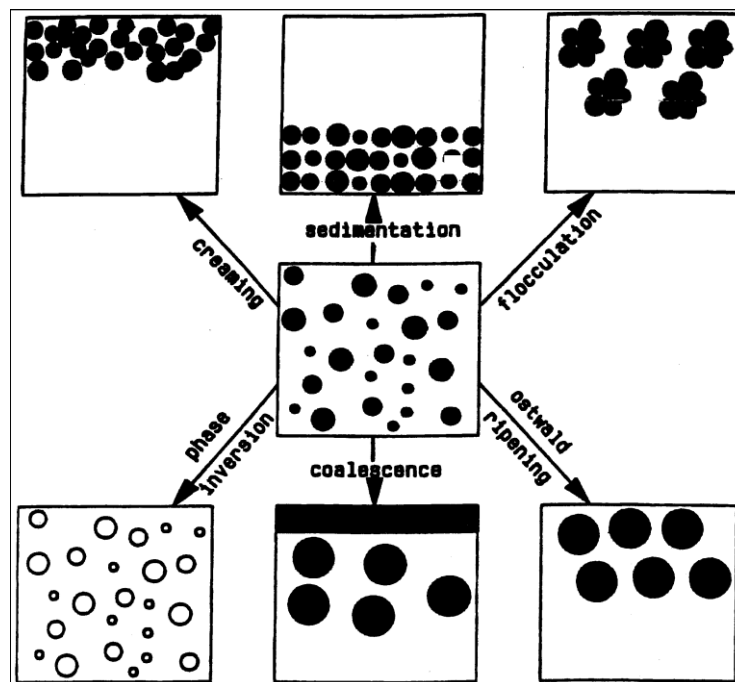


Figure 1-3: Schematic of the emulsion breakdown processes (Tadros, 2005)

### 1.3 EMULSIFICATION DEVICES

Emulsions are unstable and so don't form spontaneously, then energy input is needed. A lot of research has been carried out aimed at making the emulsification process more efficient. To evaluate the effectiveness of the process, various parameters have to be considered like the production rate, the disperse phase fraction, the energy efficiency. All of them depend on the raw materials and on the device used for mixing. According to

literature emulsions can be prepared by high energy or low energy emulsification methods. The first one requires the use of large mechanical energy generated by high pressure homogenizers or high pressure systems connected to static mixers in order to produce fine droplets. The second one uses the chemical energy stored in the ingredients and produce emulsions almost spontaneously by inverting, for example, the curvature of surfactants by changing the experimental temperature (phase inversion temperature, PIT method). The evolution of the mean drop size during emulsification is governed by two opposite processes: drop breakage and drop-drop coalescence. At high emulsifier concentration the coalescence is negligible and the drop size distribution is determined exclusively by the process of breakup. So the essential process is not droplet formation, but droplet breakup, thus in order to deform the drop, an external stress larger than Laplace Pressure has to be applied.

In this thesis emulsification in batch and through static mixers at high energy has been performed (Fig. 1-4).



Figure 1-4: Devices used for emulsification: beaker on a magnetic stirrer (left side) and static mixers (right side)

## 1.4 PRINCIPLES OF RHEOLOGY

Rheology is the science of deformation and flow of materials, with the materials under consideration being solids or fluids, including liquids and gases. Materials can deform in a different way when a force is applied. The deformation is said to be elastic if the material returns to its original size and shape upon removal of the applied load and the degree of deformation, also called strain  $\gamma$ , is proportional to the applied force or stress  $\tau$ . On the other hand, it is referred to as inelastic deformation if the application of the mechanical load results in a permanent change in the dimensions of the material, i.e., it doesn't return to its original size and shape even if the mechanical load is no longer being applied to it. These materials have a viscous (or plastic) behaviour. Fluids continuously deform - or flow - as a result of the application of external forces. Then there are some materials that have a combination of fluid-like and solid-like behavior and are called viscoelastic fluids. An example of viscoelastic fluid is blood; its behavior is basically due to the elastic energy that is stored in the deformation of red blood cells as the heart pumps the blood through the body. The energy transferred to the blood by the heart is partially stored in the elastic structure, another part is dissipated by viscosity, and the remaining energy is stored in the kinetic motion of the blood.

The stress  $\tau$  can have several components, including shear stress, the force per unit area acting parallel to the surface, and normal stress, the force per unit area acting perpendicular to the surface. The latter is defined as pressure in a fluid. The strain  $\gamma$  can also have various components associated with the different stress components. For example, shear stress results in shear strain, in which the layers of material move parallel to each other in a continuous manner. During slow flow in a tube the pressure drop (reflecting the resistance to flow) is proportional to the speed of flow. Under these conditions, it has been observed that the liquid particles move smoothly in adjacent planes (laminae) parallel to the tube wall; this type of flow is called *laminar flow*. With increasing flow rate, there is a tendency for the fluid flow to become irregular, with fluid moving in swirls and irregular patterns. This type of chaotic flow is termed turbulent, with the degree of turbulence increasing with flow rate. Under such turbulent conditions, the pressure drop is proportional to the square of the speed of flow, and thus for the same pipe and fluid, resistance to flow is greater with turbulence than it is for laminar flow. Under laminar flow conditions, a shear stress - shear rate relationship is used to define the fluidity of liquids. This relationship reflects the internal resistance between fluid layers (laminae) and thus reflects the viscosity of the fluid; the viscosity of a liquid can be calculated by dividing the shear stress by the shear rate. From a rheological point of view, liquids can be divided into two main groups (Figure 1-5):

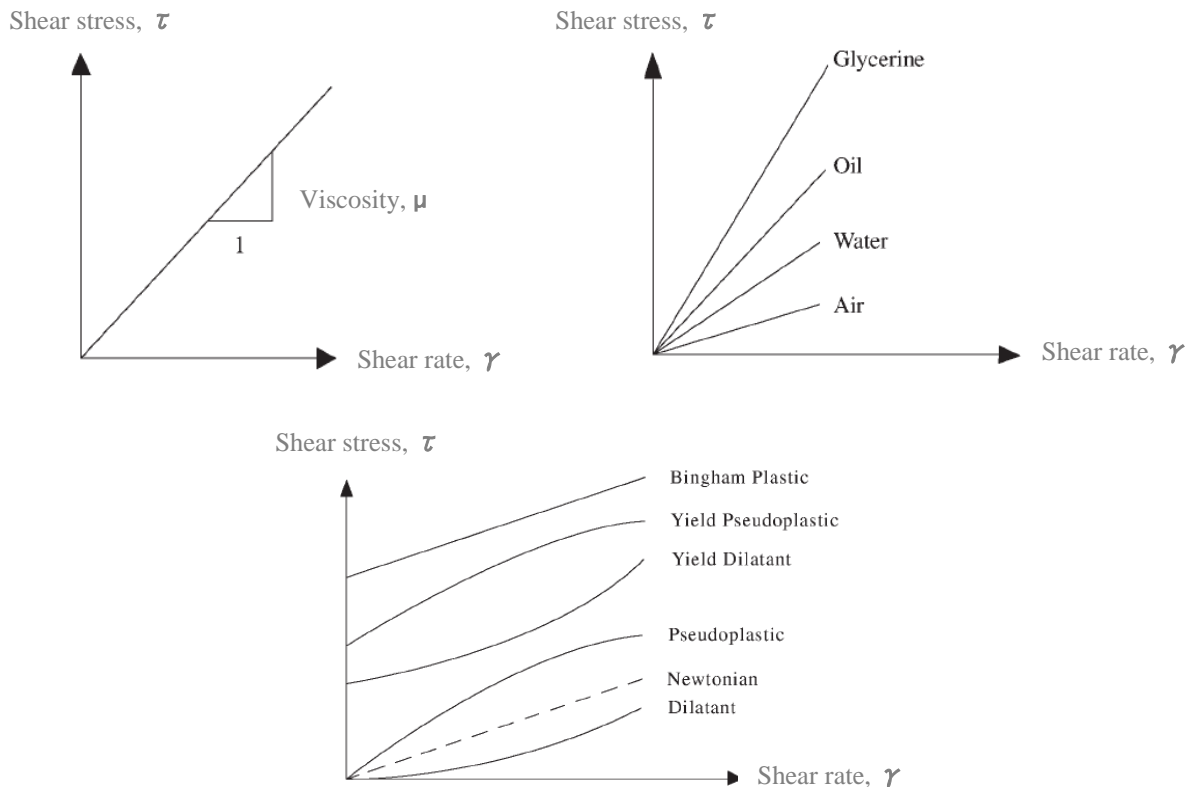


Figure 1-5: Shear stress – shear rate and viscosity – shear rate relations for Newtonian and non-Newtonian liquids

1. In Newtonian liquids, the viscosity is independent of variations in shear rate or shear stress. For these fluids the slope of the shear stress–shear rate relation is constant over the range of shear stress examined, and thus the viscosity is constant.
2. In non-Newtonian liquids, the apparent viscosity is not a constant but it depends on the magnitude of the shear stress or shear rate and can be calculated as the ratio of shear stress to shear rate. The viscosity of a non-Newtonian fluid may decrease (shear - thinning behavior) or increase (shear - thickening behavior) as the shear rate is increased. Non-

Newtonian liquids may have a yield stress below which the shear rate is zero (no shear flow), resulting in an infinite value for apparent viscosity. The flow behavior of non-Newtonian liquids may also be time dependent; the viscosity of a thixotropic liquid decreases with time at a fixed shear rate. For both classes of fluids, the viscosity of a liquid depends on its temperature, and for most fluids viscosity decreases with increasing temperature.

Several units have been used for viscosity, with the most common being milliPascal-s (mPa·s), which is numerically equal to centipoise (cP); water at 20°C has a viscosity of 1.0 mPa·s or 1.0 cP.

Viscoelasticity of fluids can be studied by dynamic mechanical analysis where an oscillatory force (stress  $\tau$ ) is applied to a material and the resulting displacement (strain  $\gamma$ ) is measured. The particular behaviour of these fluids can be expressed by the storage modulus  $G'$  representing the elastic response and loss modulus,  $G''$ , representing the viscous behaviour of the material. In general  $G'$  and  $G''$  are measured as a function of the angular velocity  $\omega$  by oscillatory measurements.

The viscosity and viscoelasticity of a liquid can be measured by a viscometer, which is a device built for studying stress – strain relations. Capillary viscometers are widely used devices for measuring viscosity of Newtonian liquids. The working principle of a capillary viscometer is based on the measurement of flow rate of the liquid through a well-defined capillary tube under a certain pressure difference; at constant temperature and pressure difference, the flow rate decreases with increasing viscosity. Capillary viscometers can also be used for flow measurements of non-Newtonian liquids, but estimation of viscosity is difficult because the shear rate varies across the diameter of the tube (i.e., maximum at the wall, zero at the center). Rotational viscometers of various types are thus more commonly used for studying non-Newtonian liquids. In a rotational viscometer, the liquid under investigation is sheared between two surfaces, either under constant shear stress or shear rate, and the response (resulting shear rate or shear stress, respectively) is measured. The geometric design of the shearing portion varies among instruments but is usually designed to provide a uniform shear rate or shear stress throughout the sample being studied. Viscosimeters can also be operated in an oscillating mode to measure elastic properties of fluids.

## 1.5 FLUID DYNAMICS OF DEFORMABLE DROPS

A droplet-based microstructure is found in most liquid-liquid industrially relevant systems, such as emulsions, polymer blends and foodstuff, which enjoy a variety of applications in everyday life. These systems, starting from the pioneering work of Taylor on the deformation of droplets in simple shear flow, have attracted much scientific interest in different fields, from fluid mechanics to geophysics. The study of the flow behaviour of droplets is more complicated in concentrated systems due to hydrodynamic interactions between the droplets and to coalescence phenomena, and in complex flow geometries, where both shear and extensional components can be present in a time-dependent manner. In fact, the rheological properties of these systems are linked to the flow conditions by a complex interplay, since a flow-induced change of microstructure can in turn affect the viscosity of the flowing mixture.

To get some insight on this problem a basic approach has been followed in the literature, where the idealized situation of an isolated droplet in a well-defined flow field has been considered. In spite of the gross simplifications associated with this approach, many significant results and some fundamental understanding have been obtained by studying

the flow behaviour of an isolated droplet under simple shear or elongational flow, as reviewed in several papers. Here, we focus on Poiseuille flow in cylindrical and rectangular channels, which is a somehow more complex problem due to the presence of a shear rate gradient in the flow geometry. This is also a quite interesting case being close to flow conditions encountered in industrial processing (such as in fluid transport and mixing operations). Another possible application is in the study of oil recovery from porous media, which can be modeled as made of a channel network (Olbricht et al, 1996). Furthermore, Poiseuille type of flow is found in microfluidics devices, where the effect of confinement is quite significant. The motion of droplets under confined flow has also attracted some interest due to the similarities with the shape taken by red blood cells in microcapillaries. The classical fluid dynamic problem is given by an isolated drop in a simple shear flow field, where the only intrinsic length scale is the undeformed drop radius  $R_0$ . When the drop is sufficiently small with respect to any typical dimension  $L$  of its ambient of motion, i.e., when  $R_0 \ll L$ , the “outer” dynamics is dictated by the undisturbed flow. In this simplest case, one assumes that the drop is suspended in an unbounded fluid, and the undisturbed velocity field “at infinity” is linear. Another usual assumption is that the Reynolds number of the fluid motion governing the deforming drop is low (Eq. 1)

$$\text{Re} = \frac{\rho \cdot v \cdot R_0}{\eta} \ll 1 \quad \text{eq.1}$$

with  $\rho$  and  $\eta$  the density and viscosity of the external fluid, respectively.

To keep the situation as simple as possible, external and buoyancy forces are assumed negligible, the two fluids are taken to be incompressible and mutually immiscible, and isothermal conditions hold. In such a case, the two nondimensional parameters governing drop shape and stability are the ratio of shear and interfacial stresses, expressed by the capillary number (Eq. 2) where  $\eta_c$  is the continuous phase viscosity,  $\dot{\gamma}$  is the shear rate,  $\sigma$  is the interfacial tension, and the viscosity ratio  $\lambda$  (Eq. 3) is the ratio between drop and continuous phase viscosity.

$$\text{Ca} = \frac{\eta_c \cdot R_0 \cdot \dot{\gamma}}{\sigma} \quad \text{eq.2}$$

$$\lambda = \frac{\eta_d}{\eta_c} \quad \text{eq.3}$$

Typical stationary drop images at low to moderate drop deformations are shown in Figure 1-6a for the lateral view (along the vorticity axis), and in Figure 1-6b for the top view (along the velocity gradient). In the images, the most significant (and readily observable) geometric parameters are also shown, namely: i) (Figure 1-6a) the maximum and minimum distances  $R_{\text{MAX}}$  and  $R_{\text{MIN}}$  of the contour from the drop centre, and the angle  $\varphi$  between  $R_{\text{MAX}}$  and the shear direction  $x$  in the lateral view; ii) (Figure 1-6b) the maximum and minimum distances  $R_P$  and  $R_Z$  of the contour from the drop centre in the top view. In both views, the drop contour is very well approximated by an ellipse.

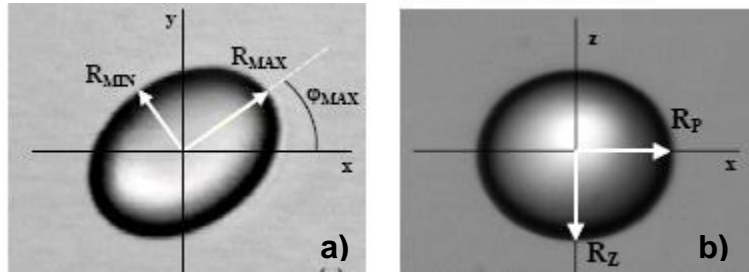


Figure 1-6: Side view (a) and top view (b) images of a drop during shear

A parameter that describes drop deformation is the so-called deformation parameter  $D$  (Eq. 4), originally introduced by Taylor.

$$D = \frac{R_{\max} - R_{\min}}{R_{\max} + R_{\min}} \quad \text{eq.4}$$

Hence, the three axes  $R_{\max}$ ,  $R_{\min}$  and  $R_z$ , and the angle  $\phi$  provide a meaningful representation of drop shape.

To better understand the transport of cells or other biological media in capillaries and microfluidic devices, droplet motion in confined geometries is more relevant. The deformation of a droplet in a continuous immiscible liquid phase under micro confined flow is a subject of growing interest in several applications. The current understanding of the effects of confinement on drop deformation, even in well controlled flow fields, is rather limited, and the design issues concerning drop rheological behavior in microdevices are often addressed on an empirical basis. Wall effects on drops deformation are therefore of practical interest, and, as in the case of unconfined flows, the starting point has been the investigation of Newtonian systems.

In the field of biomechanics, the problem that has received considerable attention is the motion of deformable drops through cylindrical tubes. Liquid drops are crude models of red blood cells whose motion is of paramount significance on the physiology of blood flow in the microcapillaries. Although the interface of a red blood cell is considerably more complex than that between two immiscible fluids, the common feature of deformability gives partial reason to extracting information on the former by studying the latter. The dimensionless parameters that govern the motion of a single drop in a cylindrical tube are the Capillary number  $Ca$  (Eq. 5), where  $\eta_c$  is the viscosity of the suspending fluid,  $V$  is the average velocity of the two-phase flow and  $\sigma$  is the interfacial tension between the drop fluid and the suspending fluid; the ratio of the viscosity of the drop fluid to the viscosity of the suspending fluid is  $\lambda$  (Eq. 6), and  $K$  (Eq. 7) is the ratio between the undeformed radius of the drop and the radius of the tube.

$$Ca = \frac{\eta_c \cdot v}{\sigma} \quad \text{eq.5}$$

$$\lambda = \frac{\eta_d}{\eta_c} \quad \text{eq.6}$$

$$k = \frac{a}{R} \quad \text{eq.7}$$

In 1972 Hyman and Skalak have analyzed the axisymmetric flow of a suspension of deformable liquid drops through a rigid cylindrical tube. The liquid in each drop and the suspending fluid have been both assumed to be Newtonian and incompressible, and a surface tension was assumed to act at the interface. The motion was assumed to be sufficiently slow so that inertial terms in the equation of motion may be neglected. Olbricht and Kung (1992) have experimentally studied the motion of drops in straight tubes for an extensive range of parameters. The axisymmetric motion of deformable drops in pressure-driven flow has been considered by Martinez and Udell (1990). The deformation of axisymmetric drops and bubbles moving through straight tubes and constrictions under pressure-driven flow have been studied by Tsai and Miksis (1994) as a function of the capillary number. Using a combination of lubrication theory for the thin film between the drop and the tube wall and a two dimensional boundary-integral representation for the internal flow, Hodges et al. (2004) recently considered the motion of a semi-infinite drop moving through a cylindrical tube. Therefore deformation and breakup of an isolated droop undergoing two-phase confined shear flow was widely described in literature

## 1.5 AIM OF THE THESIS

The objective of this PhD thesis is to study emulsification process to form products stable over time.

Different devices have been examined, starting from microcapillaries of 5-50  $\mu\text{m}$  diameters, to magnetic stirrers, to micromixers of different diameters. For all the materials used a rheological and physical characterization was done in order to study the stability over time.

A suspension of liquid drops could be considered a developing model of blood flow and drops' fluid dynamic can be compared to red blood cells' one.

More in detail, the aims of this work can be summarized as follow:

- Study of fluid dynamic behavior of emulsions in microcapillaries, analyzing the velocity and the deformability of drops, and comparing with the fluid dynamic of red blood cells in microcapillaries
- Formation of stable emulsions and fundamental understanding of emulsification process by phase inversion
- Influence of the viscoelasticity of one of the phases on the mixing efficiency
- Emulsification process and mixing in microsplit and recombine mixers and their scale-up (confidential allegante)

In the first part of the work a novel technique to measure velocity and deformability of drops in confined flow geometries will be presented. The experiments will be carried out on emulsions flowing in silica cylindrical tubes placed in a flow cell and having diameters from 5 to 50  $\mu\text{m}$ . The flow cell was already used to study the fluid dynamics of red blood cells in microcapillaries. Moreover, a silicon-made microfluidic device to study whole blood behavior during the flow in a microchannel network with dimensions and topology similar to the real microcirculation will be setup. Both the techniques will be based on direct

visualization of flowing emulsions by video-enhanced microscopy and automated image analysis procedures to measure cell velocity and deformation. In the confidential allegeate emulsification process in micromixers will be studied and model to predict particle size distribution of stable emulsions will be presented. Scale-up of micromixers of different diameters will be demonstrated.

## Chapter 2 FLOW OF EMULSIONS IN MICROCAPILLARIES

### 2.1 MATERIALS AND METHODS

#### 2.1.1 Materials

Light mineral oil (purchased by Penreco), demi-water and polyoxyethylene sorbitan fatty acid esters (Tween) and sorbitan fatty acid esters (Span) from Sigma Aldrich as emulsifiers were used. The aqueous solution was prepared by dissolving Tween into demi-water at high temperature and the dispersed phase was prepared by mixing Span and a low viscosity mineral oil for few hours.

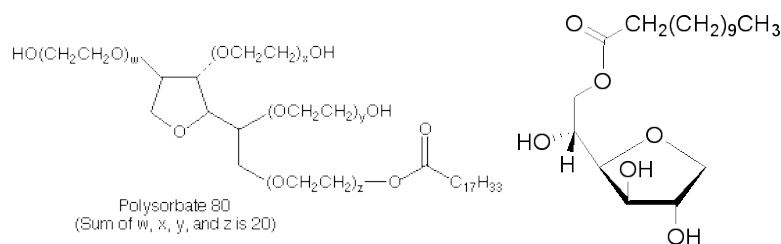


Figure 2-1: Tween80 (left side) and Span20 (right side) configurations

Further specifics about the preparation are present in the allegeate.

#### 2.1.2 Flow cell

The flow cell (Figure 2-2) was made of two Plexiglass plates separated by a rubber spacer. A window was cut in the bottom plate to allow insertion of a coverslip slide for observations at high magnifications with oil immersion objectives.

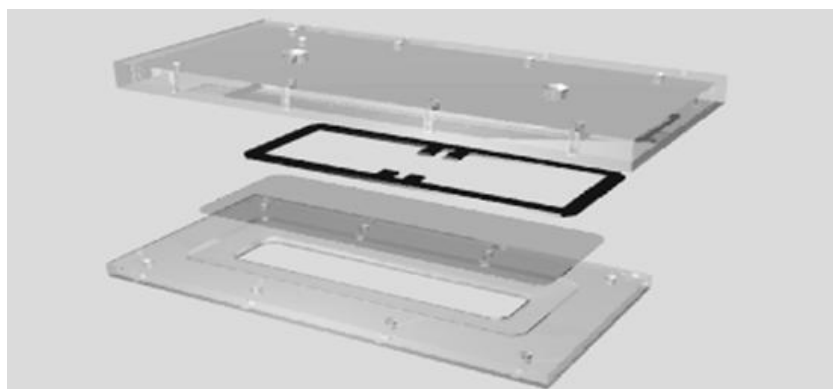


Figure 2-2: Components of the flow cell

The microcapillaries used in this work were made of silica (with 5, 10 and 50  $\mu\text{m}$  ID, Polymicro Technologies). They were cut to about 3-4 mm and then placed in parallel on the flow cell coverslip (Figure 2-3). The diameter and length of all the capillaries used in this work were carefully measured by video microscopy.

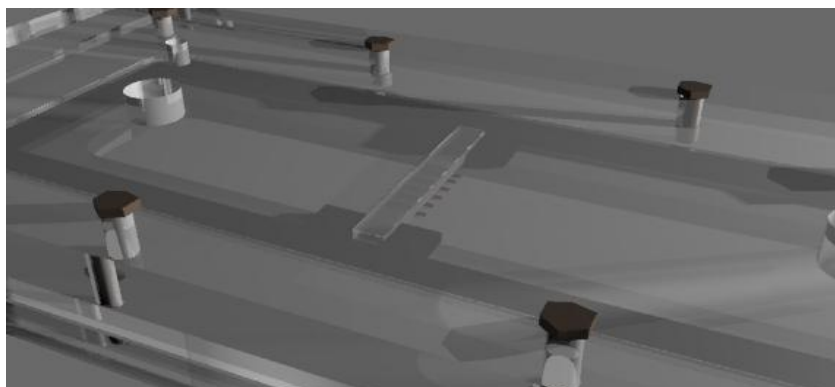


Figure 2-3: Detail of the flow cell: silica tubing

The measurements were carried out by filling the capillaries with an isorefractive silicone fluid to avoid optical distortions. A thin stripe of PDMS (polydimethylsiloxane, Sylgard 184, Dow Corning) has been put on the tubes to avoid optic distortion caused by curvature of tube walls. PDMS was used because it has almost the same refraction index of silica.

The emulsion was fed to the flow cell through an input hole by flexible tubing connected to a glass reservoir. The suspension coming out from the flow cell through an output hole was collected by plastic tubing in another glass reservoir placed on a vertical translating stage. The pressure drop across the microcapillaries was regulated by adjusting the relative liquid levels in the entrance and the exit reservoirs. At the beginning of each experiment the pressure was set to 150  $\text{cmH}_2\text{O}$  for about 5 minutes to fill the tubes with the sample more quickly.

### **2.1.3 Experimental apparatus**

The flow cell was placed on the motorized x-y stage of an inverted microscope (Zeiss Axiovert 100) (Figure 2-4) equipped with a motor assembly for focus control. Sample positioning was controlled by a custom LabView routine. Images of the flowing emulsions were acquired by a high speed (Phantom 4.3, operated up to 4,000 frames/s) that can record clear images of individual drops. Such sharp images of deformed drops enable us to make a quantitative analysis of drops fluid dynamic in the silica microcapillaries.

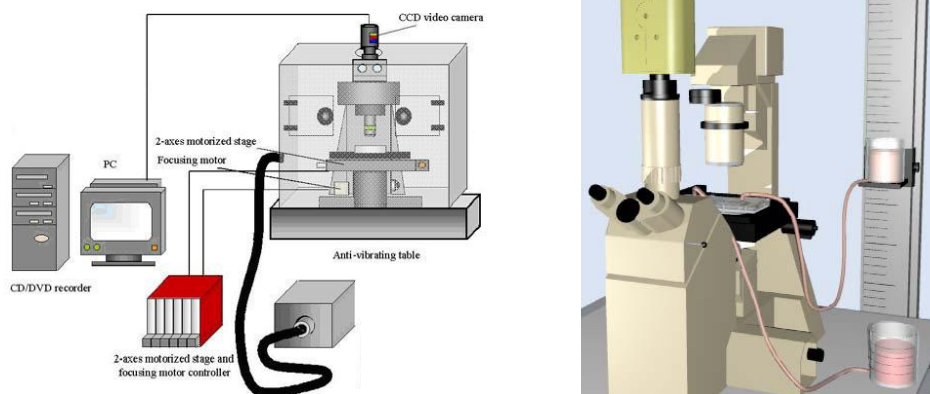


Figure 2-4 Experimental apparatus

The large arrays of images (around 15,000 for each run) recorded by the high speed camera were processed off-line by a custom macro based the library of a commercial software package (Image Pro Plus 4.5) and allowing to isolate the subsets of images with cells passing through the field of view. Other macros were then used to calculate the velocity and shape parameters of each drop. Around 100 drops were analyzed at each pressure drop. In all the experiments, observations were performed in bright field, using short working distance optics (oil immersion objective, 100x Achroplan, Zeiss).

## 2.2 RESULTS

### 2.2.1 Characterization

Observations under static conditions of the emulsion prepared in a beaker with a magnetic stirrer at room temperature were performed. Two different microscopes were used: an optical one (Zeiss Axiovert 100) at low magnification, 20x objective, (Fig. 1 right picture) and an environmental scanning electron microscope (ESEM, Fig. 1 left picture) at higher magnification.

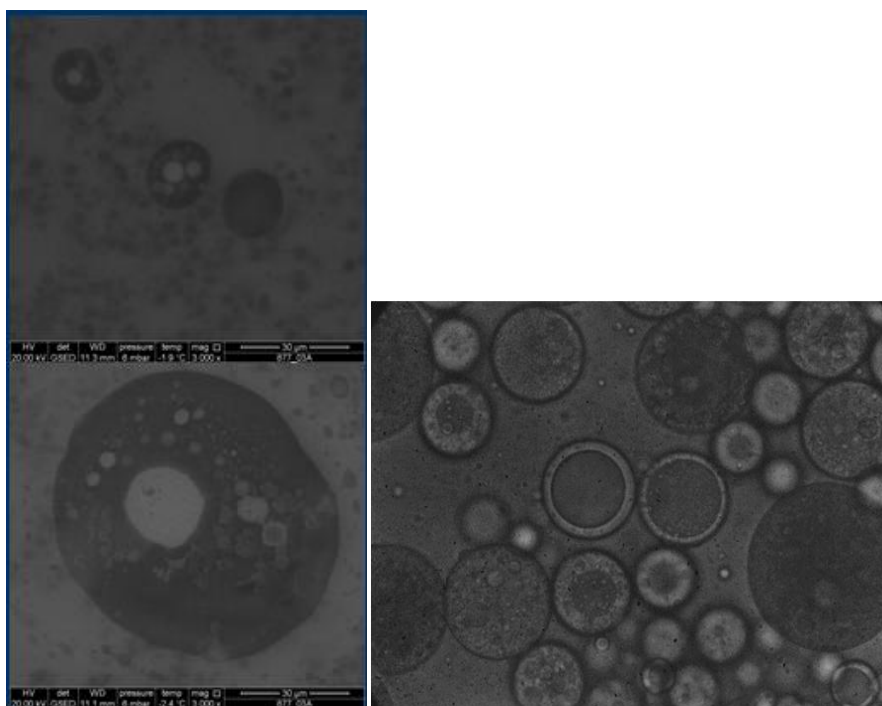


Figure 2-5: Images of drops at rest; ESEM (left picture), optical microscope (right picture)

From the pictures it was clear that the emulsion is not a simple one, but it was indeed a so called multiple emulsion, i.e. it is made of droplets inside droplets. Further investigation to analyze this system was then carried out, because the inclusion or encapsulation process has a potential biotechnological application in the controlled release of a chemical (drug delivery).

Viscosity measurements with Ubbelohde capillary viscosimeters of different diameters (25  $\mu\text{m}$ , 50 $\mu\text{m}$  and 75 $\mu\text{m}$ ) were done. As far as the latter are concerned, the same viscosity

value of 2.5 mPa·s was obtained from the measurements with different capillaries, which shows the Newtonian behavior of the emulsion.

### 2.2.2 Image analysis

Moreover, to characterize the fluid dynamical behavior of this emulsion, the flow cell previously presented with capillaries of different diameters (5  $\mu\text{m}$ , 10  $\mu\text{m}$  and 50  $\mu\text{m}$ ) was used. In Fig. 2-6 a picture of the emulsion flowing in a 50  $\mu\text{m}$  diameter capillary is presented.

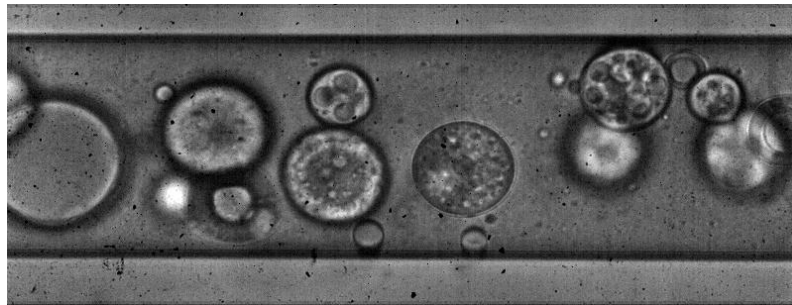


Figure 2-6: Emulsion flowing in a 50  $\mu\text{m}$  diameter capillary

During the experiment, at each pressure drop one movie is acquired. A movie usually contains a number of images (frames) depending on the frame rate imposed by the software; in this experiment the high speed camera operated at about 4000 frames/s. The images were analyzed by image processes techniques to extract quantitative information. For example by knowing drops position frame by frame, a euclidean distance versus time plot (Fig. 2-7) can be generated. The slope of this plot is emulsion velocity.

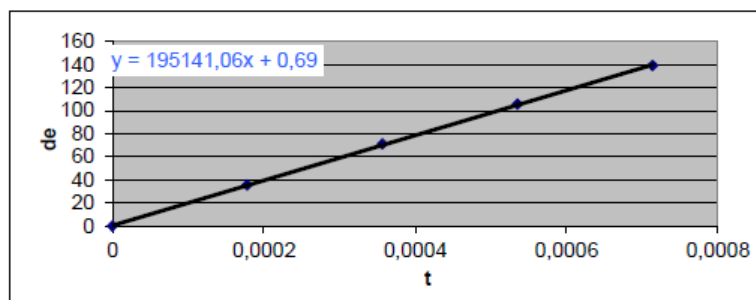


Figure 2-7: Plot of the Euclidean distance of a drop versus time

In literature it's known that measuring the velocity of the smallest drops it is possible to calculate the velocity of the continuous phase. In fig. 2-8 drop velocity is plotted against radial position in the capillary (the origin corresponds to the centerline) at different pressure drops  $\Delta P$ .

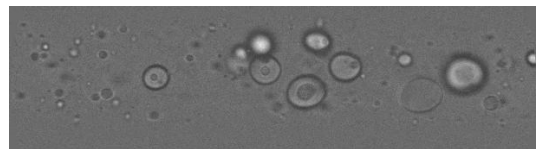
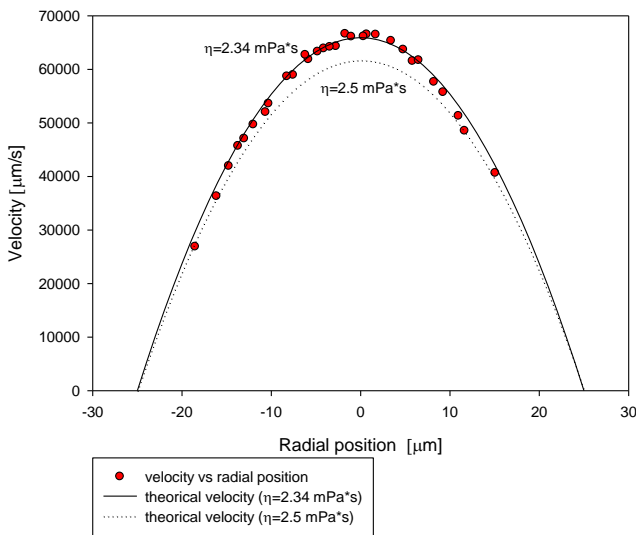
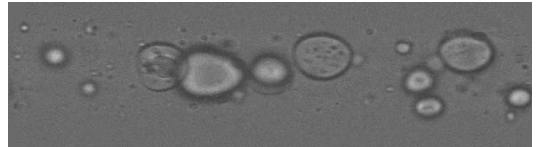
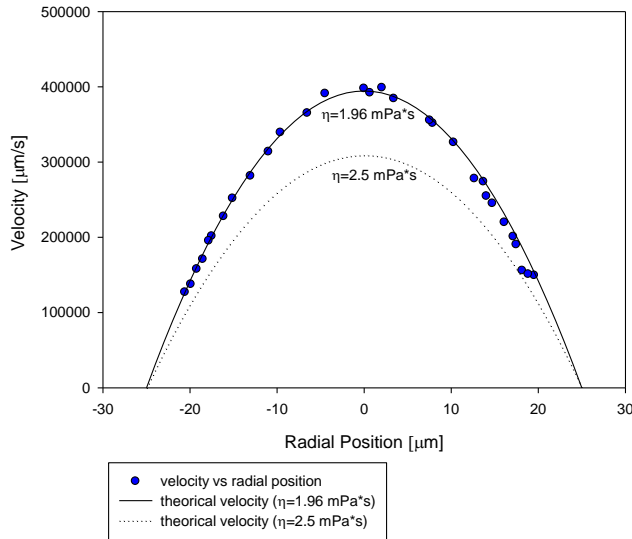


Figure 2-8: Top panel: drop velocity versus radial position and picture at  $\Delta p=205.5 \text{ [cm H}_2\text{O]}$ ; bottom panel: drop velocity versus radial position and picture at  $\Delta p=41 \text{ [cm H}_2\text{O]}$

As shown in the plot, the experimental velocity profile is parabolic, and this trend is in good agreement with Poiseuille's law (valid for laminar regime). By fitting the experimental data with Poiseuille's equation a value of viscosity equal to about 2 mPa·s is calculated, which is comparable to the values obtained by Ubbelohde glass capillary viscometer. In fact, this agreement shows that our flow visualization system could be used like a viscometer.

Our flow cell is a simple laboratory system to visualize the final product's behavior. From an industrial point of view, the emulsion is created by using flow mixers, while the measurement of all the parameters involved, such as conductivity, pH and viscosity is made offline. In this work, in addition to developing the flow cell, we focused on static micromixers. One of the objectives was to gain a fundamental understanding of the fluid dynamics in the micromixers, with a possible application in terms of scale-up that is a key point especially for industrial purposes.

### 2.2.3 Deformability of dispersed phase

The motion of a droplet of radius  $a$  translating with velocity  $U$  in an external immiscible fluid undergoing pressure-driven flow in a cylindrical tube of inner radius  $R$  is schematically represented in Figure 2-9. The average parabolic profile velocity of the external fluid far away from the droplet is  $V$ . The nondimensional parameters governing droplet motion are the ratio  $\lambda$  between the viscosity  $\eta_d$  of the droplet phase and the viscosity  $\eta_c$  of the external phase, the capillary number  $Ca = \eta_c V / \sigma$ , where  $\sigma$  is the interfacial tension, and the ratio  $k$  between droplet and tube radius. The main experimental observables are the nondimensional droplet velocity  $U/V$  and the excess pressure drop  $\Delta P^+$  due to the presence of the droplet made nondimensional with respect to the characteristic pressure  $\eta_c V/R$ . Other quantities which can be experimentally measured are the thickness of the fluid layer separating the droplet surface and the tube wall and the droplet migration velocity in the radial direction. By flow visualization techniques one can also image the external and internal streamline pattern. Most available theories allow one to make predictions of these flow-related quantities to be compared with experiments. This subject has been reviewed by Olbricht (Olbricht et al, 1996).

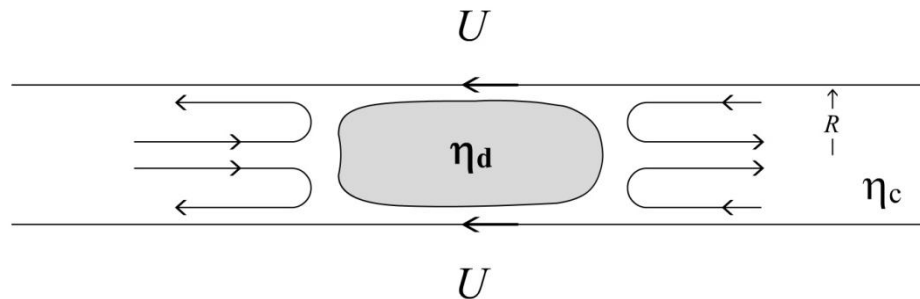


Figure 2-9: Schematic of a droplet translating in an immiscible fluid under the action of confined pressure-driven flow.

Droplet deformation at small values of  $k$  has been the subject of previous reviews. From the theoretical point of view, Hetsroni *et al.* investigated the case of small undeformed droplets ( $k \ll 1$ ) moving along the tube axis, and found the following equation for the nondimensional droplet velocity  $U/V$

$$\frac{U}{V} = 2 - \frac{4\lambda}{3\lambda+2} k^2 + O(k^3) \quad \text{eq. 8}$$

which shows that the droplet velocity lies in between the maximum (centerline) and the average velocity of the undisturbed flow (the maximum velocity being equal to twice the average velocity).

The velocity  $V$  has already been calculated previously and a Matlab macro was written to estimate axisymmetric drops' area by assuming a solid of revolution shape. Then the ratio of  $U/V$  was plotted as a function of  $k$ , the ratio between droplet and tube radius (figure 2-10).

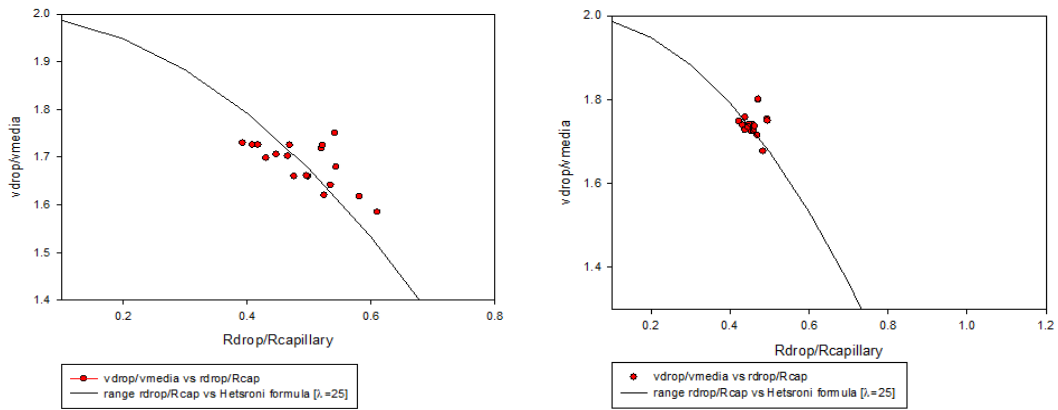


Figure 2-10: Nondimensional droplet velocity versus  $R_{drop}/R_{capillary}$  at  $\Delta p=41 \text{ mmHg}$  (left) and  $\Delta p=205 \text{ mmHg}$  (right)

According to literature the ratio of velocities is a decreasing function of  $k$ , and then the velocity is lower increasing drop's radius. Data fit very well even though they are quite concentrated in a zone and it wasn't possible to reach plateau values.

### 2.3 APPLICATION IN BIOTECHNOLOGY

Fundamental understanding of emulsification process is very important from a biotechnological point of view because it is present in many biological processes. For example the motion of droplets under confined flow has attracted some interest due to the similarities with the shape taken by red blood cells in microcapillaries. The deformability of red blood cells is essential to maintain optimal blood circulation and to allow gas transfer between blood and tissues and just this high deformability allows RBCs to flow even through microcapillaries smaller in size than the cells themselves and can be attributed to several factors, such as cell shape, viscosity of intracellular fluid and rheological properties of cell membrane. Therefore, fluid dynamic behavior of a system constituted by a suspension of liquid drops, that could be considered a developing model of blood flow, is a key study.

Experiments with RBCs, in the same flow cell presented in par 2.1.2, were already carried out; deformability and velocity of erythrocytes were analyzed and very good correlations with literature predictions were found.

Moreover a microfluidic system to measure cell membrane viscoelastic properties in diverging flow has been developed (Fig. 2-11), and the results are in good agreement with data from the literature (Fig. 2-12).

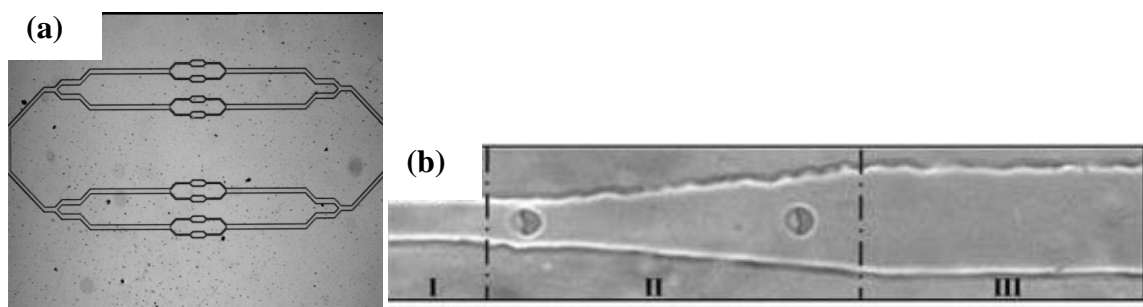


Figure 2-11: a) geometry used in the microfluidic device; b) image of the channel region used to estimate RBC membrane viscoelastic properties

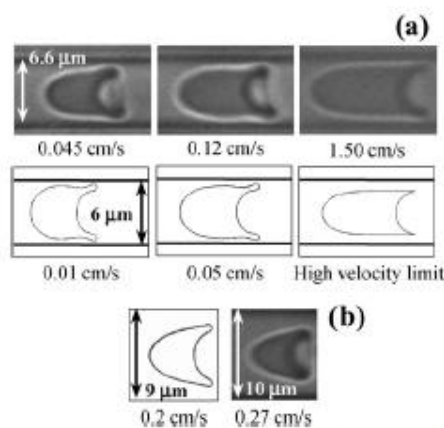


Fig. 2-12: Comparison of the images of flowing RBCs with (a) theoretical predictions and (b) numerical simulations

Microfluidics is a new field dealing with the processing of very small amounts of fluids using channels with micrometric dimensions. Fluid processing in such channels have developed ways for the construction of complexes microstructures, like lab-on-chip, and have opened new and many possibilities for the planning of assays to scale up. These microcomponents allow a set of specific functions, both the simple transport and the dosage of a fluid, and more complex functions like mixing, analysis and synthesis of fluids and blends of fluids. The implementation of the analysis in microfluidics systems is mainly addressed to the application fields: medical-biological and industrial.

Microfabrication uses a variety of pattern techniques, the most powerful of these is photolithography, even though it's not always the best or the only option for all applications. A much cheaper technique is soft-lithography, wherein an elastomeric stamp with patterned relief structures on its surface is used to generate micropatterns and microstructures, like the one showed in Fig. 2-11.

A possible application of this work is in the design of flow devices to measure RBC deformability under conditions mimicking those experienced in vivo. Such devices would indeed allow one to overcome the limits of classical static methods, which are not suitable for handling a large number of cells, and of more empirical techniques, such as blood filtration, which provide data which are difficult to interpret in terms of RBC deformability.

Another possible application of these results is to provide a benchmark of healthy RBC flow behavior to be used as a reference system in the study of pathological conditions where altered cell deformability is advocated, but the understanding of its implications is still elusive due to the lack of adequate experimental methods. Finally the system presented could also be used to evaluate the effects of drugs on cell deformability in microcirculation.

## Chapter 3 PHASE INVERSION EMULSIFICATION

### Introduction

Emulsification processes are traditionally carried out by a direct emulsification method (D), in which the dispersed phase is simply added to the continuous phase under intensive agitation. In the direct emulsification method, the phase in which a surfactant is most soluble is placed in the vessel as the continuous phase followed by addition of the second phase as the dispersed phase. The surfactant used is more soluble in the continuous

phase. As a result, emulsions formed via the direct emulsification method, called normal emulsions, are kinetically stable.

An alternative method is phase inversion emulsification. Phase inversion is a process whereby water-in-oil (W/O) emulsion inverts into oil-in-water (O/W) emulsion and viceversa. There are two types of phase inversion; transitional phase inversion and catastrophic phase inversion (CPI). For transitional phase inversion to happen the affinity of the surfactant(s) must be changed by either changing the temperature or changing the composition of the surfactant mixture at a constant temperature. The affinity of a surfactant toward a phase is conventionally measured by its Hydrophile-Lipophile Balance (HLB). HLB of a surfactant measures the degree to which it is hydrophilic or lipophilic. Altering the HLB results in the surfactant being attracted more towards the oil or water phase depending on the direction of change. Normally a single surfactant will not be of the correct HLB to produce the stability which is desired in the final emulsion. Application of a mixture of surfactants with different HLBs can serve to reduce the interfacial tension and improve emulsion stability, inhibiting the coalescence. Lower interfacial tension means less resistance forces against drop break up and a finer emulsion.

Catastrophic phase inversion emulsification usually starts off with abnormal emulsions. During a CPI process, the instability of an abnormal emulsion continuously increases until it inverts to a normal emulsion of the opposite morphology. This method usually produces finer and more stable emulsions than the direct emulsification method.

Many papers have been published on the influence of various formulations and process parameters on the stability and properties of oil-in-water emulsions containing non-ionic emulsifiers. Gullapalli et al. considered the HLB method as the best tool in choosing the optimal type of emulsifiers for given oil phase and used the HLB system to find the most stable product. Boyd et al., disregarding the resultant HLB value of the emulsifier blend and the required HLB of the oil, considered the improved stability of emulsions containing sorbitan monooleate (Span 80) and ethoxylated sorbitan monopalmitate (Tween 40) to be a result of a convenient meshing of the molecules at the oil droplet-water interface due to steric considerations (figure 3-1).

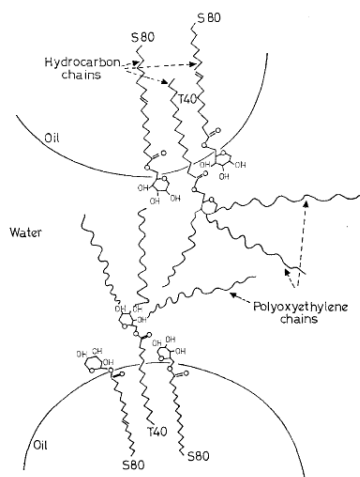


*Figure 3-1 Schematic representation of orientation of Tween and Span molecules in mixed films adsorbed at the oil-water interface*

From a wide research in literature, it has been found that the parameters that mostly influence the stability of emulsions are the ratio of oil concentration to water concentration, the ratio of surfactants' concentration to oil one and HLB.

### 3.1. MATERIALS AND METHODS

The materials used in this study have been already presented in par 2.1.1 and a magnetic agitator with a beaker was used to prepare the samples (Fig.3-2).

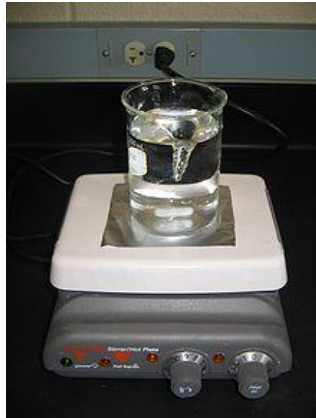


Figure 3-2 Magnetic agitator

Mineral oil was added in a beaker and heated on a magnetic stirrer up to 60°C, and Span20 and Tween 80 were added to oil by gentle mixing for some minutes. Then, when surfactants were completely dissolved, water was added drop by drop. In order to reduce particle size distribution, a mixing at high velocity for 1 min and a cooling at 13°C to inhibit the coalescence were performed.

### 3.2. RESULTS

Further to an experimental campaign (about 40 experiments) a stable emulsion, called sample n°16, was obtained with the following composition:

$$\begin{array}{l} C_{\text{oil}} = 18\% \\ C_{\text{water}} = 76\% \\ C_{\text{Tween80}} = 3\% \\ C_{\text{Span20}} = 3\% \end{array} \quad \longrightarrow \quad \begin{array}{l} \frac{C_{\text{surfactants}}}{C_{\text{oil}}} = 0.33 \\ \frac{C_{\text{oil}}}{C_{\text{water}}} = 0.24 \\ \text{HLB} = 11.8 \end{array}$$

In figure 3-3 a picture of the stable emulsion is shown:



Figure 3-3 Stable emulsion

### 3.2.1 Particle size distribution and stability

Particle size distributions of emulsions were determined by the centrifugal sedimentation method using a HORIBA particle size analyzer (HORIBA Instruments, Inc). The instrument is based on the principle of liquid phase sedimentation with measurements being done using an optical transmission method. In this method, the Stokes' sedimentation equation is combined with the proportional relationship between the absorbency and particle concentration. Approximately five drops of emulsion were diluted with approximately 30 ml of distilled water. Particle size was measured immediately after dilution and 1 minute to evaluate stability.

In Figure 3-4 an image of the most stable sample (n°16) and the plot of the particle volume distribution where the cumulative volumetric function,  $q$  [%] is a function of drop diameter [ $\mu\text{m}$ ] is reported. The distribution is unimodal and the mean diameter is about 0.17 micron, as confirmed in the picture, where a very small and quite homogeneous diameter distribution is shown.

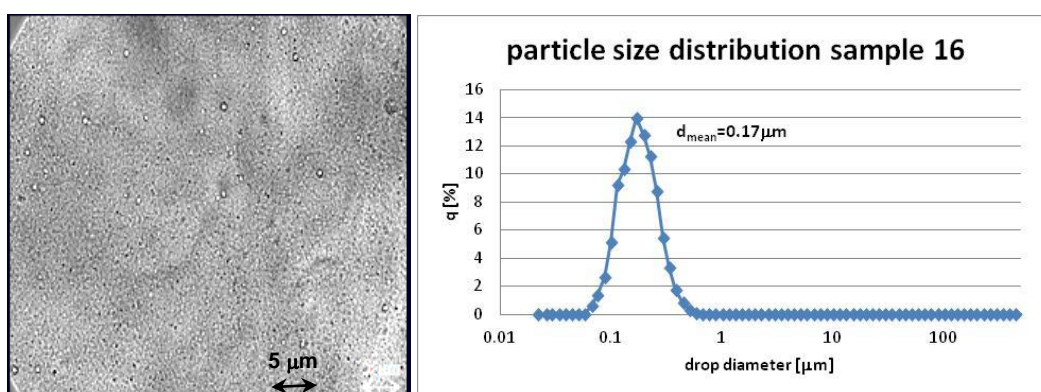


Figure 3-4 Static image and particle size distribution

In order to compare the stability of sample n°16 and other quite stable samples, obtained by changing the parameters previously presented and showed in table 3-1, particle size distribution with the Horiba instrument and stability measurements with a temperature controlled separation analyzer (Lumifuge) were performed (Fig. 3-5 and 3-6).

Sample n°	$C_{oil}/C_{water}$	$C_{surf\_TOT}/C_{oil}$	HLB
11	0.18	0.25	10.00
12	0.24	0.33	12.86
15	0.24	0.33	12.86
16	0.24	0.33	11.80
19	0.24	0.33	12.86

Table 3-1 Samples n°11, 12, 15, 16 and 19

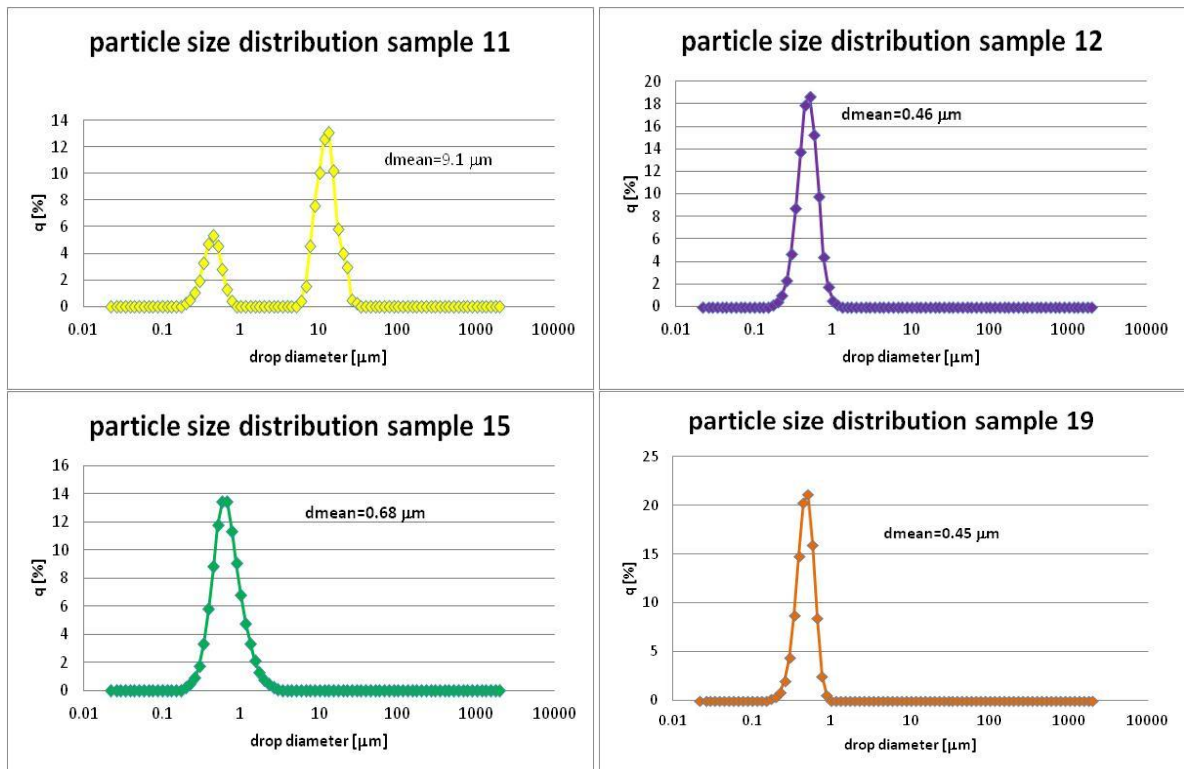


Figure 3-5 Particle size distribution of samples 11, 12, 15 and 19

Particle size distribution of sample 12, 15 and 19 are quite similar, while PSD of sample 11 is completely different ( $d_{\text{mean}}=9.1\ \mu\text{m}$ ), as its HLB, that is more lipophilic.

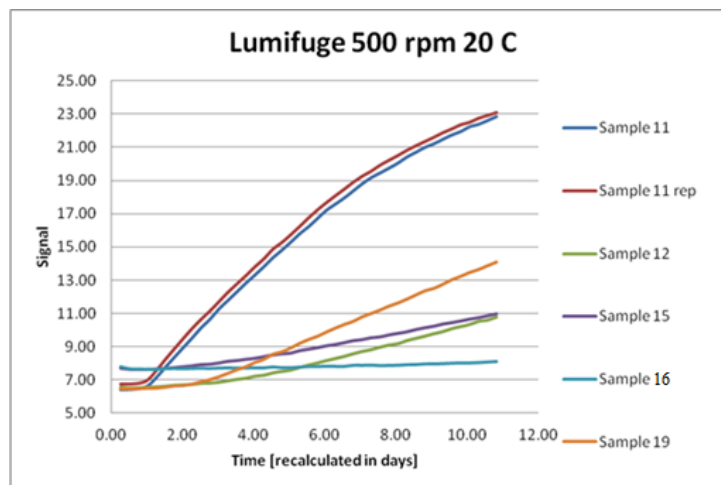


Figure 3-6 Lumifuge measurements

The LUMiFuge stability analyser is an analytical centrifugation system that measures the intensity of transmitted light in a sample being centrifuged. During the measurement, light illuminates the entire sample cell and the transmitted light through the sample is then detected. Regions of high particle concentration exhibit a low transmission value and regions of low particle concentration exhibit a high transmission value. In figure 3-6 light signal as a function of time for different samples is reported and the flatter the curves are, the more stable the sample is, therefore sample 16 is the most stable, while sample 11 is the less stable, as confirmed by the bimodal particle size distribution.

This emulsion is quite different from the one presented in Figure 2-5, even though the materials used are the same. In order to study the kinetic of formation of this emulsion

stable for more than one year, an analysis of the product by adding very small quantities of water has been performed and very peculiar behaviour has been found. In fig. 3-6 pictures at different water concentration are shown and at about 27% water a Weissenberg effect-like has been found.

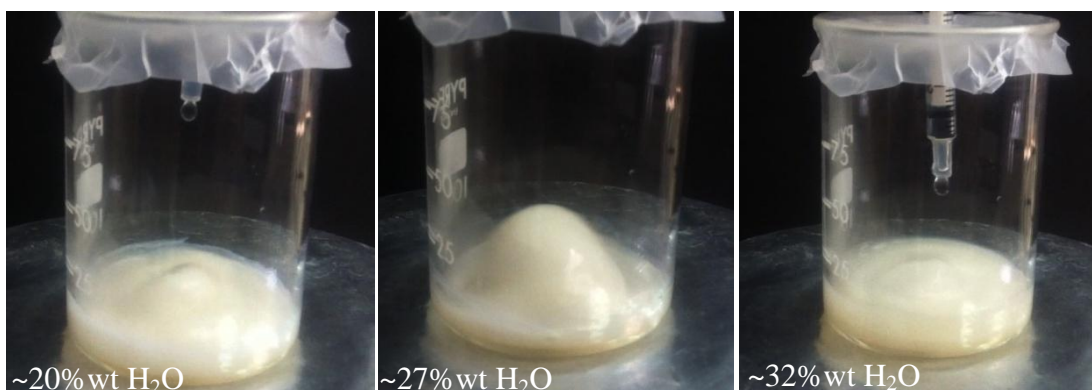


Figure 3-6 Emulsion at different water concentration

### 3.2.2 Electrical Conductivity measurements

The formation of emulsion by phase inversion can be monitored by electrical conductivity (EC) that is measure of a material's ability to conduct an electric current. EC measurements were performed at 25°C with a conductivity meter, (Bormac-PC 2700) on samples at different water concentrations (Fig. 3-7).

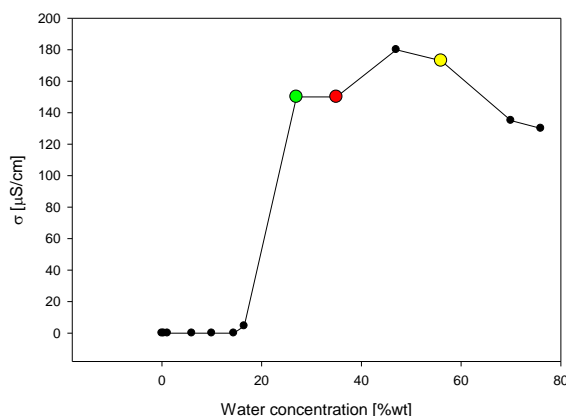


Figure 3-7 Variation of the electrical conductivity as a function of water concentration

Electrical conductivity can provide a good indication of microstructure transitions occurring in emulsion, i.e. transformation from water-entrapped systems to intermediate structures and further to water continuous microstructure. When the continuous phase is aqueous, it exhibits higher conductance than the oil-continuous formulation. The conductivity increases exponentially as the water content increases. The profile shows that up to 20 wt% of water, conductivity is initially low, suggesting the existence of reverse structures in a nonconducting oil medium, which have little interaction with each other. When more than 20 wt% of water is added, the conductive droplets begin to contact each other and form other structures, giving rise to the observed changes in properties, such as an increase in electrical conductivity.

### 3.2.3 Rheological measurements

Viscosity measurements at 27 wt% of water (Weissenberg effect) and 76 wt% (final concentration of water) at 25°C, with an Anton Paar rheometer (Rheoplus/32 Multi3 V2.81) were performed. A cone-plate geometry (CP75) has been used.

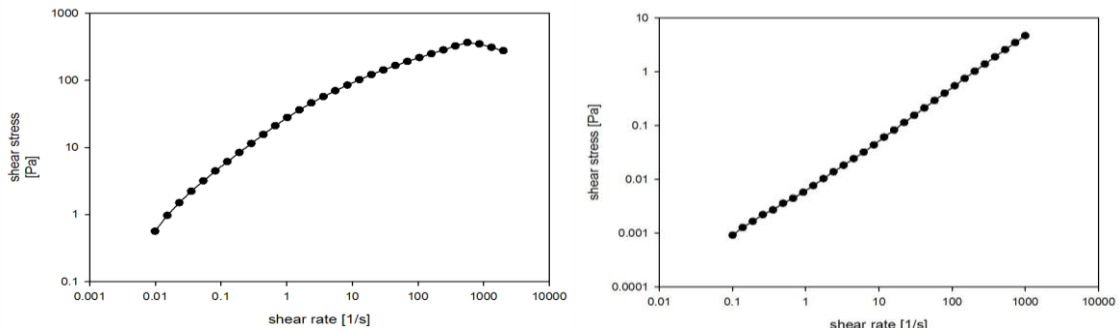


Figure 3-8: Flow curves at Weissenberg effect and of final emulsion

In figure 3-8 flow curves in terms of shear stress as a function of shear rate were performed and in the first graph (left side) a pseudoplastic behaviour, with a net curvature, is shown, while the complete emulsion shows a Newtonian behaviour.

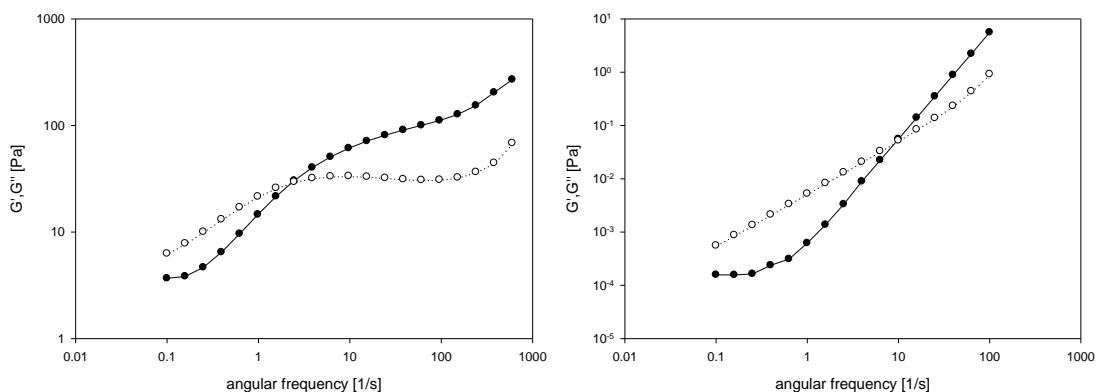


Figure 3-9: Oscillatory measurements at Weissenberg effect and of complete emulsion

Oscillatory measurements at Weissenberg effect and for the complete emulsion at 25°C with the same rheometer were performed and showed in figure 3-9, where for both samples at low frequencies a liquid-like behaviour is showed, but the point of crossover for the first sample occurs before showing a more elastic behaviour at Weissenberg effect, as expected. A different method for oscillatory measurements was used: a first step by imposing a rotation of the cone at shear rates=1 and 10 1/s, immediately followed by an oscillation for  $0.1 < \omega < 200$  to measure the fluid behaviour just when Weissenberg effect occurs (Figure 3-10). In this case a completely different measure has been found, showing the gel-like behaviour of the sample being G' and G'' parallel each other.

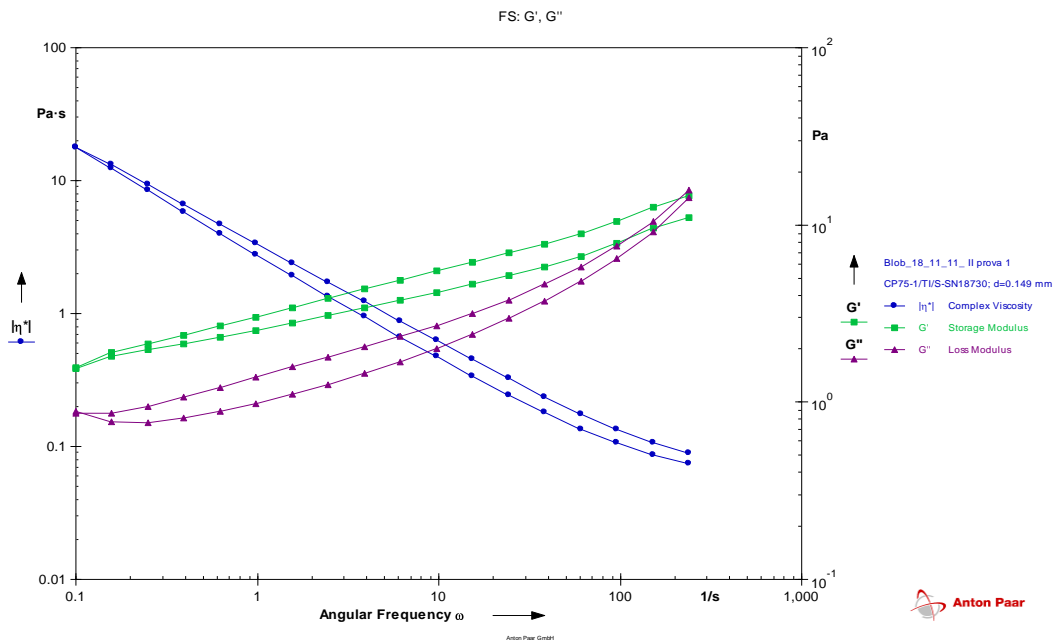


Figure 3-10: Oscillatory measurements at Weissenberg effect

### 3.2.4 Morphology by CSLM

In order to observe the formation of a stable emulsion by phase inversion a confocal scanning laser microscope (CSLM-Axiovert 200M) and Rhodamine B in water phase as fluorescent dye, were used.

In figure 3-11 subsequent pictures at increasing water concentration are showed: the first one (on the left) is completely dark because there was no water with Rhodamine B, and then some structures appear also at very low concentration of water until the formation of water in oil drops in water phase, that is completely red.

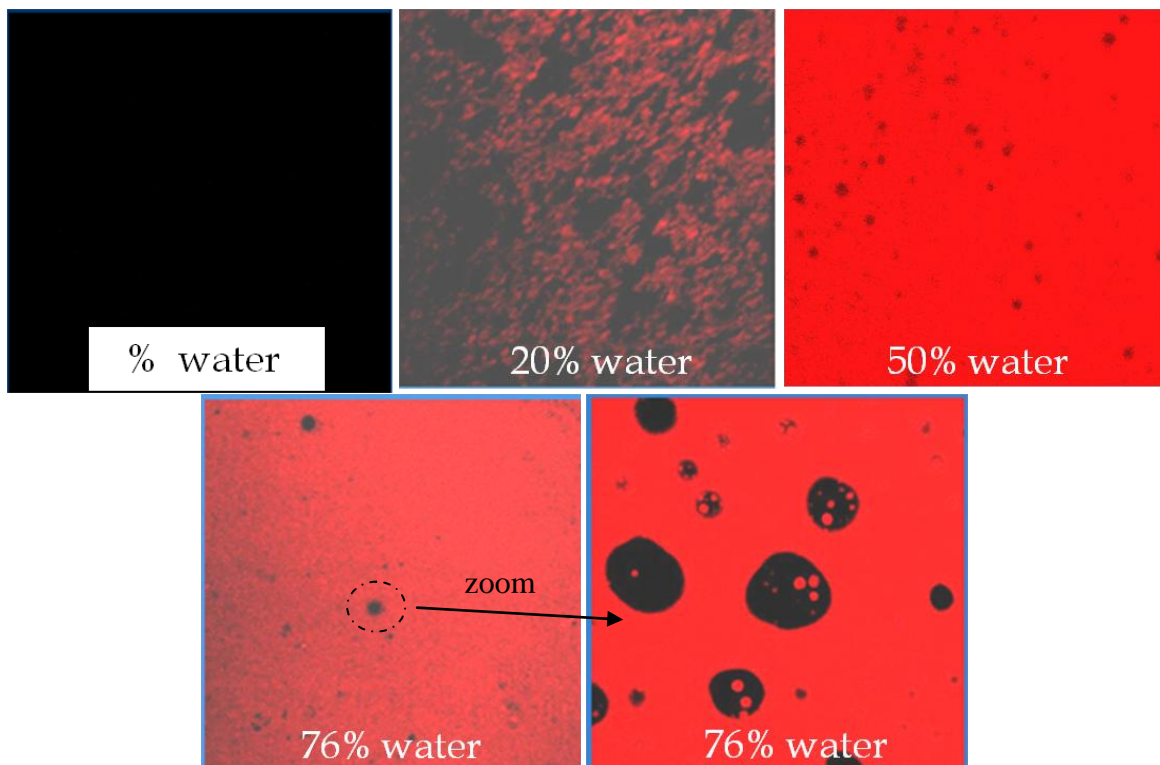


Figure 3-11 Subsequent sampling of emulsion by adding water

In order to visualize the different contributions of water and oil in a very complex structure, two fluorescent dyes, Fitc-dextran, that behaves like Rhodamine B, linking to water phase and Nile red, that is a lipophilic stain, were used. In figure 3-12 a picture at very low water concentrations (0.37%) is shown.

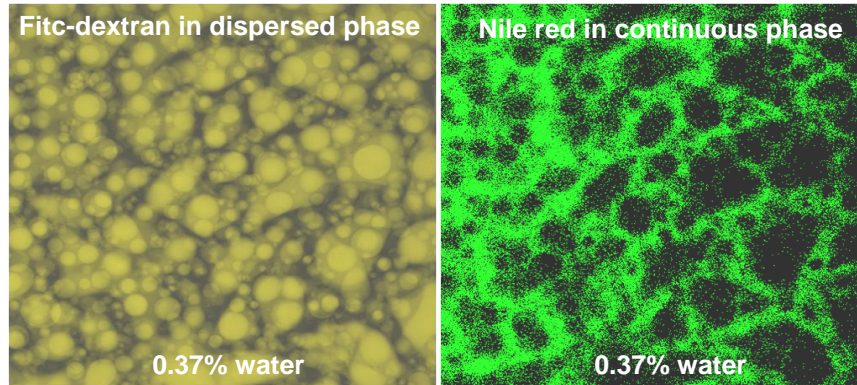
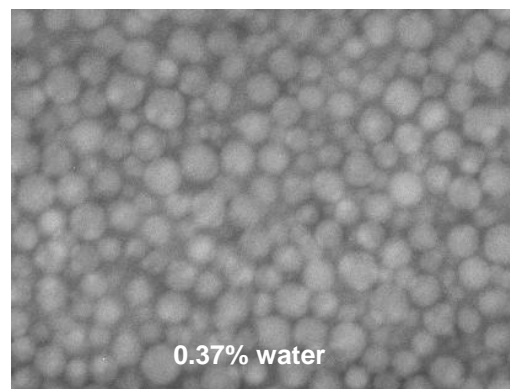


Figure 3-12 Emulsion at 0.37% water concentration with two fluorescent dyes

### **3.2.5 Interfacial tension measurements**

The interfacial tension between the two phases, at 0.37% of water, was measured by analyzing drop retraction, after coalescence of two smaller drops, as reported by Guido and Villone. The movie was acquired with a confocal scanning laser microscopy in epifluorescence set-up, equipped with a videocamera, and Rhodamine B was added to the water phase as a fluorescent dye. The drop relaxation after the coalescence is showed in figure 3-13. The analysis was based on the time evolution of the parameter  $D'$ , defined as  $D' = (R_p - R_z)/(R_p + R_z)$ , where  $R_p$  and  $R_z$  are the major and minor axis of the projection of the drop on the vorticity – flow direction plane. The following simple analytical expression for the evolution of  $D$  with time during retraction was used:

$$D = D_0 \exp\left(-\frac{40(\lambda+1)}{(2\lambda+3)(19\lambda+16)}\tau\right) \quad \text{eq 3.1}$$



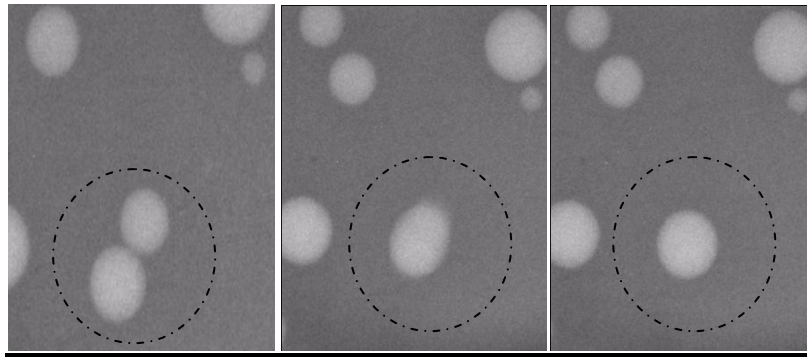


Figure 3-13 Emulsion at 0.37% water concentration (top panel), zoom of the previous picture where retraction is shown (bottom panel)

The logarithm of  $D/D_0$ , where  $D_0$  is the value of  $D$  at the beginning of the retraction, as a function of time is plotted and the result in figure 3-12, where a value of  $\sigma=9.6 \cdot 10^{-4}$  mN/m is found. This value is quite low but in agreement with previous results from literature when two surfactants are used.

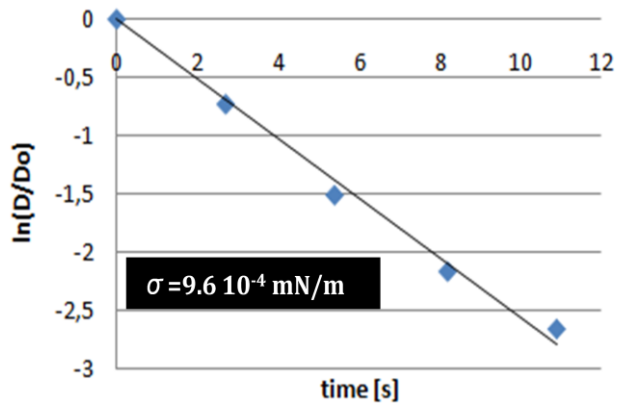


Figure 3-12  $\ln(D/D_0)$  versus time in seconds

## Chapter 4 MIXING OF LIQUID-LIQUID NON-NEWTONIAN FLUIDS

### Introduction

Liquid-liquid mixing is a common industrial practice, widely used in a variety of application, ranging from polymer synthesis and processing to biotechnology. Despite the extensive literature available on the topic, liquid-liquid mixing is still one of the most difficult and least understood mixing problems. Different technical solutions are available for the liquid-liquid mixing, depending on the type of processed fluids, ranging from the mechanical agitators to the in-line static mixers. Static mixers consist of a series of motionless inserts installed in pipes or transfer tubes. Their purpose is to divide and redistribute the fluid streams sequentially until good mixing has been achieved. Indeed, they offer narrower residence time distribution, lower capital and operating costs and minimal maintenance requirements. In these devices, the energy of mixing is derived from the extra pressure loss needed to pump the fluids through the mixing elements, with respect to that needed if the fluid were flowing in the same tube, in absence of mixing elements. Various techniques

have been used in the examination of static mixer performance: cross-section of mixtures of materials of two colors have been examined, conductivity profiles for the mixing of two streams identical except for conductivity have been determined, fast competing reactions have been used to compare laminar flow micro-mixing in empty tubes and static mixers. However, although predictive methods for mixture quality are often claimed, the basic understanding that governs static mixer performance is still quite limited. Most of the fluids used in the industries show non-Newtonian behavior, it is well known that the viscoelasticity of one of the phases can prevent the break-up of a single drop in a controlled flow, but very few is known about the mixing of non-diluted emulsion, when of one or both the liquid phases show non-Newtonian behavior. A comprehensive characterization of liquid-liquid mixing in these systems is still missing and their application is based more on intuition and vendors claims than on scientific data.

In this work we investigated the influence of the viscoelasticity of one of the phases on the mixing efficiency both using mechanical agitators and Kenics static mixers. Low viscosity water based Boger fluid has been ad hoc formulated in order to limit the pressure loss, the oil phase was chosen as Newtonian silicon oil. In order to stabilize the processed emulsion surfactants were added to the oil phase. Some preliminary results on the mixing efficiency and emulsion stability are here reported both for of water in oil and oil in water cases.

## **4.1. MATERIALS AND METHODS**

### **4.1.1 Materials**

Low viscosity Boger fluids were used as aqueous phase, the fluid consist of dilute concentrations of high molecular weight polymer in a Newtonian solvent, made of 76 wt% glycerin-water. Two different fluids have been formulated using polyacrylamide Separan (PAA) (supplied by Dow Chemical Ltd) and xanthan gum Keltrol (XGh) (supplied by Kelco) as high molecular weight polymer. The viscosity of the phases was kept low in order to reduce the pressure loss during the processing.

The polymer solutions were prepared by first dissolving the appropriate amount of polymer into deionized water to make a stock solution with a polymer concentration of 0.1 wt%. The water was warmed to about 40°C and the polymer was added gradually to the water while continually swirling the container in order to disperse the polymer and avoid agglomeration. Sodium azide was added to the stock solution (< 0.02 wt %) to prevent bacterial contamination. The stock solutions were placed in a beaker with a magnetic stirrer at very low rotation rates for about 48 h and, once the polymer was fully dissolved, the solutions were stored in the refrigerator. The experimental solutions were made by adding the appropriate amounts of polymer stock solution to the required glycerol and sodium azide in order to obtain the desired final polymer concentration, the balance was made up with deionized water.

The fluids selected as non-newtonian phase for the mixing experiments were at 75 ppm both for the PAA and XGh fluid. As oil phase, Newtonian silicon oils (SO) of different molecular weight (Dow Corning 20cst, 1000cst and 6000cst) were used. In this work oil in water and water in oil mixtures at 10 and 90 % of oil phase have been mixed, we will here present only results relative to the oil matrix case.

#### **4.1.2 Static mixers and experimental apparatus**

In order to verify fluids immiscibility and to evaluate phase separation times, preliminary experiments were performed in mechanical agitators, using a beaker stirred by a rotating magnetic bar, kept at constant velocity and controlled temperature.

More controlled flow conditions were realized using Kenics plastic static mixers, placed in PVC tubes connected to two volumetric pumps (Harvard Apparatus) used for inlets injection by two stainless steel syringes, the dispersed phase was injected coaxially. Experiments reported were performed with 49 elements of Kenics mixers in a 3/16" inner diameter tube at about 26 ml/min, at room temperature (23°C).

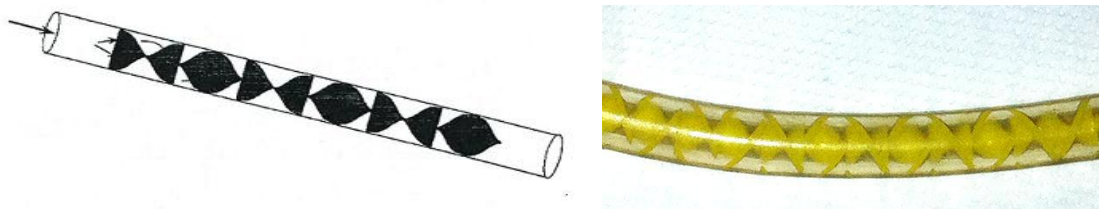


*Figure 4-1: Kenics static mixers in a tube*

To evaluate the mixing efficiency, the droplet size distribution was measured observing the sample at the microscope. A few ml of mixture were sampled at the end of the mixing line, and placed between two microscope slides. The samples were optically scanned by using a motorized inverted microscope equipped with high resolution camera and then droplet size distribution was measured by means of automated software. By means of a microscope incubator it is possible to observe the same sample portion, kept at constant temperature, over time (Time Lapse). In this way it was possible to investigate the emulsion stability over time, at different temperatures.



*Figure 4-2: Microscope incubator*

## 4.2 RESULTS

### 4.2.1 Rheological measurements

Rheological measurements were carried out using a stress controlled rheometer (Bohlin, CVO 120), due to the low viscosity and weak elasticity of the fluids; the rheometer sensibility was enhanced by using a double gap rotational geometry. In Figure 4-3 the viscosity is reported as function of shear rate for samples at different polymer concentration for Polyacrylamide (left) and Xantan gum (right),  $T = 20^\circ\text{C}$ . Polyacrylamide fluid exhibits constant viscosity for all shear rates considered, while Xantan gum based fluids show a slight shear thinning for low shear rates (about  $1 \text{ s}^{-1}$ ).

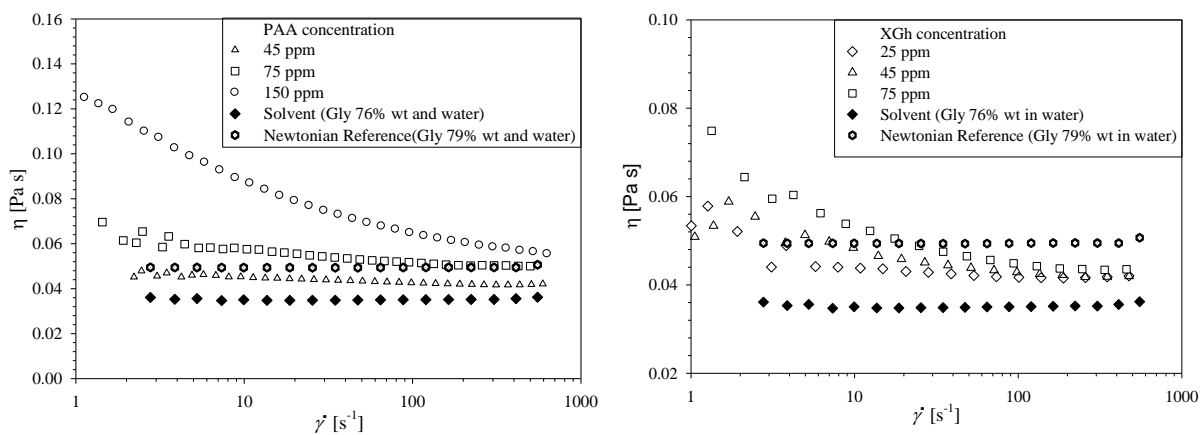


Figure 4-3: Viscosity versus shear rate at different polymer concentrations,  $T = 20^\circ\text{C}$ . Left: Polyacrylamide, Right: Xantan Gum.

In order to quantify the first normal stress difference ( $N_1$ ), the first normal stress coefficient was estimated from dynamic measurements according to eq 4-1.

$$\Psi_1 = \frac{N_1}{\dot{\gamma}^2} = \lim_{\dot{\gamma} \rightarrow 0} \frac{N_1(\dot{\gamma})}{\dot{\gamma}^2} = 2 \lim_{\omega \rightarrow 0} \frac{G'(\omega)}{\omega^2} \sim 2 G' \quad \text{eq.4-1}$$

In Figure 4-4 the elastic modulus ( $G'$ ) is reported as a function of the frequency for both PAA (left) and XG (right) at different solution. As first approximation  $N_1$  can be estimated assuming  $\omega = \dot{\gamma} = 1$  and assuming the fluid as a second order one.

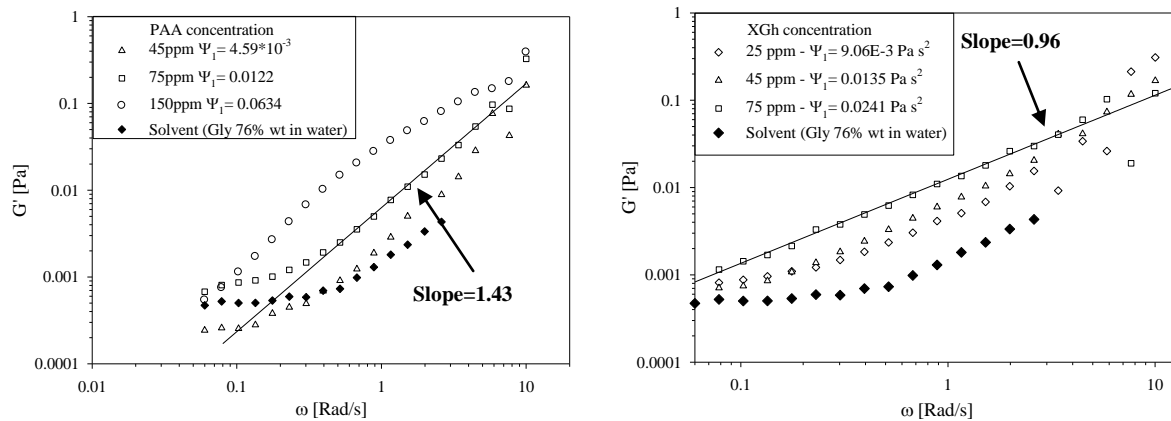


Figure 4-4: Storage modulus as function of oscillation frequency for different polymer concentration,  $T=20^\circ\text{C}$ . Left: Polyacrylamide, Right: Xantan Gum.

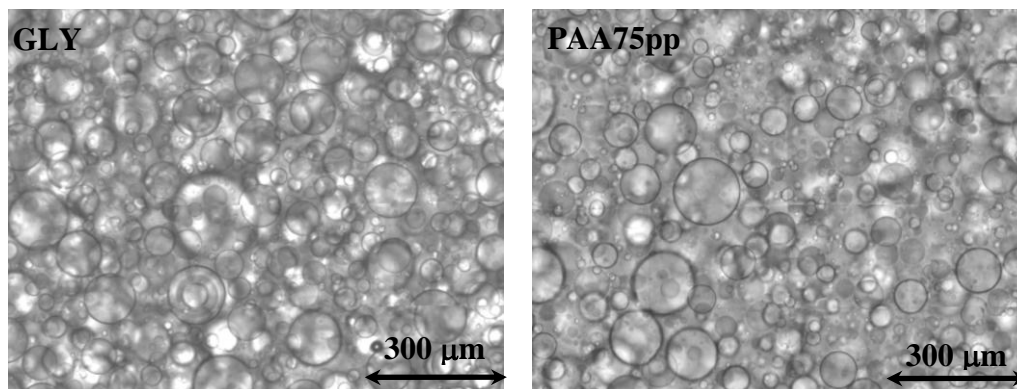
In order to quantify the influence of viscoelasticity on the mixing efficiency, a reference Newtonian fluid (GLY), obtained by mixing water and glycerin in an appropriate concentration (79.7%<sub>w/wt</sub>) to obtain the same viscosity of the non-Newtonian reference has been used.

#### 4.2.2 Characterization

It's known from the literature that higher viscoelastic effects are expected when the viscoelastic phase is the continuous one, so we firstly chose to use water phase (Boger fluids or Newtonian GLY) as matrix and 20cSt silicon oil as drop phase. Due to the low viscosity of the matrix phase, a fast coalescence phenomenon was observed, resulting in fast morphological changes over time. To suppress coalescence phenomena, a non ionic surfactant, Span20 was added.

To further increase sample stability we used the 6000 cSt oil as matrix phase, and water based Newtonian/Boger fluid as drop phase. In the following we report only some preliminary results obtained for the case of water in oil emulsion, mixed with Kenics static mixers. To investigate the influence of the viscoelasticity of the drop phase three different disperse phases have been used: Newtonian GLY, PAA 75 ppm and XGh 75 ppm, the continuous phase was always the Newtonian Silicon Oil 6000 cst.

In figure 4-5 a mosaic of 16 images for the three emulsions is compared; Newtonian GLY, PAA75 and XGh75 are the top, middle and bottom image respectively.



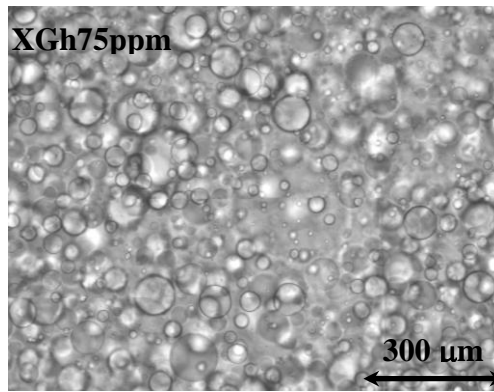


Figure 4-5: Images of emulsion obtained with Kenics static mixers. Continuous phase is SO 6000 cst, disperse phase is Newtonian GLY (top), PAA 75ppm (middle), Xantan gum 75ppm (bottom).

### 4.2.3 Interfacial tension measurements

The interfacial tensions  $\sigma$  of the mixtures used were measured observing the deformation of a single drop of water based phase in a matrix of SO6000, under simple shear flow at constant shear rate ( $\dot{\gamma}$ ). The flow is realized by means of a parallel plate rheo-optical apparatus (figure 4-6).

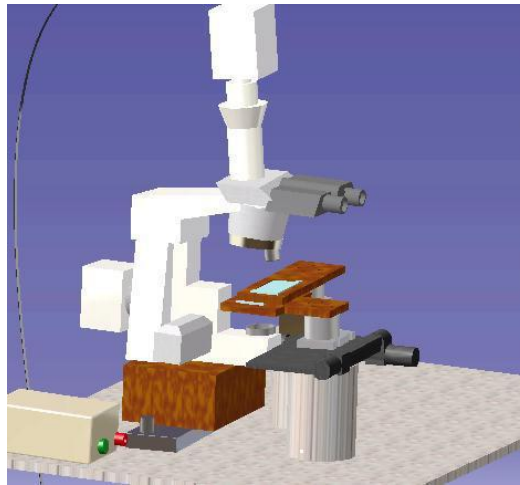


Figure 4-6: Microscope with parallel plates apparatus

Images of deformed droplets, observed along the vorticity axis, are acquired by a high speed camera (Phantom 640) equipped on an optical microscope (Zeiss AxioScope). For each system the drop deformation fit according to the Shapira-Haber theory model to confined systems. (Eq. 4-2) relates the steady state deformation parameter  $D(R_p - R_z)/(R_p + R_z)$ , where  $R_p$  and  $R_z$  are respectively the major and minor axis of the ellipsoidal shape of the deformed droplet, to the capillary number  $Ca = \frac{\eta_m \dot{\gamma} R}{\sigma}$ , the ratio  $\lambda = \frac{\eta_d}{\eta_m}$  of the droplet vs matrix viscosity;  $C_s$  is a geometrical parameter,  $R$  the droplet undeformed ratio,  $d$  is the gap between the plates.

$$D = \left[ 1 + C_s \frac{1+2.5\lambda}{1+\lambda} \left( \frac{R}{d} \right)^3 \right] \frac{19\lambda+16}{16\lambda+16} Ca \quad \text{eq 4-2}$$

In Figure 4-7 the experimental values are compared to Shapira-Haber prediction and to the Taylor unconfined equation.

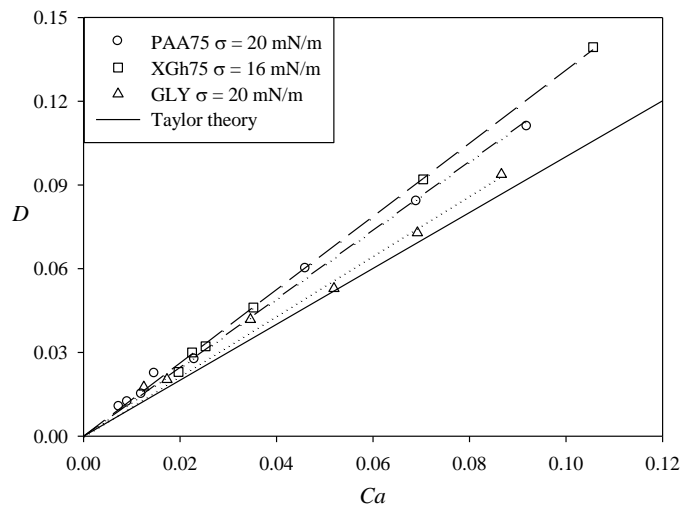


Figure 4-7: Deformation parameter  $D$  vs  $Ca$  for the three systems. Continuous line is the Taylor unconfined prediction, dashed, dash-dot and dotted lines are the Shapira-Haber theory for each system.

It's worth mentioning that the fluids selected are expected to show significant differences in terms of deformation and break-up of single drop in simple shear flow.

### 4.2.3 Image analysis

After a qualitative comparison of the images in figure 4-5, the tree samples appear similar. In figure 4-8 we report the drop size distributions for a quantitative comparison. The numerical distribution, and the numerical cumulative (figure 4-8, a and b respectively) show only minimal differences, in particular XGh 75 and GLY appear to be almost superimposed, while the PAA 75 appeared slightly better mixed. The cumulative volumetric reported in figure 4-8-c enhances the differences in the distributions at the higher diameters, this test is focused to investigate what is the size of the drop corresponding to most of the volume of the dispersed phase added to the mixture. The large diameters tail of the distribution show better mixing for the XGh 75.

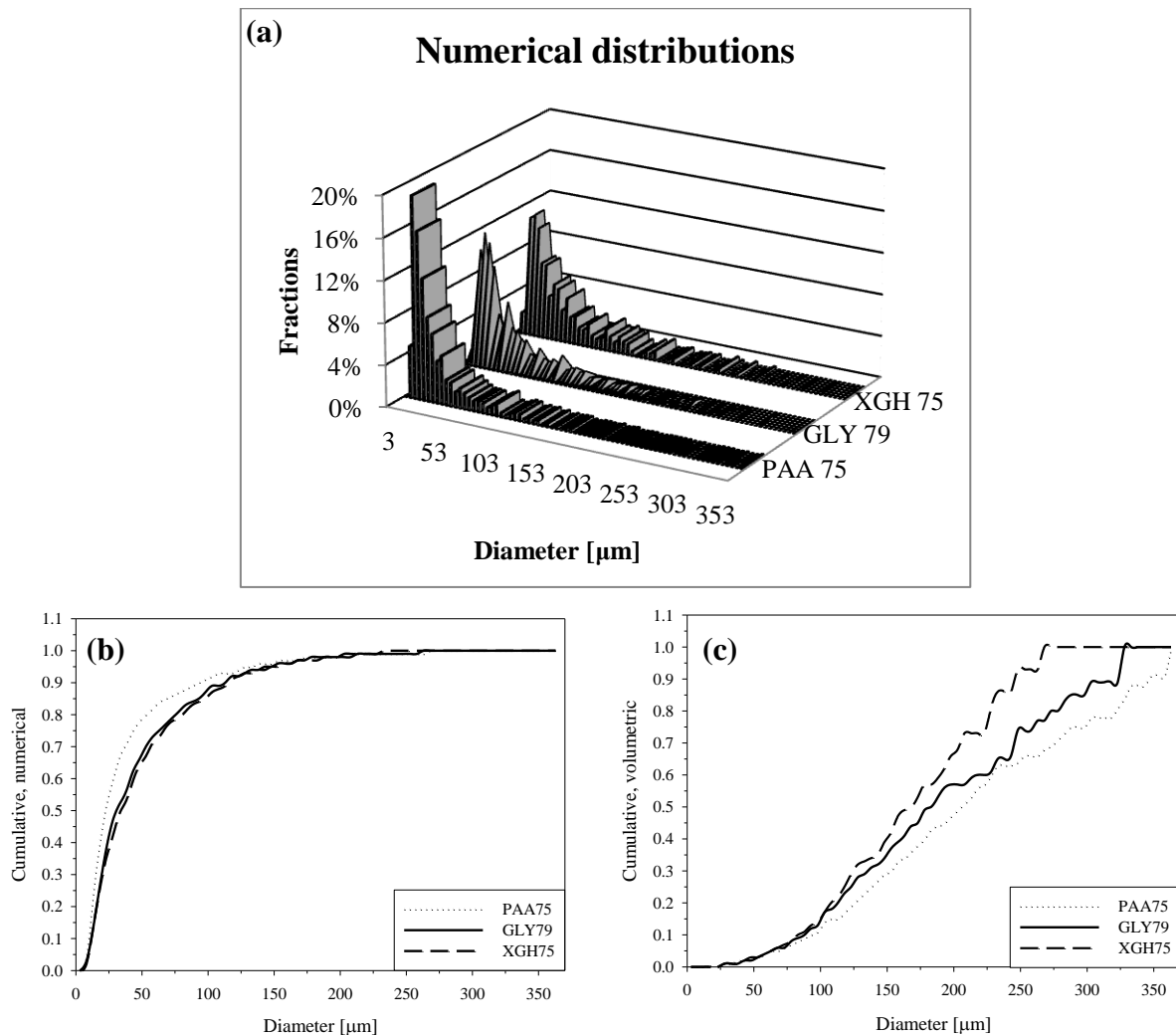


Figure 4-8: Particle size distribution for Newtonian and non-Newtonian fluids. A) numerical distribution, B) numeric cumulative, C) volumetric cumulative.

In Table 4-1 different average diameters in microns, for the three samples, are reported. As expected from previous observations, most of the values are within the error bar for the three different samples, the only significant difference being for volume averaged diameter D43, and representative of the higher diameter tail of the distribution. As observed in the charts, XGH75 shows a higher mixing efficiency.

	D10	D32	D30	D43
GLY79	49±2	147±10	88±1	<b>190±16</b>
PAA75	38±7	156±6	81±6	208±15
XGH75	51±5	134±4	86±5	<b>164±0.1</b>

Table 4-1: Measured average diameters for mixtures with Newtonian and non-Newtonian disperse phase, values are in  $\mu\text{m}$ .

The expected influence of the elasticity was to delay break-up phenomena, so resulting in a lower mixing efficiency. The effect was expected to be limited in the case the elasticity was only in the drop phase, compared to the case of elastic matrix. In our case PAA75

shows substantially the same mixing efficiency compared to the Newtonian GLY, while XGg75 showed partial improvement in the mixing efficiency in the large diameter tail of the distribution. The higher mixing of the XGh75 could be due to the lower value of the interfacial tension, as reported in figure 4-7. This is not unexpected since XGh is often used as emulsifying agent.

It is worth mentioning that coalescence wasn't completely excluded both during the mixing flow and during the sampling process and it could partially affect the results.

The conclusion is that the differences induced by the viscoelasticity of the dispersed phase, in the range of values here investigated, are only limited and partially covered by the error induced by the presence of coalescence phenomena, partially by differences in the interfacial tension.

In order to further suppress coalescence phenomena, 0.5% wt Span20, a non-ionic surfactant, was added to the silicon oil phase (figure 4-9) and mixing was performed with the Kenics apparatus. Comparing Figure 4-9 with the images in Figure 4-5 it is evident a strong influence of the surfactant in the mixing phenomena. The average drop size obtained in the presence of a limited quantity of Span 20 is certainly lower.

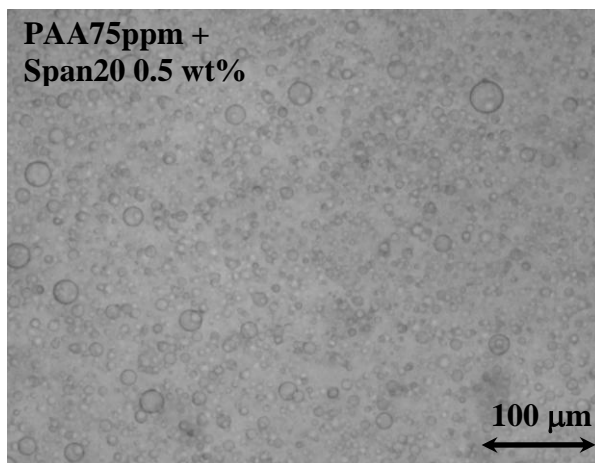


Figure 4-9: Images of emulsion obtained with Kenics static mixers. Continuous phase is SO 6000 cSt + 0.5 % wt Span21, disperse phase is PAA 75ppm.

In conclusion we presented here a methodology to investigate the influence of the viscoelasticity of one of the phases on the mixing phenomena. Some preliminary results show limited influence of the viscoelasticity of the dispersed phase, while a strong effect of the interfacial tension was observed. In particular even small quantities of surfactants can lead significant differences in the mixing efficiency. This particular aspect will be widely investigated in the future.

The presence of fast coalescence phenomena did not allowed a detailed investigation in the case of viscoelastic matrix, due to the limited viscosity of the phase. Further investigation will be done, formulating a Boger fluid with a viscosity high enough to reduce the effect of the coalescence, but not as high as to make the pressure loss in the mixing apparatus unaffordable.

## CONCLUSIONS

The objective of this PhD thesis was to study emulsification process to form products stable over time and to use these products as blood analog mimicking the rheological and fluid dynamic behavior of blood.

Different systems were examined and different kinds of experiments were performed, and the main conclusions from each experiment are presented in the following.

1. An experimental methodology to investigate the deformability of emulsions flowing in microcapillaries placed in a flow cell, where the sample was fed under the action of a liquid head in the physiological range. Video microscopy images of the flowing drops in a continuous phase are acquired at high magnification and later processed by an automated image analysis macro. It was found that the experimental velocity profile in a 50 $\mu\text{m}$  capillary is parabolic, and this trend is in good agreement with Poiseuille's law, and that axisymmetric small droplets moving along the tube axis follow Hetsroni equation, which shows that the droplet velocity lies in between the maximum (centerline) and the average velocity of the undisturbed flow (the maximum velocity being equal to twice the average velocity).
2. A methodology to study the formation of emulsions stable over time by phase inversion. After a wide research in literature and experimental validations, the parameters involved in emulsions' stability was found to be the ratio of surfactants concentration to oil concentration, the ratio of oil concentration to water one and the HLB, expressed as the affinity of a surfactant toward a phase. An emulsion stable for more than one year was prepared and investigations of product's morphology during phase inversion emulsification were performed.
3. A methodology to investigate the influence of the viscoelasticity of one of the phases on the mixing phenomena. Some preliminary results show limited influence of the viscoelasticity of the dispersed phase, while a strong effect of the interfacial tension was observed. In particular even small quantities of surfactants can lead significant differences in the mixing efficiency.
4. An optimization of microsplit and recombine mixers for emulsification, and more in general for mixing process. An experimental campaign to study the effects of several factors, such as the rate of energy dissipation, the viscosity of the oil and water phases, the oil volume fraction, the flow rate and the temperature on the mixing efficiency. Further conclusions in the confidential allegato were presented.

## BIBLIOGRAPHY

- 1) M. Abkarian, M. Faivre and H.A. Stone, "High-speed microfluidic differential manometer for cellular-scale hydrodynamics", *PNAS*, **103**: 538-542, (2006)
- 2) C. Boyd, Parkinson, P. Sherman, "Factors affecting emulsion stability, and the HLB concept", *J. Colloid Interface Sci.* **41**: 359-370, (1972)
- 3) Borhan, J. Pallinti "Pressure-Driven Motion of Drops and Bubbles through Cylindrical Capillaries: Effect of Buoyancy", *Ind Eng Chem Res* **37**: 3748-3759, (1989)
- 4) H. Brenner, PM. Bungay "Rigid-particle and liquid-droplet models of red cell motion in capillary tubes". *Fed Proc*, **30**: 1565-1577, (1989)
- 5) Leal-Calderon, F., F. Thivilliers and V. Schmitt, "Structured emulsions" *Curr. Opin. Colloid In. Sci.*, **12**: 206-212, (2007).
- 6) S. Caserta, S., Reynaud, S., Simeone, M. and Guido, S. "Drop deformation in sheared polymer blends", *Journal of Rheology*, **51**: 761-774 (2007).
- 7) S. Caserta, M. Simeone, S. Guido, "Evolution of drop size distribution of polymer blends under shear flow by optical sectioning", *Rheologica Acta*, **43**: 491-501 (2004).
- 8) V. Cristini, G. Kassab "Computer modeling of red blood cell rheology in the microcirculation: a brief overview". *Ann Biomed Eng* **33**: 1724-172 (2005)
- 9) ND. Denkov, V. Subramanian, D. Gurovich, A. Lips, "Wall slip and viscous dissipation in sheared foams: Effect of surface mobility", *Colloids Surf A* **263**: 129-145, (2005)
- 10) ND. Denkov, S. Tcholakova, K. Golemanov, V. Subramanian, A. Lips, "Foam-wall friction: Effect of air volume fraction for tangentially immobile bubble surface", *Colloids Surf A* **282-283**: 329-347, (2006)
- 11) SR. Derkach "Rheology of emulsions", *Adv Colloid Interface Sci* **151**: 1-22 (1989)
- 12) P. Dittrich, K. Tachikawa, A. Manz "Micro total analysis systems. Latest advancements and trends", *Anal Chem* **78**: 3887-3908, (1989)
- 13) G. Farzi, M. Mortezaei and A. Badiei, "Relationship between droplet size and fluid flow characteristics in miniemulsion polymerization of methyl methacrylate", *Journal of Applied Polymer Science*, **120**, 1591-1596, (2011).
- 14) S. Guido, F. Greco "Dynamics of a liquid drop in a flowing immiscible liquid", *Rheology Reviews*, 99-142, (2004)
- 15) S. Guido and M. Villone, "Measurement of interfacial tension by drop retraction analysis", *J. Coll. Interf. Sci.*, **209**, 247-250

- 16) R. P. Gullapalli, and B. B. Sheth, "Influence of an optimized non-ionic emulsifier blend on properties of oil-in-water emulsions", *EJPB*, **48**, 233-238 (1999)
- 17) K. R. Hall, and E. Godfrey, "An Experimental and Theoretical. Study of Mixing of Highly Viscous Materials" *AIChE* **10**, 71(1965)
- 18) G. Hetsroni, S. Haber, "The flow in and around a droplet or bubble submerged in an unbound arbitrary velocity field". *Rheol Acta* **9**: 488-496, (1989)
- 19) B.P. Ho, L.G. Leal "The creeping motion of liquid drops through a circular tube of comparable diameter", *J Fluid Mech* **71**: 361-386, (1989)
- 20) D. M. Hobbs, and F. J. Muzzio, "Optimization of a static mixer using dynamical systems techniques" *Chem. Eng. Sci.* **53**, 3199-3213, (1998).
- 21) W.A. Hyman, R. Skalak "Non-Newtonian behavior of a suspension of liquid drops in tube flow", *AIChE* **18**: 149-154, (1972)
- 22) B. H. Junker, T. C. Seamans, K. Ramasubramanyan, J. Aunins, E. Paul and B. C. Buckland, "Cultivation of attenuated hepatitis A virus antigen in a titanium static mixer reactor", *Biotechnology and Bioengineering*, **44**, 1315-1324, (1994)
- 23) A. Kogan, D. E. and H.A. Shalev, U. Raviv, A. Aserin, N. Garti "Formation and Characterization of Ordered Bicontinuous Microemulsions", *J. Phys. Chem.*, **113**;10669-10678, (2009)
- 24) M.J. Martinez, K.S. Udell, "Axisymmetric creeping motion of drops through circular tubes" *J Fluid Mech* **210**: 565-591, (1989)
- 25) M.J. Martinez, K.S. Udell, "Axisymmetric creeping motion of drops through a periodically constricted tube", *AIP Conf Proc*, **197**: 222-234, (1988)
- 26) T. Meyer, R. David, A. Renken and J. Villermaux, "Micromixing in a static mixer and an empty tube by a chemical method" *Chem. Eng. Sci.* **43**, 1955-1960, (1988)
- 27) S. Middleman, "Fundamentals of Polymer Processing", *McGraw-Hill*, (1977)
- 28) W.L. Olbricht "Pore-scale prototypes of multiphase flow in porous media". *Annu Rev Fluid Mech*, **28**: 27, (1996)
- 29) W.L. Olbricht, L.G. Leal, "The creeping motion of liquid drops through a circular tube of comparable diameter: the effect of density differences between the fluids" *J Fluid Mech* **115**: 187-216, (1989)
- 30) E.L. Paul, V. A. Atiemo-Obeng, S. M. Kresta, "Handbook of Industrial Mixing", *Wiley*, (2003)
- 31) J.M. Rallison, "The deformation of small viscous drops and bubbles in shear flows", *Annu Rev Fluid Mech* **16**: 45-66, (1989)

- 32) Rauline, D., Le Blevec J.-M., Bousquet J. and Tanguy, P. A. (2000). *Trans IchemE*, **78**, 389-395.
- 33) M. Shapira, S. Haber, "Low Reynolds number motion of a droplet in shear flow including wall effects", *Int. J. Multiphase Flow*, **16**, 305-321 (1990).
- 34) V. Sibillo, M. Simeone, S. Guido, "Break-up of a Newtonian drop in a viscoelastic matrix under simple shear flow", *Rheologica Acta*, **43**, 449-456 (2004).
- 35) R. J. Stokes, L.J. Graham, N. J., Lawson, D. V. Boger, "Swirling flow of viscoelastic fluids. Part 1. Interaction between inertia and elasticity", *Journal of Fluid Mechanics*, **429**, 67-115 (2001).
- 36) R. J. Stokes, L.J. W. Graham, N. J. Lawson, and D. V. Boger, "Swirling flow of viscoelastic fluids. Part 2. Elastic effects", *Journal of Fluid Mechanics*, **429**, 117-153 (2001).
- 37) HA Stone, "Dynamics of drop deformation and breakup in viscous fluids", *Annu Rev Fluid Mech* **26**: 65-102, (1989)
- 38) G. Tomaiuolo, V. Preziosi, M. Simeone, S. Guido, R. Ciancia, V. Martinelli, C. Rinaldi and B. Rotoli, "A methodology to study the deformability of red blood cells flowing in microcapillaries in vitro", *ISS*, **43**, 186-192 (2007)
- 39) G. Tomaiuolo, M. Simeone, V. Martinelli, B. Rotoli, S. Guido "Red blood cell deformation in microconfined flow", *Soft Matter* **5**: 3736-3740, (1989)
- 40) G. Tomaiuolo, M. Barra, V. Preziosi, A. Cassinese, B. Rotoli and S. Guido, "Microfluidic analysis of red blood cell membrane viscoelasticity" *LOC*, **11**, 449-454, (2010)
- 41) CL. Tucker, P. Moldenaers, "Microstructural evolution in polymer blends". *Annu Rev Fluid Mech* **34**: 33 (1989)
- 42) P. Van Puyvelde, A. Vananroye, R. Cardinaels, P. Moldenaers "Review on morphology development of immiscible blends in confined shear flow", *Polymer* **49**: 5363-5372, (1989)
- 43) J. Vlachopoulos and J.R. Wagner, *The SPE Guide on Extrusion Technology and Troubleshooting*, Society of Plastics Engineers, Brookfield CT (2001)
- 44) G. Whitesides "The origins and the future of microfluidics", *Nature* **442**: 368-373 (2006)
- 45) EJ. Windhab, M. Dressler, K. Feigl, P. Fischer, D. Megias-Alguacil "Emulsion processing--from single-drop deformation to design of complex processes and products", *Chem Eng Sci* **60**: 2101-2113, (1989)

# Appendix

## Publications

1. Tomaiuolo G., Preziosi V., Simeone M., Guido S., Ciancia R., Martinelli V., Rinaldi C., Rotoli B. "A methodology to study the deformability of red blood cells flowing in microcapillaries in vitro, *Ann Ist Sup Sanità*, **43**:186-192, (2007)
2. Guido S., Preziosi V., "Droplet deformation under confined Poiseuille flow", *Advances in Colloid and Interface Science*, **161**: 89-101,(2010)
3. Tomaiuolo G., Barra M., Preziosi V., Cassinese A., Rotoli B., Guido S., "Microfluidic analysis of red blood cell membrane viscoelasticity", *Lab on a chip*, **11**:449-454,(2011)

## Experiences in foreign laboratories

- PhD in collaboration with Brussels innovation center (BIC) of Procter & Gamble in Brussels, Belgium. Under the supervision of Ing. Alberto Simoncelli and in collaboration with Prof. Stefano Guido of the University of Naples (more than 1 year).

## Conferences

- Preziosi V., Kristal J., Simoncelli A. and Guido S., "Microstructure of model emulsion in process flow" 12<sup>th</sup> International conference multiphase flow in industrial plants, September 21-23, 2011
- Caserta S., Preziosi V., Pommella A. and Guido S., "Mixing of liquid-liquid non-newtonian fluids, preliminary results" 12<sup>th</sup> International conference multiphase flow in industrial plants, September 21-23, 2011
- Caserta S., Preziosi V., Ascione F., Tomaiuolo G. and Guido S., "Cell migration *in vitro* by time-lapse microscopy" 10<sup>th</sup> Multinational congress on microscopy 2011, September 4-9, 2011
- Preziosi V., "Microstructure of model emulsion in process flow" World Congress on emulsions October 12-14, 2010

## CONFIDENTIAL ALLEGATE

Part of this thesis has been conducted in collaboration with Procter and Gamble research center in Brussels (BIC), Belgium, and because of confidentiality it will be reported apart in the allegato.



## Droplet deformation under confined Poiseuille flow

Stefano Guido<sup>a,b,\*</sup>, Valentina Preziosi<sup>a</sup>

<sup>a</sup> Dipartimento di Ingegneria chimica, Università di Napoli Federico II, P.le Tecchio 80, 80125 Napoli, Italy

<sup>b</sup> CEINGE-Advanced Biotechnologies, Napoli, Italy

### ARTICLE INFO

Available online 16 May 2010

#### Keywords:

Droplet  
Poiseuille  
Confined  
Surfactant  
Tube

### ABSTRACT

The flow behavior of droplet-based liquid–liquid systems, such as emulsions, polymer blends, and foodstuff, which are ubiquitous in everyday life, has attracted scientific interest in different disciplines. In this review, we focus on the pressure-driven confined flow behavior of isolated droplets in circular and rectangular cross-section channels, which are valuable model geometries to gain insight into more complex flow conditions found in industrial applications. The effect of the relevant nondimensional parameters governing droplet deformation and breakup, such as viscosity ratio, capillary number, and ratio of droplet to tube radius, is presented both for axisymmetric and off-axis droplets, including cross-stream migration. The role of surfactants is also discussed. Ongoing research directions include the field of microfluidics techniques, where confined flow geometries can be exploited to manipulate droplets with a variety of possible applications.

© 2010 Elsevier B.V. All rights reserved.

### Contents

1. Introduction . . . . .	89
2. Droplet deformation in tubes . . . . .	90
2.1. Axisymmetric droplets of radius smaller than or comparable to tube radius . . . . .	90
2.2. Axisymmetric droplets of radius much larger than tube radius . . . . .	93
2.3. Breakup of axisymmetric droplets . . . . .	94
2.4. Off-axis droplet migration and deformation . . . . .	95
3. Droplet deformation in rectangular channels . . . . .	96
3.1. Poiseuille flow between parallel plates . . . . .	96
3.2. Three-dimensional Poiseuille flow in rectangular channels . . . . .	97
4. Effects of surfactants in Poiseuille flow . . . . .	98
5. Conclusions . . . . .	100
Acknowledgements . . . . .	100
References . . . . .	100

### 1. Introduction

A droplet-based microstructure is found in most liquid–liquid industrially relevant systems, such as emulsions, polymer blends and foodstuff. These systems, starting from the pioneering work of Taylor on the deformation of droplets in simple shear flow [1,2], have attracted a strong scientific interest in different fields, from fluid mechanics to geophysics. The study of the flow behavior of droplets is more complicated in concentrated systems due to hydrodynamic interactions between the droplets, possibly leading to coalescence

phenomena, and in complex flow geometries, where both shear and extensional components can be at work in a time-dependent manner. In fact, the rheological properties of these materials are linked to the flow conditions by a complex interplay, since a flow-induced change of microstructure can in turn affect system viscosity [3,4].

To get some insight into this problem a basic approach has been followed in the literature, where the idealized situation of an isolated droplet in a well-defined flow field has been investigated. In spite of the gross simplifications associated with this approach, many significant results and some fundamental understanding have been obtained by studying the flow behavior of an isolated droplet under simple shear or elongational flow, as reviewed in several papers [5–8]. Here, we focus on Poiseuille flow in cylindrical and rectangular channels, which is a somehow more complex problem due to the presence of a shear rate

\* Corresponding author. Dipartimento di Ingegneria chimica, Università di Napoli Federico II, P.le Tecchio 80, 80125 Napoli, Italy. Tel.: +39 081 7682271; fax: +39 081 2391800.

E-mail address: [steguido@unina.it](mailto:steguido@unina.it) (S. Guido).

gradient in the flow geometry. This is also a quite interesting case being close to flow conditions encountered in industrial processing (such as in fluid transport and mixing operations). Another possible application is the study of oil recovery from porous media, which can be modeled as channel networks [9]. Furthermore, Poiseuille type of flow is found in microfluidics devices, where the effect of confinement is quite significant [10]. The motion of droplets under confined flow has also attracted some interest due to the similarities with the shape taken by red blood cells in microcapillaries [11,12].

From the experimental point of view, droplet deformation under confined Poiseuille flow has been studied by coupling an optical microscope to a transparent flow device. In some works streamline visualization was achieved by micro-particle image velocimetry (some examples will be presented in Section 3.2). The problem has been also addressed by numerical simulations, mostly based on boundary integral methods.

The review is organized as follows. Section 2 is devoted to the study of droplet deformation and breakup in circular cross-section channels. The effects of the relevant physical parameters, including the droplet to tube radius, the viscosity ratio between the two phases and the capillary number, i.e., the ratio between viscous and interfacial forces, are discussed. Both axisymmetric and off-axis droplets are considered. Droplet flow in rectangular channels is discussed in Section 3, with a special emphasis on microfluidics applications. The effect of surfactants on droplet deformation in Poiseuille flow is reviewed in Section 4. Finally, possible future directions and challenges in the investigation of droplet deformation in Poiseuille flow are presented in the concluding section.

## 2. Droplet deformation in tubes

The motion of a droplet of radius  $a$  translating with velocity  $U$  in an external immiscible fluid undergoing pressure-driven flow in a cylindrical tube of inner radius  $R$  is schematically represented in Fig. 1. The average value of the undisturbed parabolic velocity profile of the external fluid far away from the droplet is  $V$ . The nondimensional parameters governing droplet motion with Newtonian fluid components are the ratio  $\lambda$  between the viscosity  $\eta_d$  of the droplet phase and the viscosity  $\eta_c$  of the external phase, the capillary number  $Ca = \eta_c V/\sigma$ , where  $\sigma$  is the interfacial tension, and the ratio  $k$  between the droplet and tube radius. For non-Newtonian fluids an additional nondimensional parameter representing the ratio of normal stresses and interfacial tension comes into play [12]. The main experimental observables are the nondimensional droplet velocity  $U/V$  and the excess pressure drop  $\Delta P^+$  due to the presence of the droplet (i.e., the difference between the tube pressure drop with and without the droplet) made nondimensional with respect to the characteristic pressure  $\eta_c V/R$ . Other quantities which can be experimentally measured are the thickness of the fluid layer separating the droplet surface and the tube wall and the droplet migration velocity in the radial direction. By using flow visualization techniques one can also image the external and internal streamline patterns. Most available theories allow one to make predictions of these flow-related quantities to be compared with experiments. This subject has been reviewed by Olbricht [9].

In the following of this section droplet deformation at low droplet-based Reynolds number  $Re = \rho Va/\eta_c$  is considered. Subsections 2.1 and 2.2 are devoted to the axisymmetric cases of low and high values of  $k$  (i.e., small and large droplets with respect to tube radius), respectively, including the effect of buoyancy. Axisymmetric droplet breakup is discussed in Subsection 2.3. Off-axis droplet deformation and migration, and the effect of Reynolds number are the subject of Subsection 2.4.

### 2.1. Axisymmetric droplets of radius smaller than or comparable to tube radius

Droplet deformation at small values of  $k$  has been the subject of previous reviews. From the theoretical point of view, Hetsroni et al. [13] investigated the case of small undeformed droplets ( $k \ll 1$ ) moving along the tube axis, and found the following equation for the nondimensional droplet velocity  $U/V$

$$\frac{U}{V} = 2 - \frac{4\lambda}{3\lambda + 2} k^2 + O(k^3) \quad (1)$$

which shows that droplet velocity lies in between the maximum (centerline) and the average velocities of the undisturbed flow (the maximum velocity being equal to twice the average velocity). By using the so calculated velocity field, Hetsroni et al. [13] applied the boundary condition on the normal stress, which is not satisfied in the case of a spherical droplet, to generate a first approximation of droplet shape under flow.

In the same limit of  $k \ll 1$ , the excess nondimensional pressure drop is given by Brenner and Bungay [14] as

$$\frac{\Delta P^+ R}{\eta_c V} = \frac{16[(9\lambda + 2)^2 - 40]}{27(\lambda + 1)(3\lambda + 2)} k^5 + O(k^{10}) \quad (2)$$

According to Eq. (2), the excess pressure drop due to the presence of a droplet can be negative if the viscosity ratio is less than 0.48. Furthermore, even though Brenner's theory was developed for  $k \ll 1$ , the small residual error in Eq. (2) shows that the prediction should be valid at somehow higher values of  $k$ .

For intermediate values of  $k$ , the effect of the capillary number becomes significant both on the excess pressure drop and droplet velocity. From the experimental side, the problem has been tackled by Ho and Leal [15] and Olbricht and Kung [16], who investigated the shape of a deformed droplet in a range of values of the nondimensional parameters  $k$ ,  $\lambda$  and  $Ca$ . In Fig. 2 images of droplet shape at  $\lambda = 0.99$  are shown at values of  $k$  from 0.95 to 1.13 (from left to right) and of  $Ca$  from 0.05 to 0.16 (from top to bottom) [9]. At each value of the capillary number, increasing  $k$  results in a more elongated droplet. In a similar way, by increasing  $Ca$  at any value of  $k$  the droplet becomes more stretched in the flow direction and the thickness of the fluid layer between the interface and the tube wall increases. Furthermore, the curvature of the trailing edge decreases at higher values of  $Ca$ , while the leading edge maintains a constant, sharper shape. On the other hand, the viscosity ratio does not affect droplet shape as much as  $Ca$  in this intermediate  $k$  range, at least up to  $\lambda$

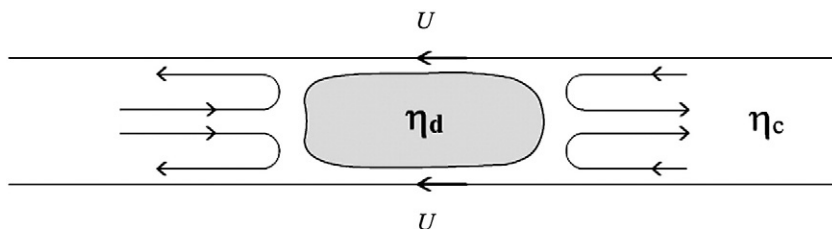
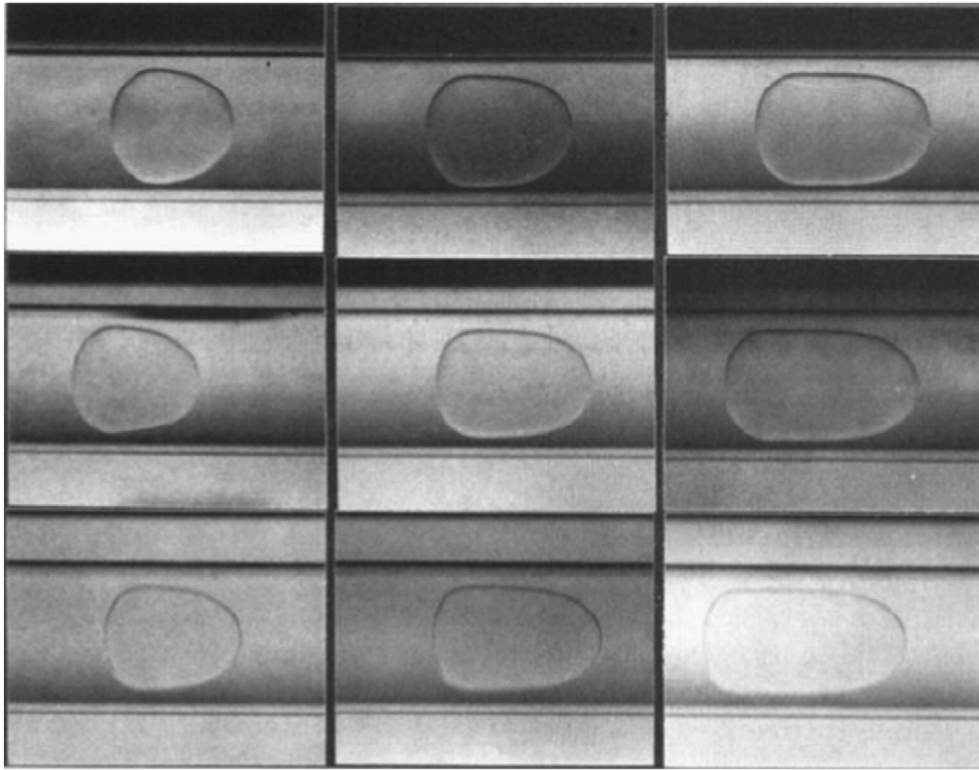


Fig. 1. Schematic of a droplet translating in an immiscible fluid under the action of confined pressure-driven flow. The frame of reference is moving with the droplet.



**Fig. 2.** Steady-state droplet shape at  $\lambda = 0.99$  with  $k = 0.95$  (left column), 1.05 (middle column) and 1.13 (right column) and with  $Ca = 0.05$  (top row), 0.10 (middle row) and 0.16 (bottom row) [9].

around 2 [16]. Interestingly, as pointed out by Ho and Leal [15], higher viscosity ratios are associated to larger droplet deformation, keeping fixed the other parameters. This result, though opposite to the intuitive notion that less viscous droplets should be more deformable, is in line with the perturbation theory of Hetsroni [13] and with numerical simulations [17]. The latter provide an explanation for this result, as discussed in the following.

Ho and Leal [15] studied a train of droplets, with separation large enough to avoid hydrodynamic interactions, in the range of  $k$  from 0.726 to 1.1 and of  $\lambda$  from 0.2 to 2. Both droplet velocity and excess pressure were measured. A comparison between such experimental data and calculations from the literature is presented in Figs. 3 and 4, both taken from Martinez and Udell [18]. In Fig. 3 the quantity  $\frac{U}{V}$  is plotted as a function of  $k$  at two viscosity ratios. The experimental data are a decreasing function of  $k$  up to about 0.9 as predicted by Eq. (2), and then become independent on  $k$ . This finding is in agreement with a previous study by Goldsmith and Mason on large droplets and bubbles [19]. Ho and Leal [15] showed that the theoretical predictions of Eq. (2) (not shown in Fig. 3), being valid for  $k \ll 1$ , overestimate the experimental results, which start from  $k = 0.726$ . The dotted lines are finite differences numerical calculations of Hyman and Skalak at  $\lambda = 0$  and 1 [17]. These calculations are in good agreement with the experimental data at  $\lambda = 0.93$  and predict a value of  $U = 2V$  for vanishing  $k$ , i.e., a small droplet on the tube axis travels with the centerline maximum velocity. The full lines are boundary integral numerical simulations by Martinez and Udell [18] and slightly exceed the experimental values of 2–7% in the range investigated. The numerical solutions in Fig. 3b exhibit a minimum at  $0.8 \leq k \leq 1$  corresponding to a maximum in drop girth at  $k \approx 0.9$  (in other words, a droplet at  $k \approx 0.9$  shows a broader profile and travels slightly slower than a larger droplet).

The values of  $\frac{\Delta P^+ R}{\eta_c V}$  measured by Ho and Leal [15] are plotted as a function of  $k$  in Fig. 4 together with the numerical simulations by Martinez and Udell [18] (full lines) and finite differences calculations by Hyman and Skalak [17] for undeformed droplets and at  $\lambda = 0$  (top

diagram) and  $\lambda = 1$  and 10 (bottom diagram). For  $k \leq 0.5$  the numerical calculations show that the additional pressure drop due the droplet is rather small, but it exhibits a drastic increase with  $k$  thereafter. Calculations and experimental data are insensitive to  $Ca$  for  $k \leq 0.5$ , and tend to collapse on the same curve. Furthermore, the effect of  $Ca$  at low values of  $\lambda$  is hard to distinguish in the experimental results. In any event, the effect of increasing  $Ca$  is to reduce the extra pressure drop, and this trend can be explained by the higher droplet elongation and the thicker intervening fluid layer at larger values of  $Ca$ . The most striking feature of Fig. 4 is, however, the fact that  $\frac{\Delta P^+ R}{\eta_c V}$  can be either positive or negative, mainly depending on the viscosity ratio. This result is in agreement with Eq. (2), which predicts that the extra pressure drop is negative for  $\lambda < 0.48$ . In fact, the theoretical analysis underlying Eq. (2) is only valid for small  $k$ . Data from Ho and Leal [15] show that at  $\lambda = 0.58$  the sign of the extra pressure drop changes from positive to negative at increasing  $k$ . The change of the extra pressure drop at  $k > 0.95$  can be estimated by a simple model proposed by Ho and Leal [15] based on the limiting case of two coflowing liquids one of which travels in an annulus region close to the tube wall. This model is in good agreement with the numerical results by Martinez and Udell [18] and provides a simple explanation of the negative extra pressure drop found at low viscosity ratios.

Some insight on fluid dynamic features of droplet deformation can be obtained by looking at the outer and inner flow fields. In Fig. 5 calculated velocity vector fields (left diagrams) [18] and experimental streamline patterns (right panel) [15] are shown in a frame of reference translating with the droplet. Both experiments and simulations show a fluid recirculation with zero net flux inside the droplet, where a forward motion is seen in the central region and a compensating rear flow takes place in a shell close to droplet interface. Two stagnation rings are present on the interface due to the fact that fluid elements close to the centerline travel faster than the droplet while those near the wall lag behind (the latter gives rise to a leak-back flow of the suspending fluid in the layer between droplet interface and tube wall). The stagnation rings

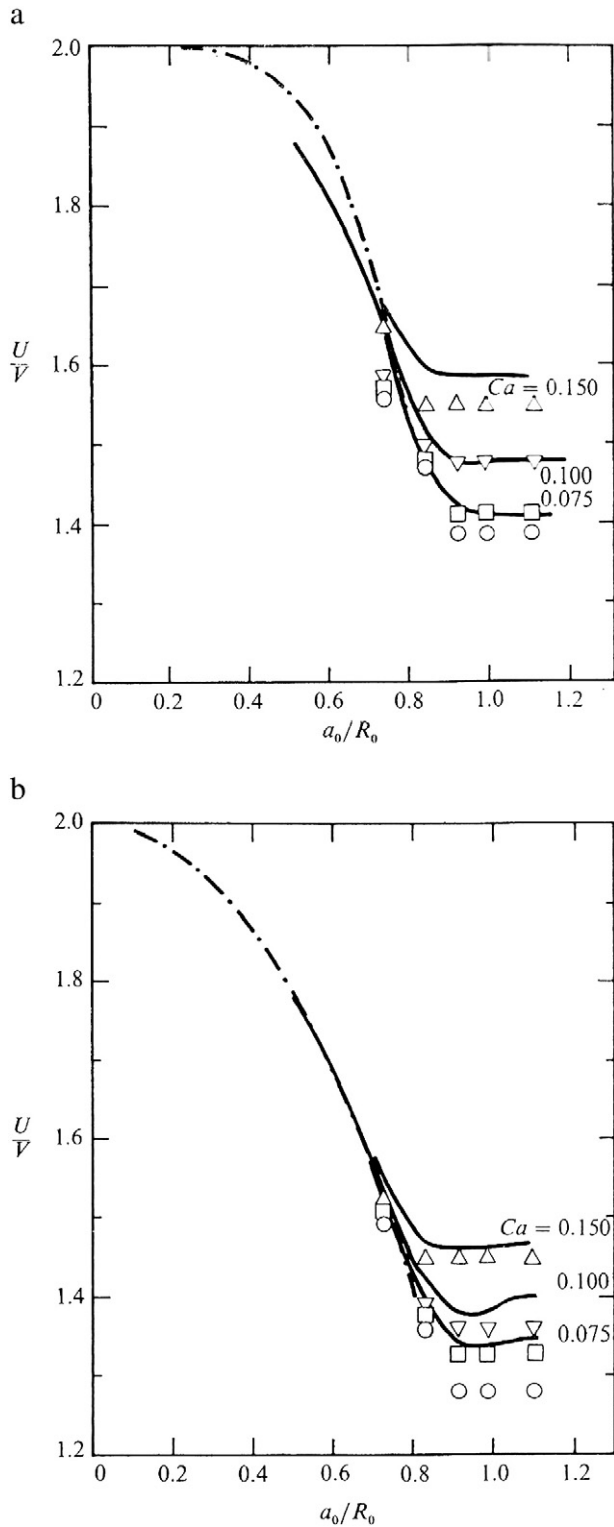


**Fig. 3.** Nondimensional droplet velocity as a function of  $k$  at two values of the viscosity ratio: 0.19 (a) and 1.0 (b). Full lines are predictions of Martinez and Udell [18], while dashed-dotted lines are calculations by Hyman and Skalak [17]. Open symbols are data by Ho and Leal [15] at viscosity ratios of 0.19 (a) and 0.93 (b). Reproduced with permission from Martinez and Udell [18].

are associated with a bolus of fluid between two consecutive droplets, which is clearly visible in the middle and bottom picture of the right panel. The bolus travels with the same velocity of the droplets. The stagnation rings play a role in insoluble surfactant convection at the

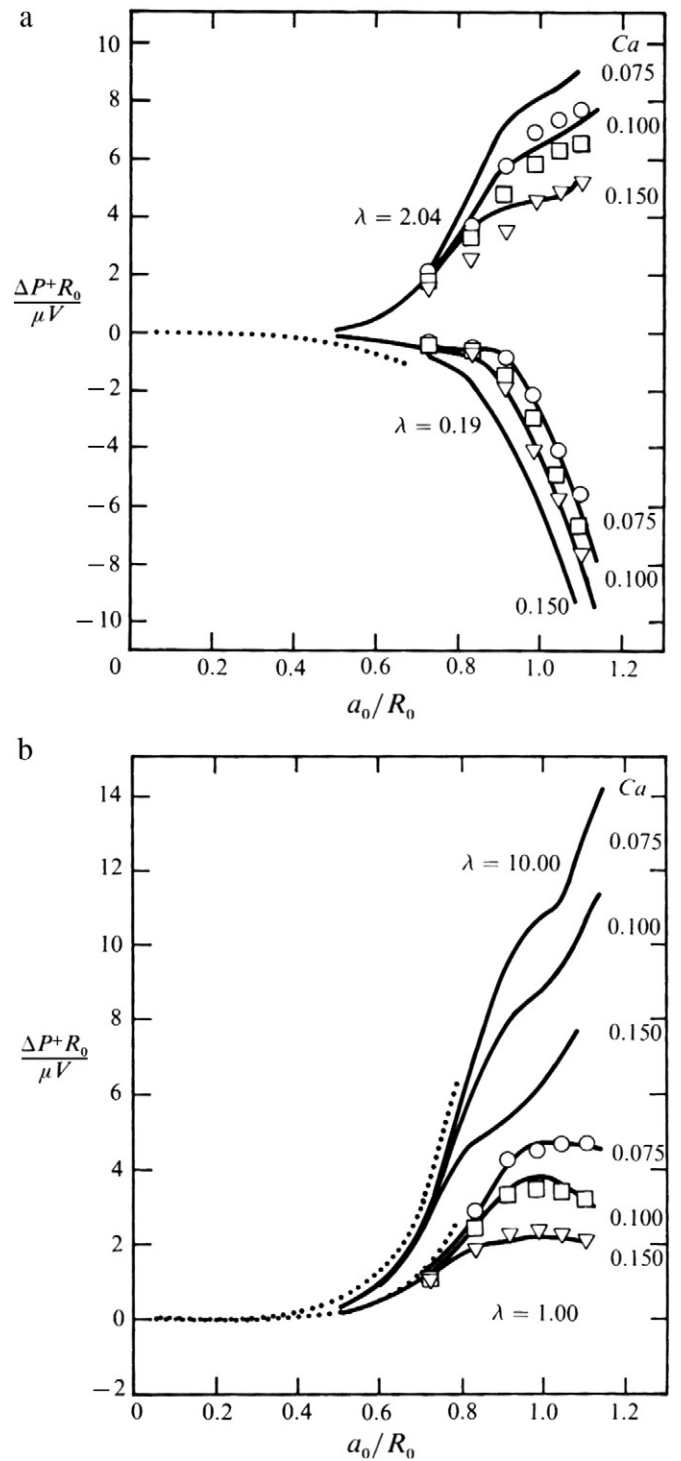


**Fig. 4.** Nondimensional extra pressure drop as a function of  $k$  at different values of the viscosity ratio and of the capillary number. Full lines are predictions of Martinez and Udell [18], while dotted lines are calculations by Hyman and Skalak at  $\lambda = 0$  (for spherical droplets, a), 1 (b) and 10 (b) [17]. Open symbols are data by Ho and Leal [15] (circles:  $Ca = 0.075$ , squares:  $Ca = 0.100$ , and triangles:  $Ca = 0.150$ ). Reproduced with permission from Martinez and Udell [18].

interface as it will be discussed later. Similar flow patterns are in agreement with other studies [19]. The somehow counterintuitive increase in droplet deformation at high viscosity ratio can be also explained in terms of the velocity vector field by exploiting the normal stress balance across the fluid interface [18].

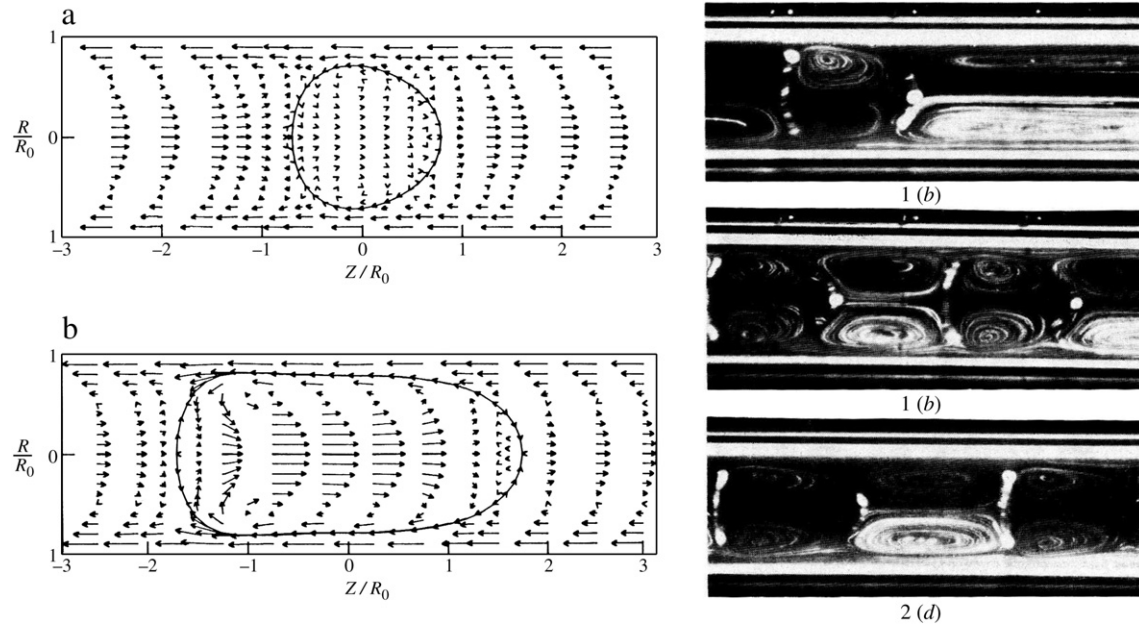


**Fig. 5.** Calculated velocity vector fields (left diagrams) [18] and experimental streamline patterns (right panel) [15] in pressure-driven tube flow. The parameters used in the calculations are  $k=0.726$ ,  $Ca=0.10$  and  $\lambda=10$  (left top diagram) and  $k=1.10$ ,  $Ca=0.10$  and  $\lambda=0.19$  (left bottom diagram). The experimental pictures on the right refer to  $Ca=0.10$  and  $\lambda=2.04$  (top and middle) and to  $Ca=0.18$  and  $\lambda=0.93$ .

The effect of buoyancy under pressure-driven flow in horizontal tubes was studied in the case of a small density difference by Goldsmith and Mason [19] for very small droplets ( $k \leq 0.07$ ) and by Olbricht and Leal [20]. The main consequence of a slight density difference between droplet and continuous phase is a decrease of droplet mobility and a parallel increase of the extra pressure drop as a result of droplet displacement towards the tube wall. When droplets get close to the wall a correlation between the extra pressure drop and the distance of the droplet from the tube wall was found [20]. Borhan and Pallinti [21] have investigated the effect of buoyancy under pressure-driven flow in vertical tubes as a function of  $k$ ,  $Ca$ ,  $\lambda$ , the relative density difference, and the Bond number  $Bo = \Delta\rho g R^2 / \sigma$ , which is the ratio of buoyancy and interfacial forces. The relative droplet mobility and the thickness of the intervening fluid layer between droplet and tube wall are both enhanced at increasing Bond number up to a limiting  $Bo$  value, beyond which constant values are approached. Such limiting Bond number is a decreasing function of the capillary number. Furthermore, the development of a negative concavity at the trailing end of the moving droplet is inhibited by increasing  $Bo$  when pressure and buoyancy forces act in the same direction [21].

Starting from the pioneering work of Hadamard [22], several other papers have been devoted to the effect of buoyancy in gravity-driven flow in vertical tubes (see for example [23] and [24]). This subject, though quite relevant in many applications, is outside the scope of this review and will be not considered here.

## 2.2. Axisymmetric droplets of radius much larger than tube radius

This case has been especially investigated at  $\lambda = 0$ , since slug flow (i.e., the periodic occurrence of long bubbles separated by liquid plugs, often referred to as Taylor bubbles) can be used to enhance mass and heat transfer in industrial and biological processes, such as reactors with catalytically active walls and blood flow in pulmonary and peripheral capillaries [25]. Here, we focus on a preferentially wetting suspending fluid, leaving aside the problem of moving contact lines, which has been the subject of several papers (see for example Sheng and Zhou [26]).

For  $k \gg 1$  the shape taken by a bubble or a droplet in a tube resembles a cylinder with two hemispherical caps. In this regime, as reported by Goldsmith and Mason [19], the thickness of the intervening fluid layer between droplet and tube wall becomes constant with  $k$ . An asymptotic behavior of  $U/V$  has been also found at increasing  $k$  [18] (see Fig. 3). A classical theoretical analysis of a long inviscid fluid in a tube has been provided by Bretherton [27], who showed that the fluid layer thickness and the extra pressure drop are both dependent on  $Ca^{2/3}$  for small  $Ca$ . More recently, the problem of a viscous droplet moving in a cylindrical tube has been investigated by Hodges et al. [28], who found that the  $Ca^{2/3}$  scaling is appropriate for all values of  $\lambda$ , but with an order unity coefficient weakly dependent on both  $\lambda$  and  $Ca$ . The intervening fluid layer thickens for viscous droplets as compared to an inviscid bubble. According to Hodges et al. [28], as  $\lambda$  increases from 0, film thickening goes through an overshoot before reaching a plateau at a factor  $2^{2/3}$  as  $\lambda \rightarrow \infty$ . The analysis was extended to larger values of the capillary number by numerical methods [29]. Numerical simulations of a droplet flowing in a confined microchannel with a 5:1:5 contraction – straight narrow channel – expansion flow domain have been presented by Chung et al. [30]. They found a power-law dependence of both the fluid layer thickness and the extra pressure drop on the capillary number, with an exponent varying with the viscosity ratio. A reduction of the excess pressure drop due to fluid elasticity (taken into account by using the Oldroyd-B constitutive model) has been also reported.

From the experimental point of view, early data on the motion of long bubbles have been reported by Fairbrother and Stubbs [30], who found that film thickness depends on the capillary number only, and scales as  $Ca^{1/2}$  for  $Ca$  up to  $O(10^{-1})$ , in contrast with the  $Ca^{2/3}$  scaling predicted by Bretherton [27]. In fact, later studies confirmed such discrepancy between experiments and theory. Taylor [31] found that the relative velocity between bubble and liquid scales as  $Ca^{1/2}$  with a limiting value of 0.56 at large  $Ca$ . An asymptotic value of 0.60 was later reported by Cox [32]. In a later study, Schwartz et al. [33] investigated the effect of viscosity, which was found to increase the film thickness, without affecting the dependence on  $Ca$ . Recently, an experimental investigation of a liquid slug has been reported by Dong et al. [34], but no comparison with theoretical predictions has been provided.

A possible interpretation of the discrepancy between theory and experiments is the presence of surface-active agents at the bubble or droplet interface. Bretherton [27] considered the effect of surfactants as changing the boundary condition at the gas/liquid interface from stress-free to no-slip. This variation of boundary condition, however, does not modify the  $Ca$  scaling. Later studies show that by taking into account the Marangoni stresses induced by surface tension interfacial gradients a larger film thickness and a weaker dependence on  $Ca$  than  $Ca^{2/3}$  are obtained, thus improving the agreement with the experimental results [35,36]. Furthermore, experimental values of the extra pressure drop due to a large bubble in a capillary are much higher than Bretherton predictions when a surfactant is present [37]. Deviations from the  $Ca^{2/3}$  scaling of bubble-wall friction force at small  $Ca$  were also found by Denkov et al. [38,40], who performed both numerical calculations based on lubrication theory and experiments by reflected light microscopy.

### 2.3. Breakup of axisymmetric droplets

By increasing the capillary number, the flow-induced deformation of a droplet translating in a tube becomes larger, until a stable shape is no longer observed and breakup takes place at some critical value  $Ca_{cr}$ . The droplet breakup modes in tube flow are quite different with respect to the ones found in unbounded [39,40] and confined [41,42] simple shear

flow between parallel plates. In these flow geometries, at  $Ca \geq Ca_{cr}$  the droplet keeps elongating under the action of flow until it breaks up in two main daughter droplets and smaller satellites in between, the number of fragments being determined both by the value of  $\lambda$  and the distance from the critical point. At variance with this behavior, droplet breakup in tube flow at  $\lambda < 1$  is preceded by the development of a re-entrant concave zone at the trailing edge [19], as shown in the upper image of the top panel in Fig. 6 [9]. A similar shape has been found in numerical simulations at  $\lambda < 1$  and large values of  $Ca$  by Chi [43] and Martinez and Udell [18]. The breakup process continues on with the penetration of a viscous jet entraining suspending fluid inside the droplet from the trailing edge, as shown in the other images of the top panel in Fig. 6, eventually leading to the formation of multiple fragments. At a given  $\lambda$ , the critical capillary value for breakup in tube flow is higher as compared to that in simple shear flow (e.g.,  $Ca_{cr} = 0.75$  in tube flow [16] and 0.43 in simple shear flow [40] at  $\lambda = 1$ ). A comparison with numerical simulations by Tsai and Miksis [44] is also presented in Fig. 6 (bottom plot), and a good qualitative agreement is observed. The breakup mode observed in tube flow can be explained in terms of the normal stress boundary condition [8]. At small  $Ca$  the inner flow is inconsequential and the pressure inside the droplet is essentially constant. At increasing  $Ca$  the curvature of the trailing edge becomes larger until a hemispherical shape is attained locally, which corresponds to the maximum stress difference across the trailing edge interface.

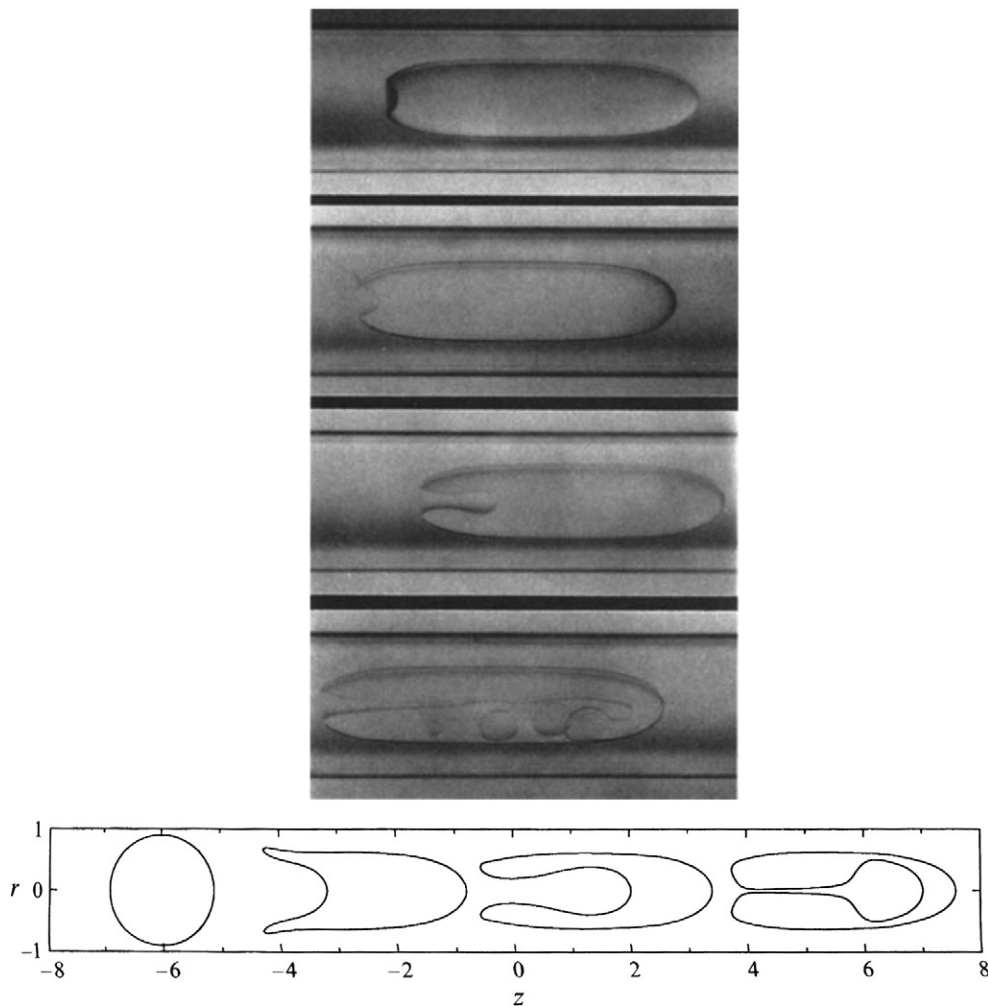


**Fig. 6.** Top panel: sequence of images showing droplet breakup by formation of a re-entrant jet at the trailing edge. Bottom plot: flow-induced shape evolution of a droplet with  $k = 0.9$ ,  $\lambda = 0.1$  and  $Ca = 1.0$  at nondimensional time  $t = 0, 2, 4, 6$ . Reproduced with permission from Olbricht [9] (top panel) and Tsai and Miksis (bottom plot) [44].

Upon further increasing the capillary number, no stable shape can satisfy the normal stress boundary conditions and a re-entrant jet develops at the trailing edge leading to droplet breakup [9]. The breakup mode changes qualitatively at  $\lambda \geq 1$ , where both boundary integral calculations of Chi [43] and experiments of Olbricht and Kung [16] show that droplet length increases without bound at  $Ca_{cr}$  (the actual breakup event was not observed experimentally since droplets kept on elongating all the way down the tube outlet). By increasing  $k$ , the critical capillary number decreases and then becomes independent on  $k$  for  $k > 0.83$ . In a similar way, by increasing  $\lambda$ ,  $Ca_{cr}$  first decreases (in agreement with the higher droplet deformability at higher  $\lambda$ ) and then becomes constant for  $\lambda > 0.5$  [9].

Another interesting breakup mode, the so called snapoff, is observed for low viscosity droplets and bubbles moving in a tube with a constriction. In this geometry, which mimicks the local changes in cross-sectional area characteristic of porous media, flow is unsteady in the Lagrangian sense, and droplet motion changes depending on the driving force, i.e., whether a constant pressure difference or a constant volumetric flow rate is applied. For small  $Ca$ , a droplet undergoes sudden movements called Haines jumps since it can only pass through a constriction provided that the pressure drop becomes large enough [8]. At higher  $Ca$ , Olbricht and Leal [45] showed that in a periodically constricted capillary tube droplet shape and velocity are also periodic, as well as the extra pressure drop. In particular, the maximum flow resistance, corresponding to the highest extra pressure drop, occurs when the droplet goes through the constriction, while the minimum flow resistance is found as the droplet enters the wide section of the tube. The experimental results of Olbricht and Leal [45] are in qualitative agreement with the numerical simulations of Martinez and Udell [46], who made the calculations at the same values of the experimental parameters. Droplet breakup can take place when the droplet cannot fully retract before the leading edge enters a new constriction. In this situation droplet stretching occurs leading eventually to breakup (Martinez and Udell [46]). On the other hand, snapoff is observed at low  $Ca$  when a suspending liquid annulus is formed through the constriction. The higher interface curvature in the constriction is associated with a lower pressure in the suspending liquid (the inner pressure being almost constant or slightly decreasing due to the low average velocity). As a consequence, more suspending liquid is driven into the annulus region until breakup occurs [9]. This situation is schematically represented in Fig. 7a [47]. The snapoff process has been analyzed by Tsai and Miksis through numerical simulations. As shown in Fig. 7b, snapoff is only found in an intermediate range of  $Ca$ . In fact, small values of the capillary number are associated with a very thin film which does not grow enough through the constriction to allow breakup. At the other extreme, if  $Ca$  is too large the droplet does not have a long enough residence time through the constriction and snapoff cannot take place. Thus, in Fig. 7b snapoff is only observed at  $Ca = 0.10$  (middle plot). Recently, snapoff of oil droplets in a capillary constriction as a function of capillary number and viscosity ratio has been experimentally investigated by Peña et al. [49]. In the investigated range of parameters, snapoff was found at low viscosity ratios for any value of  $Ca$  and never observed at high  $\lambda$ . At intermediate viscosity ratios snapoff was only found at low enough values of  $Ca$ .

Recently, droplet motion through a constriction has been analyzed by Graham and Higdon [49,50] by using a finite-element approach to simulate axisymmetric squeezing through a tight constriction at non-zero Reynolds number. Davis and Zinchenko [51] considered the problem of emulsions flowing in random granular media, where droplets can squeeze through the interparticle constrictions and possibly breakup if  $Ca$  is high enough.

#### 2.4. Off-axis droplet migration and deformation

Cross-flow migration of a droplet in tube flow is a problem of technological interest *per se*. For example, in processing two-phase

materials such as polymer blends a uniform spatial distribution of the dispersed phase droplets can be desired in order to have homogeneous products properties. On the other hand, in some cases it could be useful to have a higher concentration of one phase near the surface of the finished product. In any event, cross-flow droplet migration is a subject relevant for applications where control of spatial droplet distribution is of interest [52].

Early experimental measurements of droplet migration in Poiseuille flow were performed by Goldsmith and Mason [53,54], Karnis et al. [55], and Karnis and Mason [56], as reviewed by Brenner [57]. At viscosity ratios up to 10, droplets were found to migrate towards the centerline at a rate increasing with droplet radius, velocity gradient and radial distance from the tube axis. When the viscosity ratio reached the value of 50, and droplet deformation was negligible, a behavior similar to solid spheres was observed, i.e., no migration at low particle Reynolds number  $Re_p = \frac{\rho UR}{\eta_c} (< 10^{-6})$  and migration at halfway the distance between the centerline and tube wall at higher  $Re_p$ . Similar results were found in pulsatile Poiseuille flow [58].

Theoretical analyses to explain the experimental data of Mason and co-workers were first proposed by Chaffey et al. [59,60] who considered the effect of a single wall on the migration of a droplet in simple shear flow. Cross-flow droplet motion was found to be directed away from the wall. In later theoretical works by Haber and Hetsroni [61] and Wohl and Rubinow [62] the migration of droplets in unidirectional shear flow with a shear gradient was investigated without considering wall effects. With the exception of the former work (which was apparently affected by algebraic errors [63]) inward droplet motion towards the tube centerline was found in qualitative agreement with the experimental data. Chan and Leal [63] performed 2D and 3D theoretical analyses for nearly spherical droplets with radius smaller than tube radius both for Newtonian and second-order fluids assuming  $\lambda < 1/Ca$ . For two-dimensional flow it was found that the droplet migrated towards the walls for  $0.5 < \lambda < 10$  and towards the centerline for  $\lambda < 0.5$  and  $\lambda > 10$ . In the case of three-dimensional unbounded Poiseuille flow they derived a closed-form expression of the migration velocity, which was in good agreement with the experiments of Goldsmith and Mason [54] at low viscosity ratios, although the measured rate of droplet migration was slightly larger than the predicted one. The latter discrepancy was attributed to the neglect of walls effects in the theoretical analysis. The theoretical predictions were compared to experimental data of Gauthier et al. [64] on the lateral migration of Newtonian droplets in viscoelastic fluids in Poiseuille flow. These experiments show that migration is directed towards an equilibrium position between the wall and the centerline for pseudoplastic fluids. The theoretical predictions of Chan and Leal were also compared to data of droplet motion in a continuous phase made of a solution of polyisobutylene in decalin, which is an experimental model (the so called Boger fluid) of a second-order fluid. Some discrepancy was found and it was attributed to the fact that droplet interaction with the bounding wall, which can have the same effect as normal stresses in non-Newtonian fluids, was not accounted for.

The cross-flow migration of droplets in Poiseuille flow has been also studied by numerical simulations using boundary integral simulations. Some insight on wall effects can be obtained by studying the behavior of a droplet close to a solid boundary under simple shear flow. Numerical simulations of this case were presented by Uijttewaai et al. [65], Kennedy et al. [66] and Uijttewaai and Nijhof [67], who found that all the droplets migrated away from a plane boundary and exhibited an increased deformation as compared to unbounded flow. Wall effects were more significant at higher  $\lambda$ , and the computed migration velocities were higher than those calculated by small deformation theories. Furthermore, the computed migration velocities [66] were smaller than the experimental one by Karnis and Mason [56]. Coulliette and Pozrikidis [68] studied the motion of an array of droplets through a cylindrical tube by three-dimensional simulations

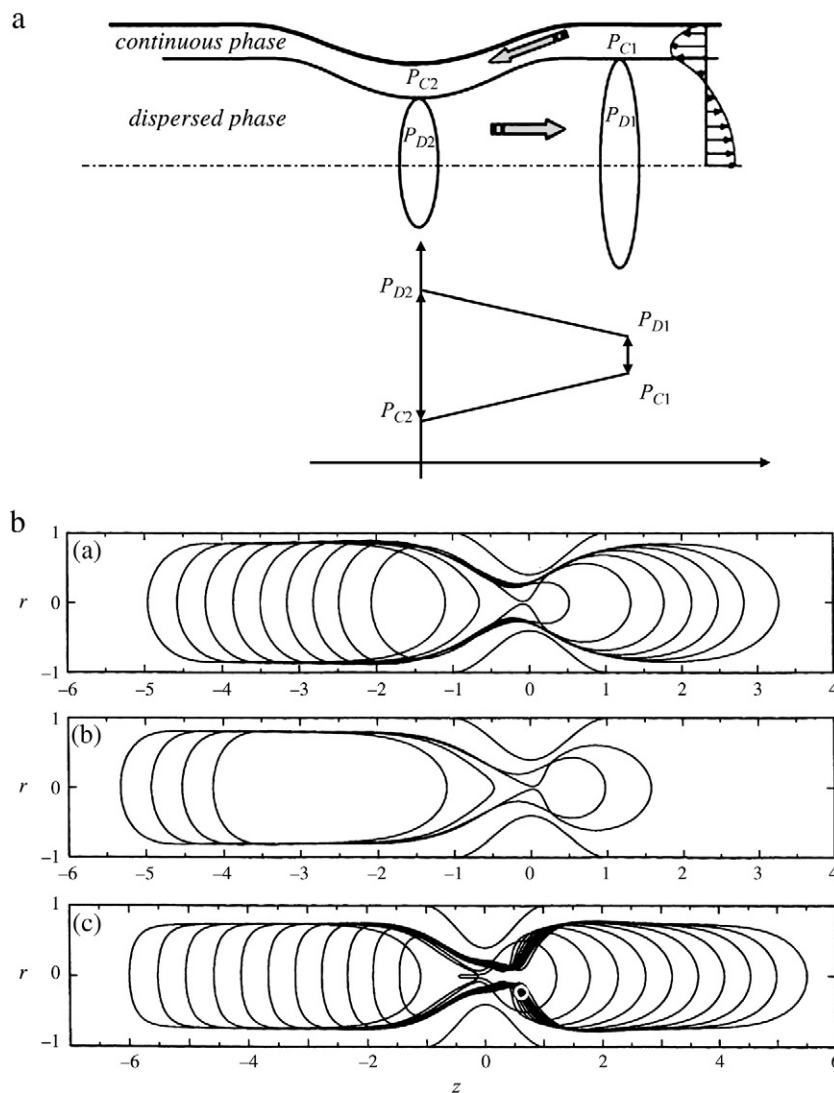


**Fig. 7.** a) Schematics of the pressure drops eliciting snapoff ( $P_C$  and  $P_D$  are local pressure in the continuous phase and droplet, respectively) [48]; b) numerical simulations of droplet motion through a constriction [44] at  $k=0.9$ ,  $\lambda=0.001$  and  $Ca=0.05$  (top), 0.10 (middle) and 0.20 (bottom).

at  $\lambda=1$ . In the case of off-axis small droplets, the shape of the deformed droplets was equal to that found in simple shear flow at the same capillary number based on the local value of shear rate. At variance with the predictions of Chan and Leal [63], small droplets migrate towards the centerline. The inner flow field is characterized by an eddy, whose center is displaced close to the wall at higher droplet size relative to tube radius (in this case a bolus of fluid is observed if the droplets spacing is greater than about one tube diameter). In the case of off-axis large droplets, for which the undeformed shape intersects the centerline, a dimple may form at the rear of the deformed droplets and a slipper shape, similar to that of red blood cells in confined flow, is observed. As shown in Fig. 8 the configuration of the rear interface depends on the off-center distance. Droplet migration is again directed to the centerline, even though it can be initially directed towards the wall. The interior flow pattern is similar to the one calculated by Martinez and Udell [18].

Droplet deformation and breakup in confined shear and extensional flow have been studied by Mietus et al. [70]. By using a transparent horizontal annular Couette flow cell different breakup modes and complex droplet structures have been identified. The combination of shear and elongational flows is especially relevant for mixing devices, where the interaction between these flow types and the confining surfaces plays a key role on product microstructure.

### 3. Droplet deformation in rectangular channels

The investigation of droplet motion in rectangular channels has recently attracted more attention due to interest in droplet-based microfluidics applications. In the following of this section two-dimensional Poiseuille flow will be reviewed first. In the second subsection confined three-dimensional flow of droplets in rectangular channels will be considered.

#### 3.1. Poiseuille flow between parallel plates

Experimental measurements of droplet motion in plane Poiseuille flow were carried out by Hiller and Kowaleski [69] by using a laser Doppler anemometer for  $k=0.064$  and  $\lambda=0.1, 1$  and 15. Mean droplet concentration was kept very small in order to focus on single droplet behavior. At  $\lambda=0.1$  a pronounced peak in the droplet spatial distribution was found close to the wall at the channel inlet. The peak moves slowly towards the centerline at increasing distance from the inlet until it finally disappears. At  $\lambda=1$  the peak is still present at the channel inlet and increases along the channel while slowly moving towards the centerline. The number of droplets around the centerline decreases along the channel, thus showing that the droplets move towards the walls. A similar trend is observed at  $\lambda=15$ , apart from a

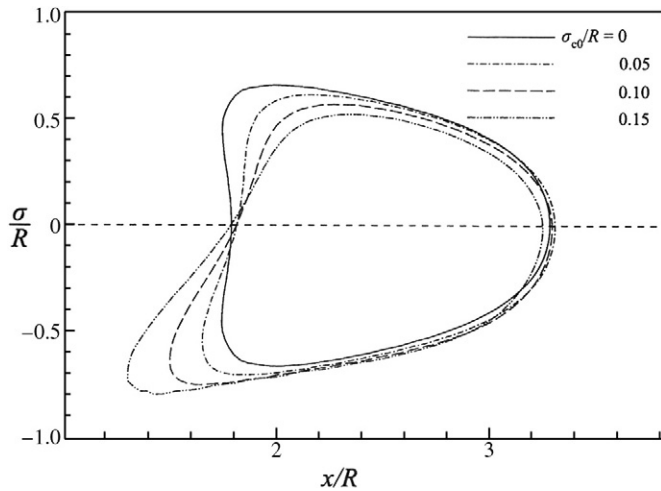


**Fig. 8.** Droplet shape at nondimensional time  $Vt/R=1.5$ , droplet spacing  $L/R=2$ ,  $k=0.7$ ,  $Ca=0.40$  for different initial distance from the centerline  $\sigma_{0c}/R=0, 0.05, 0.1$  and  $0.15$  [68].

stronger nonuniformity of the droplet distribution around the centerline. The experimental results are in qualitative agreement with predictions of the two-dimensional theory of Chan and Leal [63] (a quantitative comparison was hindered by data scatter and possible effects of contaminants on the interfacial tension). A good agreement is also found by comparing the experimental data with numerical simulations of Li and Pozrikidis [70], who took into account pairwise droplet interactions.

In the case of two-dimensional droplets Zhou and Pozrikidis [71] found that at  $\lambda=1$  droplet lateral migration was directed towards the centerline. At  $\lambda=10$  the direction of droplet migration was dependent on the initial position: droplets located close to the centerline moved to the wall, while the opposite was found for droplets initially placed close to the wall, thus showing the presence of an equilibrium position in between the centerline and the wall. Similar results were found by Mortazavi and Tryggvason [72] at small values of the Reynolds number based on droplet diameter. In particular, droplet migration to the centerline was found at  $\lambda=0.125$  and  $k$  (which in this case can be taken as equal to  $2R/H$ , where  $H$  is the distance between the plates) = 0.250. Furthermore, a small slip velocity with respect to the suspending fluid was observed in agreement with the predictions of Chan and Leal [63]. However, at  $\lambda=1$  the droplet migrated towards the wall, still in agreement with the theory of Chan and Leal [63] and with the experiments of Hiller and Kowaleski [69], but at variance with the simulations of Zhou and Pozrikidis [71]. The rate of migration increased with droplet deformation, as expressed by the capillary number. By increasing  $k$  to 0.750 and 0.875 a migration towards the centerline was found both at  $\lambda=0.125$  and 1. At higher values of the Reynolds number (in the range 5–50) the droplets either migrate to an equilibrium position located about halfway between the wall and the centerline or undergo oscillatory motion. The former behavior has been also observed for neutrally buoyant solid particles in Poiseuille flow in a range of  $Re$  and particle size, the so called Segre and Silberberg effect [73,74]. Three-dimensional sample calculations for  $Re=10$  confirm the behavior seen in planar Poiseuille flow.

The case of three-dimensional neutrally buoyant droplets in low Reynolds number Poiseuille flow between two parallel plates has been investigated by Griggs et al. [75] and by Davis and Zinchenko [51] by using boundary integral simulations. For nearly spherical droplets at low  $Ca$ , no migration across channel streamlines is observed. Droplets lag behind the suspending fluid, and this effect is more pronounced for larger values of  $R$ , closer distance to the walls

and larger  $\lambda$ . This finding is illustrated in Fig. 9, where the nondimensional translational velocity is plotted as a function of the position of the droplet center in the channel. At high values of  $\lambda$  (15 or greater) and small  $Ca$  the results for deformable droplets are in quite good agreement with those reported for rigid spheres [76]. As far as the lateral migration is concerned, the droplets tend to move towards the channel midplane, regardless of initial position, size, viscosity ratio and capillary number. This results is at variance with those of Mortazavi and Tryggvason [72], who found that at  $\lambda=1$  droplets migrated towards the walls, possibly due to the finite Reynolds numbers used in their calculations. On the other hand, droplet migration away from the walls is in agreement with the three-dimensional results of Coulliette and Pozrikidis [68] in a cylindrical tube and recent boundary integral calculations by Janssen and Anderson [77]. It should be noticed, however, that in the latter case droplets located at the centerline are axisymmetric, while the shape of droplets in a channel can be described as “heart-shaped”. Steady-state shapes at  $\lambda=1$ ,  $k=0.8$  and increasing values of  $Ca$  are shown in Fig. 10. The indentation on the rear is similar to the dimple observed in cylindrical tubes and becomes more pronounced at increasing capillary number until  $Ca\sim 1$ . For higher values of  $Ca$  no steady-state is found and breakup is likely to occur ( $Ca_{cr}\sim 1$  is in line with the value of 0.75 reported by Olbricht and Kung [16]). It should be noticed that steady-state may not be reached in industrial devices, so that transient behavior and the time scales for breakup are especially relevant for these applications.

### 3.2. Three-dimensional Poiseuille flow in rectangular channels

The flow behavior of droplets in rectangular channels of comparable or smaller size is relevant for microfluidics design, where the manipulation of fluids on the microscale has emerged as a promising approach in a number of applications [78]. Multiphase microfluidics has been the subject of several reviews concerning flow patterns, transport phenomena and chemical and materials syntheses (see for example [79]). Droplets can indeed be exploited as micro-reactors allowing one to process and handle small volumes of fluid with improved analytical performance, reduced instrumental footprints, low unit cost, and ultra-high throughput [80]. Here, we focus on fluid dynamical features of droplet motion in rectangular channels. Sarrazin et al. [81] used micro-particle image velocimetry (micro-PIV) and numerical simulations to study velocity fields inside droplets in a polydimethylsiloxane (PDMS) microchannel of width  $D=60\ \mu\text{m}$  and a constant height equal to  $0.83D$ . Viscosity and density ratio between the droplets and the continuous phase were 0.05 and 1.05, respectively. Droplet size was about  $150\times 50\times 40\ \mu\text{m}$  (length  $\times$  width  $\times$  height), and  $Ca=0.1$  and  $Re$  (based on an equivalent diameter of  $1.33D$ ) = 0.19. The velocity field was characterized by a central zone where flow is directed towards the front of the droplet and a thinner region close to the interface where fluid moves to the rear. Two toroidal recirculation zones are also apparent, which enhance mixing inside the droplet, as shown by numerical simulations. Recirculation zones at the front and the rear of the droplet act instead to inhibit mixing. Micro-PIV visualization of inner flow was carried out by Kinoshita et al. [82] by using a confocal microscope which allowed a high resolution optical sectioning in the vertical direction (about  $2\ \mu\text{m}$  vs  $5\ \mu\text{m}$  of the previously described technique). Channel width and height are  $100\ \mu\text{m}$  and  $58\ \mu\text{m}$ , respectively. The Reynolds number based on droplet size is  $3.0\cdot 10^{-3}$ , but it is not possible to calculate the capillary number since the interfacial tension is not given. By using the continuity equation, the vertical component of the velocity was calculated from the experimentally measured horizontal components, thus allowing a three-dimensional reconstruction of the flow field. The latter shows four zones of apparent contact between the water droplet and channel walls (such zones move backwards being dragged by the boundaries). A detailed picture of the flow field is shown in Fig. 11 in the four cross-sections corresponding to different focus positions

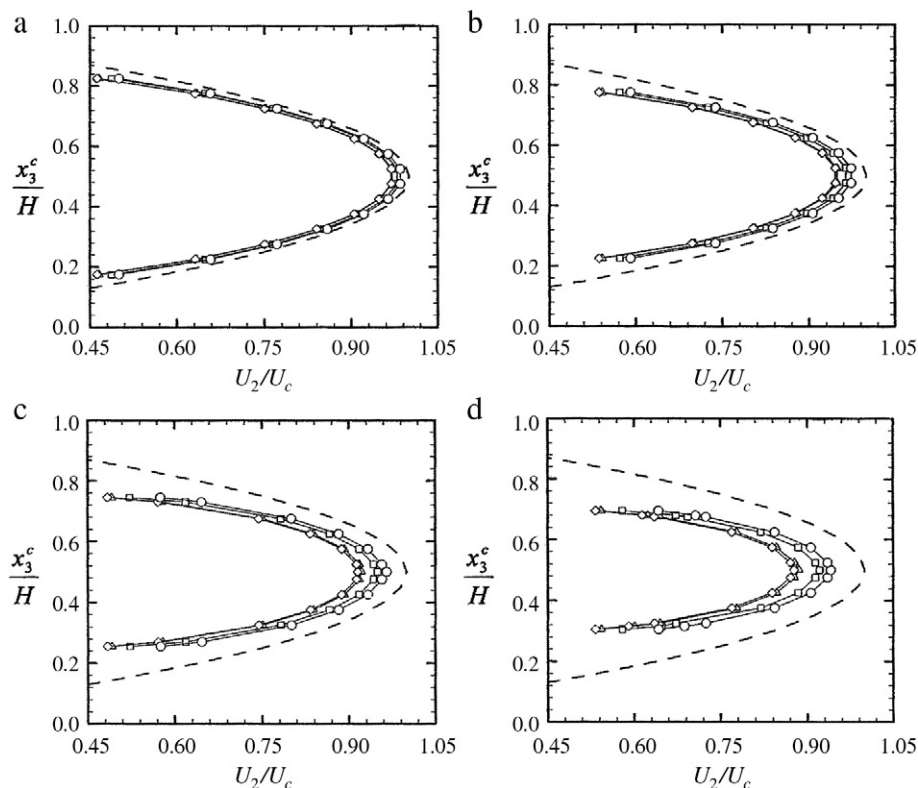


**Fig. 9.** Dimensionless translational velocities for spherical drops as a function of position of the droplet center in a rectangular channel, for  $k =$  (a) 0.3, (b) 0.4, (c) 0.5, and (d) 0.6, with viscosity ratios of (○) 0.5, (□) 1.0, (△) 5.0, and (◇) 10 (right to left). The undisturbed parabolic flow is shown by the dashed line [75].

along channel height. A complex flow pattern with three-dimensional vortices emerges from the velocity distributions of Fig. 11, with features similar to the ones calculated by Martinez and Udell [18] for a droplet flowing in a cylindrical tube (see Fig. 5).

The flow through a constriction, which has been discussed in Section 2.3, has been also studied in microfluidics devices. A possible application is rapid measurement of interfacial tension [83], which could be especially relevant for systems with very low values of  $\sigma$ , such as water-in-water mixtures [84], which are the subject of another review in this issue [85]. Quite recently, the hydrodynamic resistance of droplets in a rectangular microchannel has been investigated by measuring the excess pressure drop for a train of droplets [86] or for a single droplet by a microfluidics comparator [87]. In the latter work, several qualitative features, such as a lower resistance at high viscosity ratios, were found in agreement with the numerical simulations of Martinez and Udell [18] for tube flow. A model relating the excess pressure drop to dissipation caused by end caps in small droplets and by the central body in large droplets was also proposed. Other interesting aspects of multiphase flow in microchannels, such as droplet formation in T-junctions [88] or flow-focusing [89], are outside the scope of this review.

#### 4. Effects of surfactants in Poiseuille flow

It has been already pointed out that the presence of contaminants at the interface can lead to discrepancies between theoretical predictions and experimental results. Of course, surface-active agents can be added for practical purposes, especially as coalescence inhibitors in emulsion stabilization. Surfactants can be either soluble or insoluble in the bulk phase. In the former case, surfactants transport by diffusion and convection from the bulk to the droplet interface and adsorption–desorption mechanism need to be taken

into account. In addition, both convection due to the flow pattern at the interface (see Fig. 5) and surface diffusion act to change local surfactant concentration on droplet surface. Convection and diffusion at the droplet surface are the only mechanisms at play in case of insoluble surfactants, which are the most studied in the literature. Surfactant effects can be described in terms of three phenomena. The first one is surfactant accumulation at droplet tips due to surface convection, leading to a local decrease of surface tension and hence to higher local deformation. This effect is especially relevant for low viscosity ratios, where droplet breakup occurs by ejection of tiny fragments at the droplet tips (tip streaming [90]). The second effect is the onset of Marangoni stress due surface tension gradients. Marangoni stresses act tangentially opposite to the direction of surfactant convection and can lead to surface immobilization when they are balanced out by viscous stresses. This situation is similar to the case of high viscosity droplets, thus explaining why this effect is more pronounced at low viscosity ratios. Finally, the third effect is found at high surface coverage, when surface tension is essentially uniform due to high surfactant concentration. Surface enlargement upon droplet deformation brings about surfactant dilution. The resulting surface tension increase is associated with lower deformation as compared to a clean interface, regardless of the viscosity ratio.

The influence of surfactant adsorption on the steady axisymmetric translation of a spherical droplet in a tube under Poiseuille flow has been investigated by He et al. by numerical simulations [91]. Interfacial flow elicits surfactant convection from the front stagnation ring to the front pole and from the back pole to the back stagnation ring, thus leading to surface tension gradients and the corresponding Marangoni stresses. The assumptions of He et al. include fast desorption and diffusive processes, so that surfactants cannot accumulate at converging stagnation points, and surface concentration is only slightly different from the uniform value corresponding to

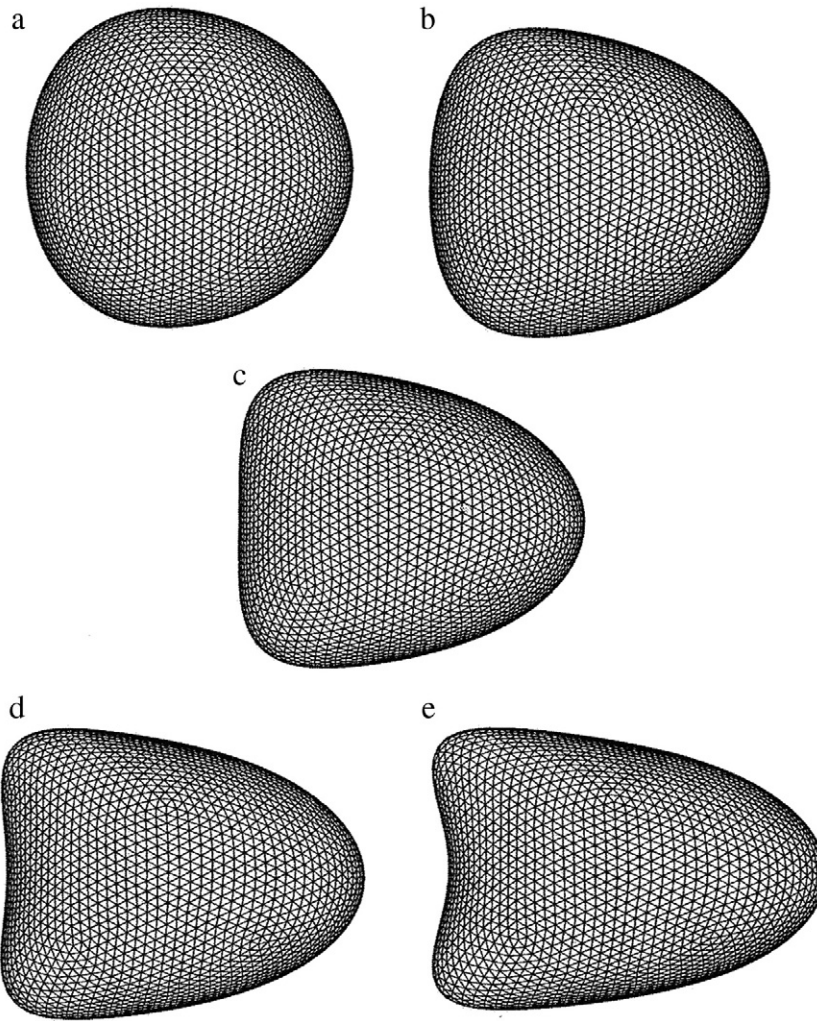


Fig. 10. Steady-state droplet shape at  $\lambda = 1$  and  $k = 0.8$  for  $Ca =$  (a) 0.1, (b) 0.3, (c) 0.5, (d) 0.7, and (e) 0.9 [75].

static conditions. The main results obtained by He et al. are that the surface convection pattern leads to a lower droplet velocity, and this retarding effect is higher for larger droplets and lower viscosity ratios.

The case of insoluble surfactants has been also addressed by Borhan and Mao [92], who used the boundary integral method in conjunction with a convective-diffusion equation to study surfactant distribution at the surface of the deformed droplet. Surfactant concentration was described by a linear equation of state, which is typically valid in the dilute regime. While droplet shape was slightly affected by the presence of a surfactant, more significant effects were found for the droplet velocity and the extra pressure drop. An important parameter in this problem is the Peclet number  $Pe$ , which expresses the ratio between surfactant convection and two-dimensional diffusion at the interface. At low values of  $Pe$  diffusion is dominant and surfactant distribution is almost constant. In this regime, the main effect of surfactant is to lower the surface tension. On the other hand, at high values of  $Pe$  convection-induced surfactant gradients elicit Marangoni stresses leading to surface immobilization. This results in higher extra pressure drops and lower droplet velocity as compared to clean interfaces, the effect becoming independent on  $\lambda$  at increasing values of  $Pe$ . If desorption is fast, and the bulk surfactant concentration is high enough so that diffusion away from the droplet is fast, then surfactant concentration is uniform and no significant Marangoni stresses are developed. This effect, leading to remobilization of surfactant-laden interfaces, has been demonstrated experimentally by Stebe et al. [93] for a three-phase periodic slug flow

in a capillary tube in which a train of alternating air and aqueous slugs ride on an annular wetting film of fluorocarbon oil. Surfactant, which is dissolved in the aqueous slug phase, adsorbs onto and retards the aqueous-oil interface, thus significantly increasing the pressure drop required to drive the slug train at constant velocity.

Recently, the effect of insoluble surfactants on equiviscous droplet deformation in Poiseuille flow between parallel plates has been investigated by Janssen and Anderson [94] by boundary integral numerical simulations. A Langmuir isotherm was used to model the surface tension  $\sigma$  as a function of surfactant concentration  $\Gamma$

$$\sigma = \frac{1 + E \ln(1 - x\Gamma)}{1 + E \ln(1 - \Gamma)} \quad (3)$$

where  $E$  is the elasticity parameter representing the sensitivity of  $\sigma$  with respect to  $\Gamma$ , and  $x = \Gamma_{eq}/\Gamma_{\infty}$  is the fraction of the surface initially covered by the surfactant,  $\Gamma_{\infty}$  being the maximum surfactant concentration. A Langmuir isotherm provides indeed a more realistic representation of the surfactant concentration as compared to a linear equation, especially at high values of  $\Gamma$ . Droplet deformation increases with surfactant coverage due to tip stretching up to  $x = 0.9$ . The trend is then reversed because of surfactant dilution. Furthermore, droplet velocity decreases with surfactant concentration. This result can be explained in terms of the immobilizing effect of Marangoni stresses at low concentrations and of surfactant dilution at higher values of  $\lambda$ . In

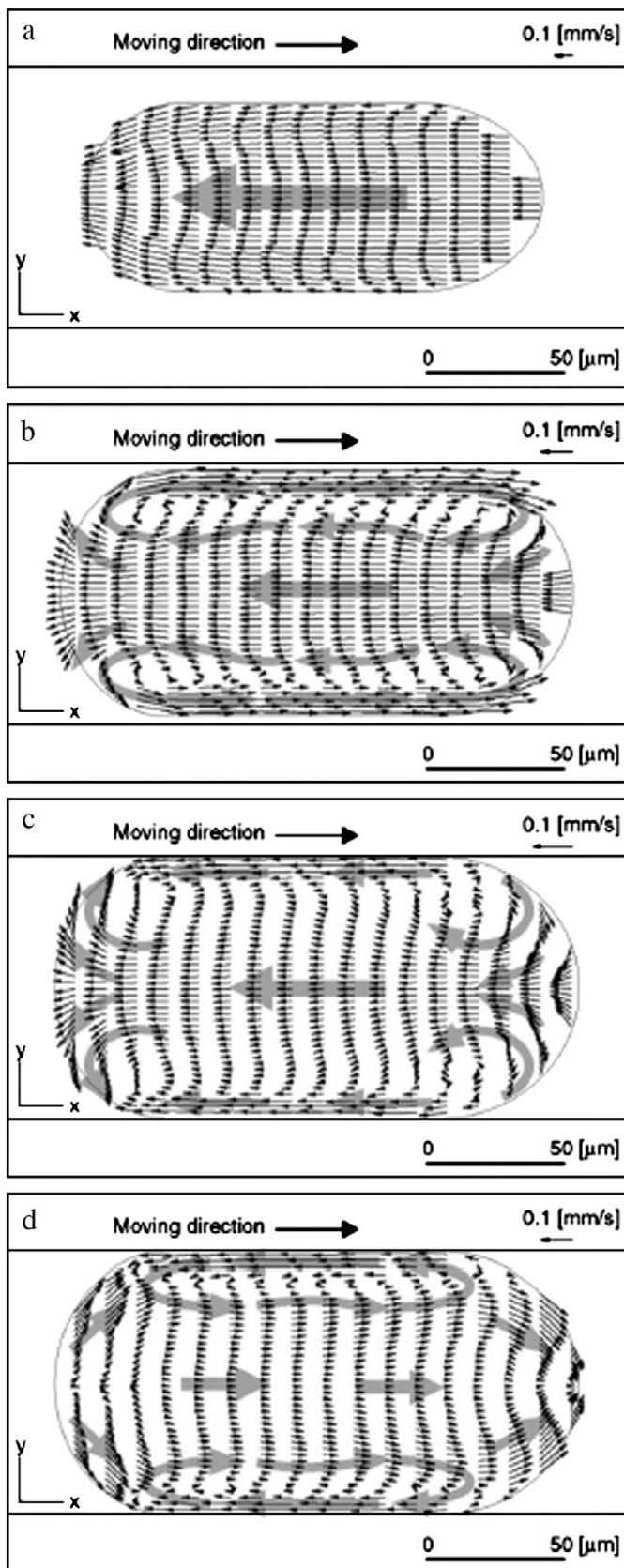


**Fig. 11.** 2D velocity distributions corresponding to four cross-sections at different focus positions. The droplet is moving from left to right. The arrows on the right with 0.1 mm/s represent the reference vectors. (a) 2.0  $\mu\text{m}$  away from the channel bottom wall. (b) 12.0  $\mu\text{m}$  away from the channel bottom wall. (c) 22.0  $\mu\text{m}$  from the channel bottom wall. (d) At the midplane cross-section of the droplet [82].

agreement with the results of Borhan and Mao [92], a lower droplet velocity was found at increasing values of  $Pe$ .

## 5. Conclusions

The deformation and breakup of single droplets in pressure-driven channel flow are subject of both scientific and industrial interests. In this review, the main fluid dynamical aspects reported in the literature concerning droplet flow behavior have been presented with reference to circular and rectangular cross-section channels. In fact, most of the quantities investigated in the literature show a similar behavior in the two channel geometries.

A topic of special interest is droplet breakup under Poiseuille flow, being it relevant for emulsification processes where the goal is to reduce the average droplet size by the action of flow. Experimental and numerical studies show that breakup is usually associated with the formation of a re-entrant jet of the continuous phase until droplet fragmentation occurs. Tip streaming is also found at low viscosity ratios.

Another interesting topic is droplet cross-stream migration, which can lead to nonuniform distribution of droplets in the channel. Both migrations towards the walls and the centerline have been found in experimental and numerical studies. However, the former ones could have been affected by the presence of contaminants at the droplet surface. In fact, the effect of surfactants has been the subject of several studies *per se*. Surfactants can indeed act to favor emulsification by lowering the interfacial tension and to stabilize the final products by inhibiting coalescence through Marangoni stresses. While several effects of surfactants on droplet flow behavior have been pointed out in the literature, this topic needs more work to be further elucidated.

This review has been mostly devoted to Newtonian fluids components, both in the droplet and in the suspending fluid. Some peculiar features on droplet cross-stream migration arising from the viscoelastic behavior of one of the fluids have been already cited [63,64]. Although other interesting works are available in the literature [95–100], further studies on non-Newtonian effects are at order.

Recently, droplet deformation and breakup in rectangular channels have attracted much interest in the context of microfluidics. More work in this area can be anticipated based on the range of potential applications, from process intensification to clinical testing. Since droplets can act as micro-reactors or carriers in microfluidics devices, a deeper knowledge of breakup conditions and internal circulation mixing patterns looks especially relevant for these applications.

## Acknowledgements

The authors gratefully acknowledge funding from the COST project “The Physics of droplets”.

## References

- [1] Taylor GI. Proc Roy Soc A 1932;138:41.
- [2] Taylor GI. Proc Roy Soc A 1934;146:501.
- [3] Tucker CL, Moldenaers P. Annu Rev Fluid Mech 2002;34:177.
- [4] Derkach SR. Adv Colloid Interface Sci 2009;151:1.
- [5] Rallison JM. Annu Rev Fluid Mech 1984;16:45.
- [6] Stone HA. Annu Rev Fluid Mech 1994;26:65.
- [7] Guido S, Greco F. Rheology Reviews British Society of Rheology; 2004. p. 99.
- [8] Windhab EJ, Dressler M, Feigl K, Fischer P, Megias-Alguacil D. Chem Eng Sci 2005;60:2101.
- [9] Olbricht WL. Annu Rev Fluid Mech 1996;28:187.
- [10] Van Puyvelde P, Vananroye A, Cardinaels R, Moldenaers P. Polymer 2008;49:5363.
- [11] Tomaiuolo G, Simeone M, Martinelli V, Rotoli B, Guido S. Soft Matter 2009;5:3736.
- [12] Cristini V, Kassab GS. Ann Biomed Eng 2005;33:1724.
- [13] Hetsroni G, Haber S. Rheol Acta 1970;9:488.
- [14] Brenner H, Bungay PM. Fed Proc 1971;30:1565.
- [15] Ho BP, Leal LG. J Fluid Mech 1975;71:361.

- [16] Olbricht WL, Kung DM. *Phys Fluids* 1992;4:1347.
- [17] Hyman WA, Skalak R. *AIChE* 1972;18:149.
- [18] Martinez MJ, Udell KS. *J Fluid Mech* 1990;210:565.
- [19] Goldsmith HL, Mason SG. *J Colloid Sci* 1963;18:237.
- [20] Olbricht WL, Leal LG. *J Fluid Mech* 1982;115:187.
- [21] Borhan A, Pallinti J. *Ind Eng Chem Res* 1998;37:3748.
- [22] Hadamard J. *C R Acad Sci* 1911;152:1735.
- [23] Pozrikidis C. *J Fluid Mech* 1992;237:627.
- [24] Hemmat M, Borhan A. *Chem Eng Comm* 1996;148–150:363.
- [25] Taha T, Cui ZF. *Chem Eng Sci* 2004;59:1181.
- [26] Sheng P, Zhou M. *Phys Rev A* 1992;45:5694.
- [27] Bretherton FP. *J Fluid Mech* 1961;10:166.
- [28] Hodges SR, Jensen OE, Rallison JM. *J Fluid Mech* 2004;501:279.
- [29] Reinelt DA, Saffman PG. *Soc Ind Appl Math* 1985;6:542.
- [30] Fairbrother F, Stubbs AE. *J Chem Soc* 1935:527.
- [31] Taylor GI. *J Fluid Mech* 1961;10:161.
- [32] Cox BG. *J Fluid Mech* 1964;20:193.
- [33] Schwartz LW, Princen HM, Kiss AD. *J Fluid Mech* 1986;172:259.
- [34] Dong M, Fan Q, Dai L. *Transp Porous Med* 2009;1.
- [35] Ratulowski J, Chang HC. *J Fluid Mech* 1990;210:303.
- [36] Ginley GM, Radke CJ. *Am Chem Soc Div Petrol Chem*, 1 ed; 1988. p. 4.
- [37] Denkov ND, Subramanian V, Gurovich D, Lips A. *Colloids Surf A* 2005;263:129.
- [38] Denkov ND, Tcholakova S, Golemanov K, Subramanian V, Lips A. *Colloids Surf A* 2006;282–283:329.
- [39] Torza S, Cox RG, Mason SG. *J Colloid Interface Sci* 1972;38:395.
- [40] Cristini V, Guido S, Alfani A, Blawdziewicz J, Loewenberg M. *J Rheol* 2003;47:1283.
- [41] Sibillo V, Pasquariello G, Simeone M, Cristini V, Guido S. *Phys Rev Letters* 2006;97:054502–1.
- [42] Vananroye A, Van Puyvelde P, Moldenaers P. *Langmuir* 2006;22:3972.
- [43] B. Chi. The motion of immiscible drops and the stability of anular flow. PhD thesis, (1986).
- [44] Tsai TM, Miksis MJ. *J Fluid Mech* 1994;274:197.
- [45] Olbricht WL, Leal LG. *J Fluid Mech* 1983;134:329.
- [46] Martinez MJ, Udell KS. *AIP Conf Proc* 1988:222.
- [47] Cobos S, Carvalho MS, Alvarado V. *Int J Multiphase Flow* 2009;35:507.
- [48] Peña TJ, Carvalho MS, Alvarado V. *AIChE Journal* 2009;55:1993.
- [49] Graham DR, Higdon JLL. *J Fluid Mech* 2000;425:31.
- [50] Graham DR, Higdon JLL. *J Fluid Mech* 2000;425:55.
- [51] Davis RH, Zinchenko AZ. *J Colloid Interface Sci* 2009;334:113.
- [52] Karami A, Balke ST. *Polymer Eng Sci* 2000;40:2342.
- [53] Goldsmith HL, Mason SG. *Nature* 1961;190:1095.
- [54] Goldsmith HL, Mason SG. *J Colloid Interface Sci* 1962;17:448.
- [55] Karnis A, Goldsmith HL, Mason SG. *Nature* 1963;200:159.
- [56] Karnis A, Mason SG. *J Colloid Interface Sci* 1967;24:164.
- [57] Brenner H. *Adv Chem Eng* 1966;6:151.
- [58] Takano M, Goldsmith HL, Mason SG. *J Colloid Interface Sci* 1968;27:253.
- [59] Chaffey CE, Brenner H, Mason SG. *Rheol Acta* 1965;4:64.
- [60] Chaffey CE, Brenner H, Mason SG. *Rheol Acta* 1967;6:100.
- [61] Haber S, Hetsroni G. *J Fluid Mech* 1971;49:257.
- [62] Wohl PR, Rubinow SI. *J Fluid Mech* 1974;62:185.
- [63] Chan PCH, Leal LG. *J Fluid Mech* 1979;92:131.
- [64] Gauthier F, Goldsmith HL, Mason SG. *J Rheol* 1971;15:297.
- [65] Uijttewaal WSJ, Nijhof E-J, Heethaar RM. *Phys Fluids* 1993;5:819.
- [66] Kennedy MR, Pozrikidis C, Skalak R. *Comput Fluid* 1994;23:251.
- [67] Uijttewaal WSJ, Nijhof EJ. *J Fluid Mech* 1995;302:45.
- [68] Couliette C, Pozrikidis C. *J Fluid Mech* 1998;358:1.
- [69] Hiller W, Kowalewski TA. *Exp Fluids* 1987;5:43.
- [70] Li X, Pozrikidis C. *Int J Multiphase Flow* 2000;26:1247.
- [71] Zhou H, Pozrikidis C. *Phys Fluids* 1994;6:80.
- [72] Mortazavi S, Tryggvason GR. *J Fluid Mech* 2000;411:325.
- [73] Segré G, Silberberg A. *J Fluid Mech* 1962;14:115.
- [74] Segré G, Silberberg A. *J Fluid Mech* 1962;14:136.
- [75] Griggs AJ, Zinchenko AZ, Davis RH. *Int J Multiphase Flow* 2007;33:182.
- [76] Staben ME, Zinchenko AZ, Davis RH. *Phys Fluids* 2003;15:1711.
- [77] Janssen PJA, Anderson PD. *J Comput Phys* 2008;227:8807.
- [78] Whitesides GM. *Nature* 2006;442:368.
- [79] Günther A, Jensen KF. *Lab Chip* 2006;6:1487.
- [80] Huebner A, Sharma S, Srisa-Art M, Hollfelder F, Edel JB. A. J. deMello. *Lab Chip* 2008;8:1244.
- [81] Sarrazin F, Loubiere K, Prat L, Gourdon C, Bonometti T, Magoaudet J. *AIChE* 2006;52:4061.
- [82] Kinoshita H, Kaneda S, Fujii T, Oshima M. *Lab Chip* 2007;7:338.
- [83] Cabral JT, Hudson SD. *Lab Chip* 2006;6:427.
- [84] Guido S, Simeone M, Alfani A. *Carbohydrate Polymers* 2002;48:143.
- [85] Frith WJ. *Adv Colloid Interface Sci* 2009:1.
- [86] Adzima BJ, Velankar SS. *J Micromech Microeng* 2006;16:1504.
- [87] Vanapalli SA, Banpurkar AG, Van Den Ende D, Duits MHG, Mugele F. *Lab Chip* 2009;9:982.
- [88] Link DR, Anna SL, Weitz DA, Stone HA. *Phys Rev Lett* 2004;92:054503.
- [89] T. Ward, M. Faivre, M. Abkarian, H.A. Stone, 26 (2005) 3716.
- [90] Eggleton CD, Tsai T-M, Stebe KJ. *Phys Rev Lett* 2001;87:048302–1.
- [91] He Z, Dagan Z, Maldarelli C. *J Fluid Mech* 1991;222:1.
- [92] Borhan A, Mao CF. *Phys Fluids* 1992;4:2628.
- [93] Stebe KJ, Lin S-Y, Maldarelli C. *Phys Fluids A* 1991:3.
- [94] Janssen PJA, Anderson PD. *Chem Eng Res Des* 2008;86:8807.
- [95] Dressler M, Edwards BJ. *J Non-Newtonian Fluid Mech* 2005;130:77.
- [96] Chin HB, Han CD. *J Rheol* 1980;24:1.
- [97] Kim SJ, Han CD. *J Rheol* 2001;45:1279.
- [98] Nadim A, Borhan A. *Appl Math Res Express* 2006;2006:1.
- [99] Harvie DJE, Cooper-White JJ, Davidson MR. *J Non-Newtonian Fluid Mech* 2008;155:67.
- [100] Lavrenteva OM, Holenberg Y, Nir A. *Chem Eng Sci* 2009;64:4772.

# Microfluidics analysis of red blood cell membrane viscoelasticity

Giovanna Tomaiuolo,<sup>ab</sup> Mario Barra,<sup>c</sup> Valentina Preziosi,<sup>a</sup> Antonio Cassinese,<sup>c</sup> Bruno Rotoli<sup>d</sup> and Stefano Guido<sup>\*ab</sup>

Received 27th August 2010, Accepted 19th October 2010

DOI: 10.1039/c0lc00348d

In this work, a microfluidic system to investigate the flow behavior of red blood cells in a microcirculation-mimicking network of PDMS microchannels with thickness comparable to cell size is presented. We provide the first quantitative description of cell velocity and shape as a function of the applied pressure drop in such devices. Based on these results, a novel methodology to measure cell membrane viscoelastic properties in converging/diverging flow is developed, and the results are in good agreement with data from the literature. In particular, in the diverging channel the effect of RBC surface viscosity is dominant with respect to shear elasticity. Possible applications include measurements of cell deformability in pathological samples, where reliable methods are still lacking.

## Introduction

In microcirculation *in vivo*, red blood cells (RBCs) travel through microvessels with diameter smaller than cell size in order to ensure optimal gas transfer between blood and tissues.<sup>1</sup> In such microconfined flow RBC shape departs from the classical biconcave geometry at rest by taking more fluid dynamic configurations depending on flow rate and microvessel diameter.<sup>2</sup> The high RBC deformability is mainly due to the viscoelastic properties of the cell membrane, especially shear modulus and surface viscosity.<sup>3</sup> Bending resistance is small unless high curvatures are involved,<sup>4</sup> such as in going from biconcave to parachute shapes<sup>5,6</sup> and in slipper-like shapes.<sup>7</sup> An altered RBC deformability is associated with several diseases, such as diabetes, sickle cell anemia and spherocytosis.<sup>1,2</sup> Due to the pathophysiological relevance of RBC deformability, a number of studies on this topic are reported in the literature.<sup>8</sup> The available experimental methods include single cell techniques, such as micropipette aspiration<sup>9–11</sup> and optical tweezers,<sup>12–14</sup> and measurements on whole blood or diluted RBC suspensions, such as blood filtration<sup>15</sup> and ektacytometry.<sup>16</sup> The main drawback of the former techniques is the limited number of cells that can be tested at the same time, thus hindering the acquisition of statistically significant datasets. As far as the whole blood techniques are concerned, the imposed flow geometry is far from the ones actually experienced by RBCs in microcirculation, which makes more difficult to evaluate the clinical relevance of the results.

Recently, microfluidic techniques have been applied to design flow geometries resembling the microvascular network.<sup>17</sup> In principle, microfluidic devices are suitable to testing a large number of cells in a physiologically relevant flow field.<sup>18</sup> By using transparent substrata, such as polydimethylsiloxane (PDMS)

and glass, the flow behavior of individual cells has been investigated by video microscopy. Examples from the literature are measurement of cell deformation in healthy donors<sup>19</sup> and diabetes patients,<sup>20</sup> effect of microconfined flow in malaria,<sup>21</sup> flow-induced RBC filtration,<sup>22</sup> determination of pressure drop through a single cell,<sup>23</sup> and measurement of cell size under flow.<sup>24–26</sup> However, to our knowledge microfluidic devices to determine the viscoelastic properties of RBC membrane are still lacking.

In this work, we report on the setup and the quantitative fluid dynamic analysis of a microfluidics device with channel thickness comparable to RBC size. By studying cell deformation in a divergent channel geometry, membrane viscoelastic properties are obtained from the application of the classical Kelvin–Voigt model, which is based on the parallel combination of an elastic spring and a Newtonian damping element.

## Methodology

### Device fabrication

The microfluidic device is made of PDMS and is fabricated by using soft-lithography techniques with SU-8 as photoresist. The network pattern (Fig. 1) used as a stamp was drawn by a layout program, LASI 7, a commercial software widely used to draw electric microcircuits, and consists of a network of bifurcating

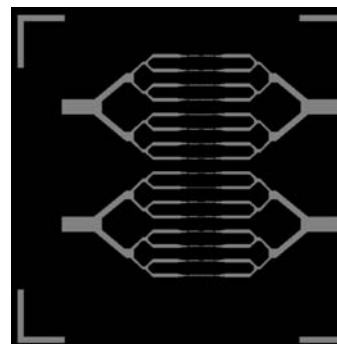


Fig. 1 The geometry used in the microfluidic device.

<sup>a</sup>Dipartimento di Ingegneria chimica, Università di Napoli Federico II, Napoli, Italy. E-mail: steguido@unina.it; Fax: +39 081-2391800; Tel: +39 081-7682271

<sup>b</sup>CEINGE-Advanced Biotechnologies, Napoli, Italy

<sup>c</sup>CNR-SPIN and Department of Physics Science, Università di Napoli Federico II, Napoli, Italy. E-mail: antonio.cassinese@unina.it; Fax: +39 081-2391821; Tel: +39 081-7682548

<sup>d</sup>Dipartimento di Biochimica e Biotecnologie mediche, Università di Napoli Federico II, Napoli, Italy

channels of decreasing width (down to 10 micron), including converging–diverging flow sections, to mimic human microcirculation network.

The PDMS microchannels are bonded to a glass cover slip by a Corona-treater and the final channel thickness is about 7.5 micron as measured by profilometry.

### Experimental setup

Observations are performed through a 100× oil immersion objective by using an optical microscope (Zeiss Axiovert 100) equipped with a motorized translating stage and a focus control (Ludl), and a high speed video camera (Phantom 4.3) operated up to 1000 frames per second (Fig. 2). Venous blood samples are withdrawn from healthy consenting volunteers and used within 4 hours of collection. RBC suspensions used in the experiments are obtained by diluting blood samples 1 : 100 with human albumin supplemented ACD anticoagulant (0.6% citric acid, 1.1% anhydrous dextrose, 2.3% sodium citrate, 96% water). The total pressure drop  $\Delta P_{\text{tot}}$  in the microchannel network is adjusted by changing the distance between a feeding and an exit reservoir connected through plastic tubing to the microfluidics device.

### Image acquisition and data analysis

At each pressure drop, a sequence of images (around 10 000) captured by the high speed video camera is recorded on a hard disk. Given the large amount of images to be analyzed, a macro based on the library of a commercial package (Image Pro Plus) has been developed for automated image processing. The output data include RBC center of mass coordinates, velocity and deformation index, DI, defined as the ratio between the sides of a bounding rectangular box enclosing cell contour. Only axisymmetrical RBCs are considered in the following for the sake of comparison with models and experimental data from the literature. The values of pressure drop  $\Delta P_j$  in each channel of the

network are found by calculation since in our experiments only the total pressure drop  $\Delta P_{\text{tot}}$  across the whole microfluidic device is directly known, being imposed as the liquid head between the two reservoirs. In order to calculate  $\Delta P_j$ , the following Poiseuille-type expression of the flow rate  $Q_j$  for a rectangular cross-section channel<sup>27</sup> was used where, once again, the index  $j$  refers to a generic channel in the network pattern shown in Fig. 1 and the coordinate system used to describe the flow field and the channel geometry is shown in Fig. 3.

$$Q_j = \frac{W_j H^3}{12\mu} \left( \frac{\Delta P_j}{L_j} \right) \left[ 1 - \frac{192H}{\pi^5 W_j} \sum_{i=1,3,\dots}^{\infty} \frac{1}{i^5} \tan h \left( \frac{i\pi W_j}{2H} \right) \right] \quad (1)$$

The term  $\frac{W_j H^3}{12\mu} \left( \frac{\Delta P_j}{L_j} \right)$  in eqn (1) is the flow rate in a slit and the term between square brackets is the correction for a finite width channel. The overall flow rate  $Q$  is found by imposing that the overall applied pressure drop  $\Delta P_{\text{tot}}$  is equal to the sum of the pressure drops in each channel as calculated from eqn (1). This leads to the following expression for  $Q$  according to the splitting geometry shown in Fig. 1:

$$Q = \frac{\Delta P}{\sum_j \frac{12\mu L_j}{W_j H^3} \left[ 1 - \frac{192H}{\pi^5 W_j} \sum_{i=1,3,\dots}^{\infty} \frac{1}{i^5} \tan h \left( \frac{i\pi W_j}{2H} \right) \right]^{-1}} \quad (2)$$

This calculation scheme is based on the assumptions that (i) the pressure drops associated with changes in channel direction are negligible with respect to the distributed ones appearing in eqn (1) (this can be confirmed by simple estimates, not shown here for the sake of brevity), and (ii) the contribution of the flowing RBCs to the pressure drop is negligible in the dilute regime investigated in this work (see Secomb *et al.*<sup>4</sup>), (iii) for the same reason, *i.e.*, the high blood dilution, coupled with some bypass around the PDMS chip in the flow cell, the effects of white blood cells, which are 3 orders of magnitude less abundant than RBCs, are negligible as well, and (iv) the dilute blood suspension behaves like a Newtonian liquid. This latter point was confirmed by viscosity measurements performed on glass capillaries, which give a constant value of  $\mu = 1.05$  cP independent of wall shear rate.

## Results

### Constant cross-section channel

We start describing the experimental results from the data obtained in channels having constant cross-section. An example

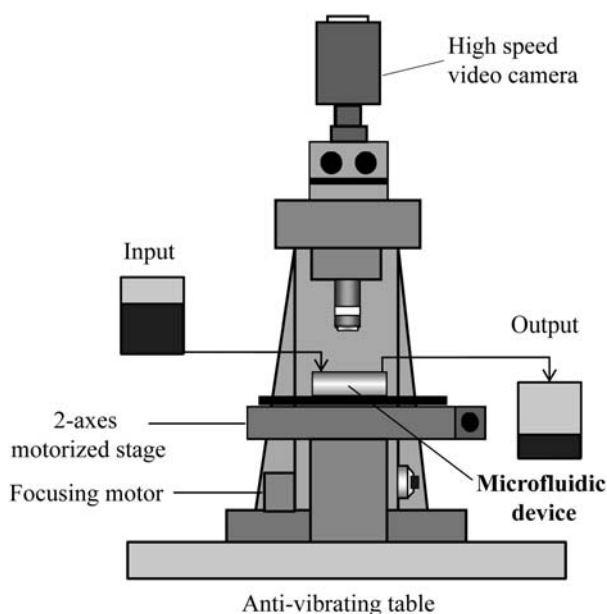


Fig. 2 Schematic of the experimental setup.

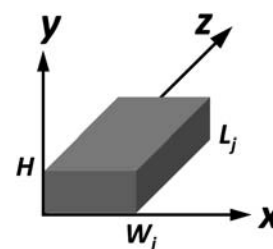
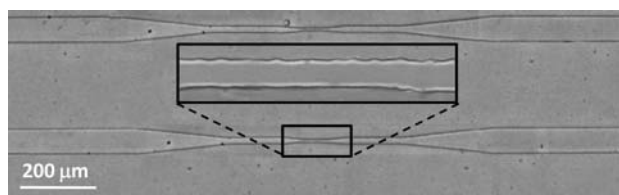


Fig. 3 The coordinate system used to describe the flow field.



**Fig. 4** The straight channel ( $W = 10$  micron) selected to analyze RBC motion in a constant cross-section channel.

is presented in Fig. 4, where the enlargement shows the smallest straight channel (width = 10 micron), which has been used to investigate RBC flow behavior.

The data of RBC velocity as a function of the local pressure drop between the ends of the smallest straight channel,  $\Delta P/L$ , are shown in Fig. 5.

In the same plot data of RBC velocity vs.  $\Delta P/L$  in circular cross-section microcapillaries of 10 micron inner diameter (which have a cross-section area comparable to that of the rectangular microchannels) are also shown for comparison. It can be noticed that the two sets of data are close to each other, thus showing that the flow behavior of RBCs is similar in the two geometries. This result shows that the effect of the gutters (the regions of the flow field bounded by the curved cell body and the corners of the channel) is not significant for RBCs under confined flow. The effect of the gutters has been found to be important in the case of bubbles flowing in rectangular channels at an intermediate surfactant concentration.<sup>28</sup> A more detailed investigation of this effect in RBCs is outside the scope of this work. Here, it should be noticed that the similarity of RBC flow behavior in rectangular and circular channels provides further support to the use of microfluidics as a relevant experimental model of microcirculation.

Representative images of RBCs flowing in the smallest straight channel are shown in Fig. 6a at two cell velocities. In both cases, cell shapes are deformed with respect to the biconcave rest configuration, being more elongated at increasing cell velocity. As a reference, images of RBCs flowing in circular cross-section

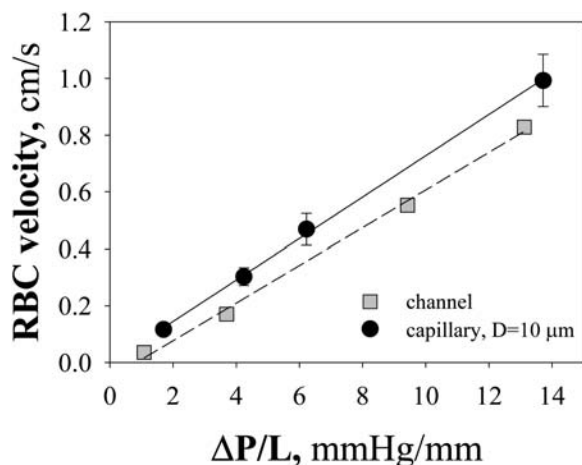


**Fig. 5** RBC velocity vs. pressure drop per unit length in the straight channel and in a capillary of comparable size ( $D = 10 \mu\text{m}$ ).

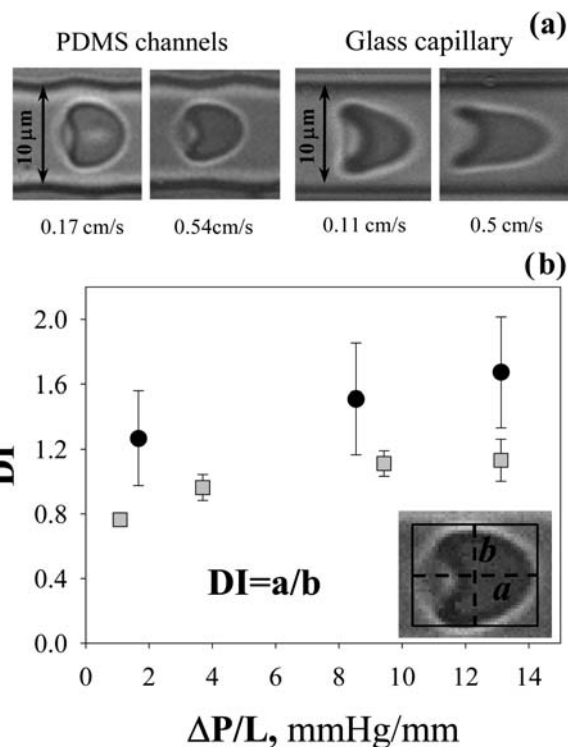


**Fig. 6** (a) Representative images of RBCs flowing in rectangular (left) and circular (right) microchannels at a comparable cell velocity. (b) The deformation index, DI, vs.  $\Delta P/L$  of RBCs flowing in channels (squares) and capillaries (circles) of comparable size.

glass microcapillaries of 10 micron diameter are also shown in the same figure.<sup>29</sup>

In both geometries, RBCs exhibit the typical parachute-like shape found in microcirculation *in vivo*. However, in the PDMS rectangular channels RBCs display a more flattened shape and are more elongated in the  $x$ -axis due to the channel aspect ratio ( $=10/7.5$ ). This trend is shown in a quantitative way in Fig. 6b, where the deformation index, DI, defined as the ratio between the sides of a cell rectangular bounding box (see inset), is plotted as a function of  $\Delta P/L$ . Indeed, at any value of  $\Delta P/L$  the deformation index is slightly smaller in the rectangular channels than in the circular cross-section capillaries. In both cases, DI tends to increase with pressure drop and cell velocity. In the rectangular channels the values of DI are smaller than 1 at low  $\Delta P/L$ , again as expected based on the shapes shown in Fig. 6a.

### Divergent channel

In order to measure the viscoelastic properties of the RBC membrane, which are the main factors affecting cell deformability,<sup>30</sup> the flow in the channel region shown in Fig. 7a was investigated. Such region may be divided into three zones: (1) a constant cross-section with  $W_I = 10 \mu\text{m}$  and  $L_I = 25 \mu\text{m}$ ; (2) a diverging cross-section, with  $W_{II}$  ranging from  $10 \mu\text{m}$  to  $25 \mu\text{m}$  and  $L_{II} = 100 \mu\text{m}$ ; (3) a constant cross-section with  $W_{III} = 25 \mu\text{m}$  and  $L_{III} = 65 \mu\text{m}$ . The three zones are marked with dashed lines in Fig. 7a. In Fig. 7b RBC velocity is plotted as a function of distance  $z$  along the divergent channel centerline at three different pressure drops.

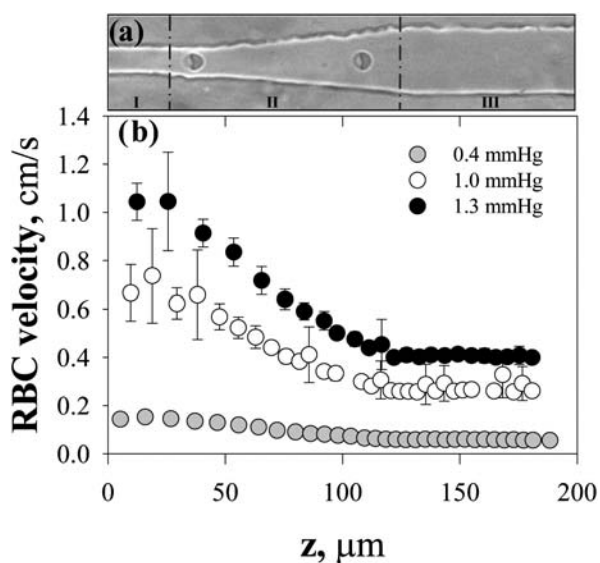


**Fig. 7** (a) An image of the channel region used to estimate RBC membrane viscoelastic properties. (b) RBC velocity as a function of  $z$  in the same channel region.

The  $z$  origin is located halfway in the smallest straight channel. Error bars represent the data standard deviation. Only RBCs with a center of mass moving on the centerline (with a tolerance  $\pm 0.3 \mu\text{m}$ ) and thus exhibiting an apparently axisymmetrical shape are considered in this analysis, as shown in the upper image. As expected, RBC velocity decreases with channel width at the same pressure drop and increases with  $\Delta P$  at any values of  $z$ .

For a cell travelling along the centerline, the fluid dynamic action in the divergent channel can be described as a uniaxial compressional stress  $\sigma = 3\eta_s \dot{\epsilon}$ , where  $\eta_s$  is the suspending fluid viscosity (1.05 cP) and  $\dot{\epsilon}$  is the strain rate.<sup>31</sup> The latter is equal to the velocity gradient  $d v/d z$  at the centerline.<sup>32</sup> In turn, the fluid velocity  $v$  at the centerline as a function of  $z$  is calculated by dividing eqn (1) by the local cross-section area  $A$  in the divergent (which also depends on  $z$  as  $A = W_{II} H = (W_I + z \tan \alpha) H$ , where  $\alpha$  is the divergent angle equal to  $5^\circ$ ). The calculated velocity gradient as a function of  $z$  is shown in Fig. 8 at two extreme

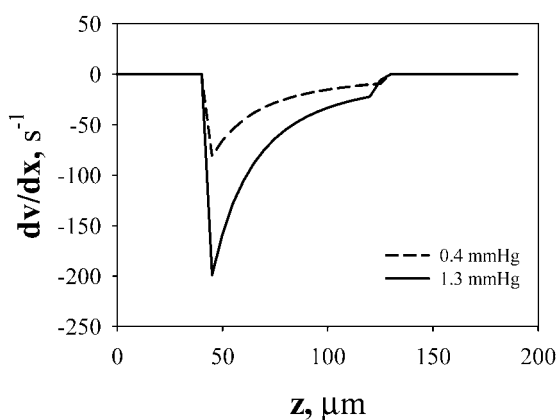


**Fig. 8** The calculated velocity gradient as a function of  $z$  at two different pressure drops.

values of pressure drop of Fig. 7 (the third one being omitted for the sake of clarity). It can be seen that  $d v/d z$  starts from zero in the smaller straight channel, takes a negative minimum and tends to zero again at the larger constant section channel. The extensional stress is then negative in the diverging section, thus corresponding to uniaxial compression, which is the external force acting on the flowing RBCs. Concerning RBC shape, starting from a more elongated configuration in the  $10 \mu\text{m}$  straight channel, a progressive rounding up of the cell body is observed along the divergent length.

A quantitative representation of this behavior can be obtained by plotting the deformation index, DI, as a function of the  $z$  coordinate in the divergent channel, as shown in Fig. 9 at the same pressure drops as in Fig. 8.

The deformation index is indeed a decreasing function of  $z$ , due to the more rounded shapes as RBCs approach the divergent end. A similar trend is observed in the classical micropipette experiment, where the retraction of a deformed cell vs. time is measured after ejection from the capillary.<sup>9,30,33</sup> In our case, the shape change of the RBCs flowing in the divergent channel is elicited by the fluid dynamics of the flow field.

The RBC flow-induced deformation in the divergent channel can be described by using the Kelvin–Voigt model,<sup>30</sup> which is based on the parallel combination of a spring and a dashpot. The two elements are associated with the elastic and viscous response of the cell membrane, respectively. The elastic part is expressed by a shear modulus  $\mu$ , and the viscous one by a surface viscosity  $\eta$ . We used the following expression of the constitutive equation of the Kelvin–Voigt model:

$$T = \frac{\mu}{2} \left[ \left( \frac{\lambda}{\lambda_{\text{fin}}} \right)^2 - \left( \frac{\lambda}{\lambda_{\text{fin}}} \right)^{-2} \right] + \frac{2\eta}{\lambda} \frac{\partial \lambda}{\partial t} \quad (3)$$

where  $T$  is the tension (force/length, see below) acting on the membrane due to the flow field, and  $\lambda$  is the membrane deformation given by the ratio between the initial and the deformed length  $a$  of the cell body (see inset of Fig. 6b) in the  $z$  direction.  $\lambda_{\text{fin}}$  is the value of  $\lambda$  at the end of the divergent channel, and it was found by solving eqn (3) with  $\partial \lambda / \partial t = 0$  and  $\dot{\epsilon}$  calculated at the end of the divergent. The membrane tension  $T$  is given by

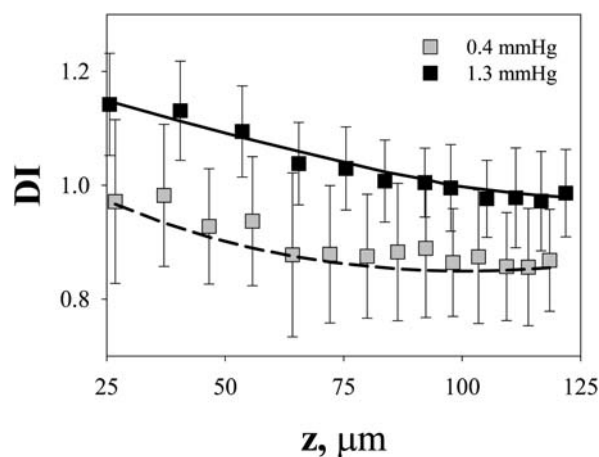


**Fig. 9** The deformation index vs  $z$  in the divergent channel at two pressure drops. Lines are obtained by best-fitting the Kelvin–Voigt model.

$\sigma A_{\text{RBC}}/L_{\text{RBC}}$ , where  $\sigma$  is the flow-generated uniaxial compressional stress acting on RBC membrane,  $A_{\text{RBC}}$  is the cell area ( $=135 \mu\text{m}^2$ ) and  $L_{\text{RBC}}$  is the cell diameter at rest ( $=8 \mu\text{m}$ ). Eqn (3) was solved by numerical integration for  $\lambda$  and the model parameters  $\mu$  and  $\eta$  were varied in order to give the best fit of the experimental values of DI in Fig. 9. Indeed, the deformation index is given by the ratio of membrane deformation along the  $z$  direction,  $\lambda$ , and membrane deformation along the  $x$  direction, which, due to volume conservation, is given by  $1/\lambda$ . Hence, the deformation index, DI, is equal to  $\lambda^2$ .<sup>30</sup> The best fitting procedure was applied to both datasets of Fig. 9 corresponding to two different values of the pressure drop, and the so obtained values of the model parameters  $\mu$  and  $\eta$  are  $0.006 \text{ dyn cm}^{-1}$  and  $0.055 \text{ cP}\cdot\text{cm}$ , respectively. These values are in good agreement with experimental results from the literature ( $0.006\text{--}0.009$  for  $\mu$ , and  $0.047\text{--}0.1$  for  $\eta$ ).<sup>2,34–36</sup> The lines in Fig. 9 are the Kelvin–Voigt model predictions based on our fitting parameters, and a good agreement is found.

In order to get more insight into the RBC membrane visco-elastic behavior each term of eqn (3) is plotted vs. time in Fig. 10, where  $T$  is the membrane tension coming from the external flow field,  $T_s^v = \frac{2\eta}{\lambda} \frac{\partial \lambda}{\partial t}$  is the membrane tension associated with the surface viscosity and  $T_s^e = \frac{\mu}{2} \left[ \left( \frac{\lambda}{\lambda_{\text{fin}}} \right)^2 - \left( \frac{\lambda}{\lambda_{\text{fin}}} \right)^{-2} \right]$  is the tension due to shear elasticity.

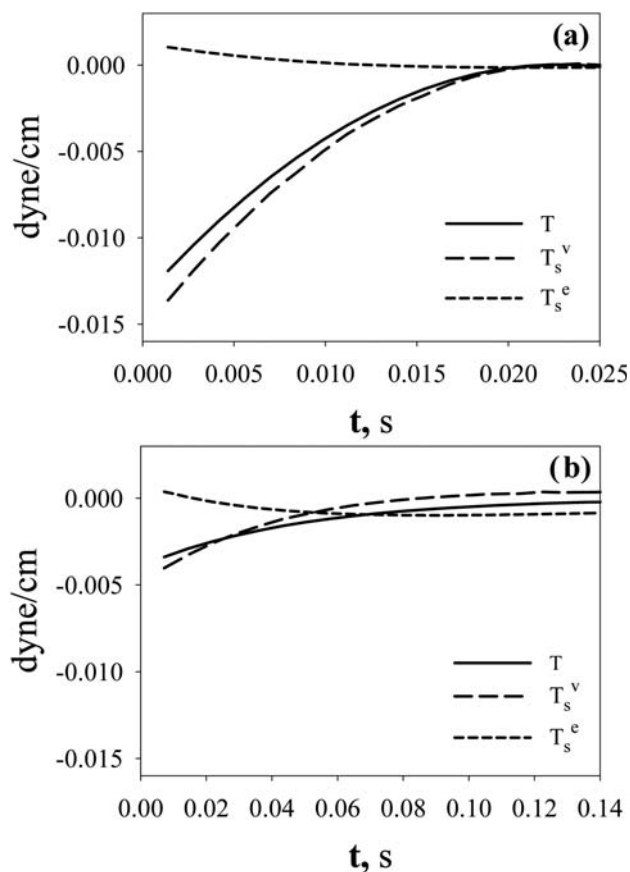


**Fig. 10** The three contributes of the tension in the equation of Kelvin–Voigt model at (a) 1.3 mmHg and (b) 0.4 mmHg.

Fig. 10a and b refer to a pressure drop of 1.3 mmHg and 0.4 mmHg, respectively. At both pressure drops the viscous tension is dominant as compared to the elastic one, and this effect increases with pressure drop. In other words, mechanical RBC membrane behavior is mostly governed by the viscous component in the diverging channel. On the contrary, elasticity is dominant in the constant section zones, where viscosity contribution can be considered negligible due to the lack of membrane rotation in axisymmetrical cells.<sup>4</sup> These findings are in line with predictions of Secomb and Hsu<sup>37</sup> for RBC motion through cylindrical micropores based on a time-dependent lubrication equation for the suspending fluid coupled with equations for membrane equilibrium. It can also be noticed that the RBC transit time through the diverging channel at the pressure drop of 0.4 mmHg ( $\sim 0.15$  s) is comparable to RBC characteristic relaxation time, which can be estimated as  $\eta/\mu = 0.09$  s. On the other hand, at the higher pressure drop of 1.3 mmHg the RBC transit time is an order of magnitude lower than the relaxation time. Thus, such higher values of pressure drop are best suited to measure RBC surface viscosity.

## Conclusions

In conclusion, in this work a microfluidics system to investigate RBC flow in a microcirculation-mimicking network of PDMS microchannels with thickness comparable to cell size has been presented. The observed RBC parachute shapes and velocities are similar to the ones found in glass microcapillaries of similar inner diameter, thus showing that this system is indeed a relevant experimental model to study cell microconfined flow behavior. One of the main results of this work is the development of a novel methodology to estimate cell membrane viscoelastic properties. In particular, in the diverging channel the effect of surface viscosity is dominant with respect to shear elasticity. The main advantages are the small sample volume required, the simultaneous measurement of elastic and viscous parameters, and the continuous flow configuration allowing multiple cells to be examined in the same experiment. Possible applications include the analysis of RBC deformability in pathological situations, for which reliable quantitative methods are still lacking.

## Acknowledgements

Financial support from the Italian Ministry of Research under PRIN 2006 program and from the Regione Campania, L.R. 5 2005 is gratefully acknowledged. Support through the BIO-MICS—Biomimetic and Cellular Systems ESA topical team was also helpful for stimulating discussions and meeting opportunities. The authors thank Prof. F. Salvatore for supporting this work, Prof. G. Marrucci for useful discussions and M. Cirillo for providing the photomask.

## References

- 1 R. Hoffman and E. J. Benz, *Hematology: Basic Principles and Practice*, Philadelphia, 2000.
- 2 S. Guido and G. Tomaiuolo, *C. R. Phys.*, 2009, **10**, 751–763.
- 3 C. Pozrikidis, *Ann. Biomed. Eng.*, 2003, **31**, 1194–1205.
- 4 T. W. Secomb, R. Skalak, N. Özkaya and J. F. Gross, *J. Fluid Mech.*, 1986, **163**, 405–423.

- 5 H. Noguchi and G. Gompper, *Proc. Natl. Acad. Sci. U. S. A.*, 2005, **102**, 14159–14164.
- 6 J. McWhirter, H. Noguchi and G. Gompper, *Proc. Natl. Acad. Sci. U. S. A.*, 2009, **106**, 6039–6043.
- 7 B. Kaoui, G. Birois and C. Misbah, *Phys. Rev. Lett.*, 2009, **103**, 188101.
- 8 G. McHedlishvili and N. Maeda, *Jpn. J. Physiol.*, 2001, **51**, 19–30.
- 9 E. Evans, *Biophys. J.*, 1973, **13**, 941–954.
- 10 E. Evans and P. La Celle, *Blood*, 1975, **45**, 29–43.
- 11 K. G. Engstrom and H. J. Meiselman, *Biorheology*, 1995, **32**, 115–116.
- 12 S. Hénon, G. Lenormand, A. Richert and F. Gallet, *Biophys. J.*, 1999, **76**, 1145–1151.
- 13 J. Mills, L. Qie, M. Dao, C. Lim and S. Suresh, *Mech. Chem. Biosyst.*, 2004, **1**, 169–180.
- 14 A. De Luca, G. Rusciano, R. Ciancia, V. Martinelli, G. Pesce, B. Rotoli, L. Selvaggi and A. Sasso, *Opt. Express*, 2008, **16**, 7943–7957.
- 15 P. Lingard, *Microvasc. Res.*, 1974, **8**, 53–63.
- 16 M. Bessis, N. Mohandas and C. Feo, *Blood Cells*, 1980, **6**, 315–327.
- 17 M. Rosenbluth, W. Lam and D. Fletcher, *Lab Chip*, 2008, **8**, 1062–1070.
- 18 G. Whitesides, *Nature*, 2006, **442**, 368–373.
- 19 W. Lee, H. Bang, H. Yun, J. Lee, J. Park, J. Kim, S. Chung, K. Cho, C. Chung, D. Han and J. Chang, *Lab Chip*, 2007, **7**, 516–519.
- 20 K. Tsukada, E. Sekizuka, C. Oshio and H. Minamitani, *Microvasc. Res.*, 2001, **61**, 231–239.
- 21 J. Shelby, J. White, K. Ganesan, P. Rathod and D. Chiu, *Proc. Natl. Acad. Sci. U. S. A.*, 2003, **100**, 14618–14622.
- 22 S. Shevkoplyas, T. Yoshida, S. Gifford and M. Bitensky, *Lab Chip*, 2006, **6**, 914–920.
- 23 M. Abkarian, M. Faivre and H. Stone, *Proc. Natl. Acad. Sci. U. S. A.*, 2006, **103**, 538–542.
- 24 N. Sutton, M. C. Tracey, I. D. Johnston, R. S. Greenaway and M. W. Rampling, *Microvasc. Res.*, 1997, **53**, 272–281.
- 25 M. Tracey, R. Greenaway, A. Das, P. Kaye and A. Barnes, *IEEE Trans. Biomed. Eng.*, 1995, **42**, 751–761.
- 26 S. C. Gifford, M. G. Frank, J. Derganc, C. Gabel, R. H. Austin, T. Yoshida and M. W. Bitensky, *Biophys. J.*, 2003, **84**, 623–633.
- 27 Z. Tadmor and C. Gogos, *Principles of Polymer Processing*, New York, 1979.
- 28 M. J. Fuerstman, A. Lai, M. E. Thurlow, S. S. Shevkoplyas, H. A. Stone and G. M. Whitesides, *Lab Chip*, 2007, **7**, 1479–1489.
- 29 G. Tomaiuolo, M. Simeone, V. Martinelli, B. Rotoli and S. Guido, *Soft Matter*, 2009, **5**, 3736–3740.
- 30 R. Hochmuth, P. Worthy and E. Evans, *Biophys. J.*, 1979, **26**, 101–114.
- 31 C. W. Macosko, *Rheology*, New York, 1994.
- 32 G. Astarita and G. Marrucci, *Principles of Non-Newtonian Fluid Mechanics*, London, 1974.
- 33 E. Evans, *Biophys. J.*, 1973, **13**, 926–940.
- 34 R. E. Waugh, PhD thesis, Duke University, 1977.
- 35 R. E. Waugh and E. A. Evans, *Biophys. J.*, 1979, **26**, 115–131.
- 36 M. C. Brain, I. Kohn, A. J. McComas, Y. F. Missirlis, M. P. Rathbone and J. Vickers, *N. Engl. J. Med.*, 1978, **298**, 403.
- 37 T. Secomb and R. Hsu, *Biophys. J.*, 1996, **71**, 1095–1101.